

A NUCLEAR FROZEN SPIN TARGET FOR DEUTERON PHOTODISINTEGRATION EXPERIMENTS AT THE HIGH INTENSITY GAMMA SOURCE

Ryan Duve
Charlottesville, VA

Bachelor of Science PHYSICS
University of Connecticut, 2009

A Dissertation presented to the Graduate Faculty of the University of Virginia in Candidacy
for the Degree of Doctor of Philosophy

Department of Physics
University of Virginia
December, 2016

Abstract

The HIGS Frozen Spin Polarized Target, or Hifrost, is a nuclear polarized target apparatus consisting of a dilution refrigerator, internal magnetic coil, microwave guide channel and NMR coils. It is named because it was designed and commissioned to run at HIGS, the High Intensity Gamma Source located on the campus of Duke University. External components of Hifrost include a polarizing magnet, microwave generator, pump and vacuum system to run the dilution refrigerator, and the Q-Meter/Yale Card setup for running the NMR.

Polarized nuclear targets allow measurement of spin observables, the subset of observables from scattering experiments that do not average out the spin component of the scattered and/or scattering particles' wave functions. Polarization of nuclear targets unlock a new degree of freedom to probe and learn about the nuclear system. Experimental data from double polarized spin observables, where both the target and beam probe have some degree of polarization, are rare due to the high technical hurdles of polarizing both target and beam.

To polarize solid targets, chemically doped or irradiated beads are refrigerated to a fraction of a kelvin. The refrigerator is assembled around the beads and swung to align with the HIGS gamma beam. A large external magnet polarizes the target, first to a fraction of percent in thermal equilibrium, then orders of magnitude higher with a technique called dynamic nuclear polarization (DNP).

Frozen spin mode is a configuration where the internal magnet of the apparatus is ramped up as the external magnet is ramped down, so eventually the external magnet can be disconnected and removed from the scattering area while keeping the beads polarized. Frozen spin allows a detector array to be placed around the polarized target without having to consider the effects of the heavy polarizing magnet on the products of the scattering experiment.

Target material in frozen spin mode loses its polarization with time because the DNP process is halted before transitioning between the polarizing and holding magnets. The gamma beam at HIGS does not meaningfully degrade the polarization like ionizing beams used at most other facilities. Therefore, with the holding field held constant, the target temperature is the sole parameter that determines T_1 , the characteristic time describing target polarization loss. In Hifrost, a deuteron target has a characteristic time ranging from hours to days, depending on the run time temperature achieved. Given the beam schedule at HIGS, this is adequate for any polarized target experiment proposed so far.

*This dissertation is dedicated
to the love of my life.*

To Ayla.

Acknowledgements

I could never have contributed so much to this project without the constant help of those around me over the past seven years.

It was only through the teaching style of my advisors, Blaine Norum and Don Crabb, that I gained the confidence in the lab and the management capabilities to take on such a large project. By letting me learn on my own and make mistakes for myself, they have allowed me to take my own path through the doctoral program. I truly owe them for teaching me everything necessary to succeed that isn't written in a textbook.

There are not many polarized target physicists in the world, but those that are active are some of the friendliest, open and helpful people I have ever had the pleasure of working with. I especially owe thanks to Tapio Niinikoski, Chris Keith and Josh Pierce.

David Wimer is technically the "Machine Shop Foreman" at UVa. However, it is no understatement to say he and his machinists are full time "Solvers of Problems." The support provided by them over the years has been unparalleled, and in a very real way this project could not have been successful if they weren't willing to go above and beyond.

The Physics Librarian, Vicky Ingram, is a constant source of help searching for reference material and navigating the ever-changing online library system. Her unwavering positivity and enthusiasm has often been the difference between a good and bad day.

The DFELL and TUNL crew members are too many to name, but their support to this project is the only reason it got off the ground at Duke. Each of them wear many hats and, teaching by example, showed me how to get more done in a day's work than I ever would have thought possible.

Most importantly, I thank my wife Ayla, who supported me by moving down to Virginia my first year at UVa and has been by my side ever since. Thank you for reminding me there is much more to life than physics.

Finally, I thank my son, Moshe. Even though you've only been around a few months, you're the most curious person I have ever met. And curiosity is, after all, the hallmark of science. Thank you for the inspiration.

תושלב"ע

*Charlottesville, Virginia
August 2016*

RYAN DUVE

Contents

1	Theoretical Motivation	1
1.1	Spin in Physics	1
1.1.1	Origin of Spin	2
1.2	History of Polarized Target Physics	5
1.3	Experiments with Hifrost	7
1.3.1	GDH Sum Rule	8
1.3.2	Deuteron Tensor Polarization Measurement	13
1.3.3	Active Proton Target Experiment	16
2	Polarized Target Theory	19
2.1	Spin- $1/2$ Polarization	19
2.1.1	Zeeman Splitting	19
2.1.2	Thermal Polarization Derivation	20
2.1.3	Thermal Polarization Values	22
2.2	Spin-1 Polarization and Alignment	23
2.3	Dynamic Nuclear Polarization (DNP)	29
2.3.1	Optical Pumping	30
2.3.2	Solid State Effect	31
2.3.3	Cross Effect	32
2.4	NMR	32
2.4.1	Liverpool Q-Meter	33
2.4.2	$\lambda/2$ Cable	39
2.5	Frozen Spin	40
2.6	Dilution	41
3	The Hifrost Target	47
3.1	Refrigerator	47
3.2	Holding Coil	51
3.3	NMR	52
3.4	Microwaves	52

4	Equipment Commissioning	53
4.1	Electronics and Instruments	54
4.1.1	^4He Thermometers and Wiring	54
4.1.2	^3He Heaters	59
4.1.3	^3He Thermometers	59
4.1.4	Flow Meter Installation and Calibration	60
4.1.5	Pressure Gauge Installation and Measurements	65
4.2	^4He Cryogenics	67
4.2.1	Outer Vacuum Chamber	68
4.2.2	Heat Leaks	70
4.2.3	Multilayer Insulation (MLI)	74
4.2.4	Bypass Capillary	76
4.3	NMR	78
4.3.1	Yale Card Housing	78
4.3.2	Housing Electronics	81
4.3.3	$\lambda/2$ Cables	84
4.3.4	Finished System Operation	85
4.4	Support Systems	85
4.4.1	LN_2 Traps	85
4.4.2	^3He Recovery System	92
4.4.3	^3He Circulation Loop	95
4.4.4	Mash Cleaning	98
4.4.5	RGA Measurements	100
4.4.6	WKP4000 Roots and ^3He Pump Stack	101
4.4.7	Data Acquisition	104
4.5	Liquid Helium Transfer	122
4.5.1	LHe Transfer Losses	123
4.5.2	LHe Probe	126
4.5.3	Thumper	127
4.6	Indium Extrusion	128
4.6.1	Background	128
4.6.2	Materials	129
4.7	Holding Field	132
4.7.1	Geometric Limitations	132
4.7.2	Inner Vacuum Chamber Can	134
4.7.3	Equipment	136
4.7.4	Coil Winding Procedure	137
4.7.5	Magnetic Field Test	143
4.7.6	Performance	146
4.8	OVC Track	146

5	Geant4 Simulations	149
5.1	Gamma Attenuation	150
6	Cooldown Results	153
6.1	UVa Cooldowns	153
6.1.1	August 2012 - The First Cooling	154
6.1.2	December 2012 - ^3He Circulation Attempt	156
6.1.3	February and April 2013 - Dilution	156
6.2	Duke Cooldowns	157
6.2.1	October 2013 - The First Duke Cooling	157
6.2.2	December 2013 - An Unprepared Cooldown	157
6.2.3	July 2014 - Dilution Cooldown #1	158
6.2.4	October 2014 - Dilution Cooldown #2	161
6.2.5	March 2015 - The Super Cooldown	162
6.3	UVa Cooldowns	167
6.3.1	June 2015 - Low Flow Cooldown	167
6.3.2	July 2015 - Magnet Cooldown #1	168
6.3.3	August 2015 - Magnet Cooldown #2	168
6.3.4	December 2015 - Magnet Cooldown #3	169
7	Conclusions	171
7.1	Conclusion	171
7.1.1	Final Results Review	171
7.1.2	Work To Be Done	174

Acronyms

ADC Analog to Digital Converter

API Application Programming Interface

AWG American Wire Gauge

BRM Balanced Ring Modulator

DAQ Data Acquisition

DFELL Duke Free Electron Laser Laboratory

DNP Dynamic Nuclear Polarization

DVM Digital Volt Meter

EIO Extended Interaction Oscillator

FEP Fluorinated Ethylene Propylene

GDH Gerasimov-Drell-Hearn

HIGS High Intensity Gamma Source

IVC Inner Vacuum Chamber

LMN Lanthanum Magnesium Nitrate

MC Mixing Chamber

MLI Multi-Layer Insulation

NMR Nuclear Magnetic Resonance

OVC Outer Vacuum Chamber

PSI Pounds per Square Inch

PTGroup Polarized Target Group

RGA Residual Gas Analyzer

ROX Ruthenium Oxide

SLPM Standard Liters Per Minute

SQL Structured Query Language

STP Standard Temperature and Pressure

TDR Time Domain Reflectometer

TUNL Tri-University Nuclear Laboratory

UHV Ultra High Vacuum

VDC Volts (DC)

VRT Vacuum Rise Test

Chapter 1

Theoretical Motivation

“ *It is a mysterious beast, and yet its practical effect prevails over the whole of science. The existence of spin, and the statistics associated with it, is the most subtle and ingenious design of Nature — without it the whole universe would collapse.* ”

Sin-itiro Tomonaga, *The Story of Spin*

1.1 Spin in Physics

Before the revolution of quantum mechanics in the early 20th century, the term spin strictly referred to an extended mechanical object with angular momentum. Bohr's early atomic model represented the electrons orbiting the nucleus, similar to the model of the planets of the solar system, with only discrete values of angular momentum $n\hbar$ allowed. The electron was considered to be a point charge particle with no magnetic moment of its own besides this orbital angular momentum term.

1.1.1 Origin of Spin

The Bohr model had been expanded by Sommerfeld and others for ten years before falling out of favor with the scientific community due to an increasing number of discrepancies with the model's predictions. The matter came to a head during the so-called Doublet Riddle of atomic physics during the early 1920s, when the model's success explaining the hydrogen hyperfine structure could not accommodate the observed doublet states of alkali metals[For68]. The German physicist Alfred Landé set out to save the theory in 1924 by showing the two phenomena were mutually caused by magnetic interactions of the outermost electron's orbital angular momentum and the magnetic moment of the rest of the atom. His theory, the last attempt at explaining atomic physics before the introduction of intrinsic spin, "lead completely to disaster at a relativistic interpretation of optical doublets," in Landé's own words[Lan24].

Electron

In late 1924, Austrian physicist Wolfgang Pauli released the results of his failed attempt to find a relativistic correction explaining the differences between the spectra of alkali atoms with different principal quantum numbers. Landé's theory attributed this to the alkalis' "core" electrons (i.e., non-valence electrons) having varying angular momenta for different periods in the periodic table. Pauli's conclusion referred to a "classically non-describable 'twofoldness' of the quantum-theoretical properties of the valence electron," making him the first physicist to abandon the core-model theory in favor of what would become the theory of electron "self-rotation", or spin[Mas05].

Pauli's new paradigm liberated the need to give the non-valence electrons of the atom differing multiplicities depending on the presence of an external magnetic field. The complicated description of atoms was now described by granting the electron $2(2k - 1)$

states, where the leading 2 is Pauli's intrinsic "twofoldness".

Additionally, by introducing a fourth quantum number m associated with the electron's two-state nature, the pattern of how many electrons each atomic shell has can be summarized with a simple rule: any combination of values for the four quantum numbers may not be associated with more than one electron in an atom[Mas05]. This rule, now famously known as Pauli's exclusion principle, directly leads to the result of the first atomic shell holding a maximum of 2 electrons, the second shell holding 8, the third with 18, etc.

Finally, the association of Pauli's new quantum number m and the spin of the electron is attributed to German physicist Ralph Kronig. As a graduate student, Kronig visited Pauli right after publication of the two spin-state electron concept. Kronig interpreted this as a rotation of the electron about its own axis, with an intrinsic angular momentum of $\hbar/2$, allowing it to be oriented in two states relative to the direction of the nucleus angular momentum[MR01]. Kronig then predicted there would be an interaction term between the spin and angular momentum of the electron and calculated the associated energy states, finding they obeyed the Z^4 -law predicted by relativity, the same law Landé's theory could not reproduce. The model of the inner-shell moment was thus discarded for the theory of the electron having an intrinsic spin equal to $\hbar/2$.

Proton

The spin of the proton was found indirectly by spectroscopic studies of the diatomic hydrogen molecule, in its ortho and para configurations, in early 1927. German physicist Friedrich Hund considered the two species of molecular hydrogen in thermal equilibrium and used the available spectroscopic data for angular momentum state transitions to calculate the molecular moment of inertia, I , and the degeneracy ratios of even/odd angular momentum states, β [TN01]. Subsequent spectroscopic measurements made by Takeo Hori, a Japanese physicist working with Bohr in Copenhagen, disagreed with Hund's calculations, showing

I was three times as large as Hund's prediction. Even worse, Hund predicated $\beta \approx 2$, implying the even J states were more highly degenerate than the odds states¹ while Hori found it to be less than 1.

Before Hori's data was even published, fellow visiting physicist David Dennison from the University of Michigan traveled to Copenhagen to learn about the discrepancy. After noticing Hori found no transitions between odd and even J states², it occurred to Dennison the thermodynamic expression Hund used unjustly assumed the two states mixed on a timescale comparable to that of the experiments[Fow36]. With the hindsight of Hori's data, he performed a similar calculation to Hund's except the ortho and para hydrogen species were treated as non-mixing gases, and from this he derived a value of I in agreement with Hori and a ratio of $\beta \approx 1/3$, in line with Hori's findings[Den27]. The 1:3 ratio of symmetric to anti-symmetric hydrogen is exactly what is expected if the proton has the same intrinsic spin as the electron.

From the 1930s to the polarized target

The decades following Dennison's discovery of the proton spin held a flurry of activity for nuclear physics. The 1930s saw James Chadwick's discovery of the neutron, Carl Anderson's discoveries of both the positron and muon, Yukawa's nuclear theory of meson exchange and Heisenberg's trilogy of papers proposing a nucleus made of protons and neutrons. Of course in the first half of the 1940s the physicists working on the Manhattan Project found the path to the atomic bomb and end of World War II, but the late 1940s also saw the discovery of more particles like the pion and kaon, as well as a complete development of Quantum Electrodynamics by Tomonaga, Schwinger and Feynman.

After the arrival of the first particle accelerators in the 1950s, new baryons and mesons

¹This implies the proton behaves like a boson.

²A higher order effect, Hori should have found *some* transition between odd/even states, even if the spectral line showed at very low intensities.

were only being discovered more frequently than ever. At the beginning of his 1955 Nobel Prize speech, Willis Lamb said[Zho13]

When the Nobel Prizes were first awarded in 1901, physicists knew something of just two objects which are now called “elementary particles”: the electron and the proton. A deluge of other elementary particles appeared after 1930; neutron, neutrino, meson, meson, heavier mesons, and various hyperons. I have heard it said that “the finder of a new elementary particle used to be rewarded by a Nobel Prize, but such a discovery now ought to be punished by a \$10,000 fine”.

Lamb’s sentiments reflect the acceleration of new discoveries in the field since the 1920s, among which polarized nuclear targets are just one subfield.

1.2 History of Polarized Target Physics

In his overview of the history of development of the field of polarized targets, Hartmut Dutz begins by saying the “polarized target has been a powerful tool to study spin physics over more than 40 years”[Dut04]. Here we follow his outline of the milestones reached by the polarized target community from the 1960s until today.

Solid polarized targets were first introduced and used in the 1960s by Abragam at Centre d’Etudes Nucléaires de Saclay and Chamberlain et al at Berkeley[CM97]. Around this time, dynamic nuclear polarization (DNP, see Section 2.3) had been found with lanthanum magnesium nitrate (LMN) but was limited to a vertical cryostat with a horizontal magnetic field. Both orientation of the target, which is less convenient than a horizontal arrangement, and the inefficient use of liquid helium by evaporative cooling limited the productivity of these early setups.

The first big experimental improvement came in 1966 in the form of Roubeau's horizontal refrigerator[Rou66], which was so influential it still serves as the basis of the ^4He precooler in Hifrost (see Section 4.2 for details) today. Instead of filling a large vessel with liquid helium before pumping it all away, requiring pauses to refill 2-4 times daily[Dut04], Roubeau implemented a continuous-flow refrigerator that utilizes the cold gas to cool the radiation shielding. This allowed polarized target experiments to run continuously, by virtue of a transfer line that is always delivering liquid helium to the system from an external buffer dewar, and more efficiently since the enthalpy of the cold gas is not going to waste.

LMN was surpassed by organic target compounds such as butanol following the work of Mango, Runolfsson and Borghini in 1969. They found butanol targets, despite only polarizing to 40% instead of the 70% of LMN, has twice the hydrogen density and a dilution factor nearly 5 times greater than LMN[MRB69]. The discovery of organic target materials with paramagnetic centers doped throughout via irradiation reduced run times or increased counting statistics by a factor ten compared to previous methods on top of the factor of two already resulting from Roubeau's continuous refrigerator.

The dramatic effect of temperature on polarization was well known by the 1970s. For example, Mango et al. reported a polarization drop from 44% to 30% when the target temperature increased from 0.98 K to 1.3 K. A series of unpublished experiments showed that the proton polarization could be increased to 80% by decreasing the temperature to 0.5 K, but it wasn't until Roubeau designed a refrigerator that cooled by evaporation of circulated ^3He that these temperatures were taken to polarized target experiments. The ^3He refrigerator utilized Roubeau's older ^4He refrigerator as a precooler with an added ^3He stage, consisting of a target chamber, expansion device and condenser, inserted while already at low temperatures[RV71]. It is in this way polarized proton targets were able to be run continuously at nearly 100% polarization.

The next significant advancement stemmed from the experimental realization of the

dilution refrigerator (DR). Covered in Section 2.6, the inner workings of dilution will not be covered here. It suffices to say the DR's capability to achieve temperatures in the tens of mK with high cooling power directly benefited polarizations of deuterated target materials and allowed for higher beam currents, since the dilution mixture is a more effective coolant than pure ^3He . The practical use of the DR in polarized target experiments would not have been possible without the discovery of the performance of the final DR heat exchanger on the filling factor of the sintered copper powder[Nii71b]. This type of heat exchanger was successfully used in DRs with cooling powers of 0.5 mmol/s and run continuously at 11 mK, and is the same type used in the Hifrost refrigerator.

The high magnetic fields needed to polarize target materials are generated by massive solenoid or Helmholtz coils that necessarily obstruct the ejected particles of interest in a scattering experiment. In 1971, F.M. Russell from Rutherford Lab reported results of a cooldown that used a traditional magnet to polarize a target before being replaced by a weaker magnet, mostly maintaining polarization while opening up spectroscopic access to kinematic particles to nearly 3π steradians[Rus71]. The concept, which Russell called "separated function frozen targets" (now called "frozen spin targets"), is covered in technical detail in Section 2.5. At CERN, Niinikoski was then able to integrate the frozen spin technique into the DR target and, at temperatures significantly lower than the ^3He refrigerator could achieve at Rutherford Lab, he was able to maintain polarization with a holding field an order of magnitude lower[Nii76]. The refrigerator he used to do this is the same design as the refrigerator central to this dissertation.

1.3 Experiments with Hifrost

The Hifrost polarized target system will be used to take measurements of single- and double-polarized observable reactions. This section discusses some experiments on the

horizon.

1.3.1 GDH Sum Rule

The GDH Sum Rule, named after three that discovered it, Gerasimov, Drell and Hearn, is one of a class of relationships derived from dispersion relations that relates polarized observables to the anomalous magnetic moment κ of the target nuclear species. The sum rule for a generalized target of spin S and mass m is

$$\int_{\nu_0}^{\infty} \frac{\sigma_P - \sigma_A}{\nu} d\nu = -4\pi^2 \alpha S \left(\frac{\kappa}{m} \right)^2, \quad (1.1)$$

where σ_P (σ_A) is the cross section between the polarized gamma and target when their spins are aligned parallel (anti-parallel) to one another and α is the fine structure constant.

The GDH Sum Rule is special because it is model independent, that is to say it only relies on the most fundamental physical assumptions. Despite only relying on the fundamentals, it relates directly measured polarized observables (namely, a cross section asymmetry) to the anomalous magnetic moment of a nuclear species. The derivation requires only the following assumptions[A⁺00]:

- Lorentz invariance
- Gauge invariance
- Crossing symmetry
- Rotational invariance
- Causality

- Unitarity

The feasibility of measuring the GDH Sum Rule was deemed by Gerasimov himself to be of academic interest only due to the technical difficulties in making the measurement. Drell and Hearn, on the other hand, determined the experiment would be difficult but possible and called on the community to test it.

Measurements of the high energy (above pion production threshold) contributions to the proton GDH Sum Rule were the result of the formation of the MAMI and ELSA collaboration in the 1990's, which are discussed later in this section. Contributions below pion production are unavailable to the collaboration due to beam limitations, but are available at the Duke Free Electron Laser Laboratory (DFELL) down to 1 MeV. Since the GDH integrand's lower bound is determined by the lowest energy inelastic process, the sum rule integrand for the deuteron must include measurements of these low energies. Furthermore, because the GDH expression is inversely weighed by gamma energy, the low energy components are likely to be a major contribution to the total integrand value.

The derivation of the GDH Sum Rule is covered extensively elsewhere[Hel06], but a schematic overview is as follows. The Compton amplitude for forward scattering between a polarized gamma in the nucleon rest frame can be expanded into five scalar functions

$$\begin{aligned}
 F &= \left\langle \chi_2^\dagger \left| \sum_{i=1}^5 f_i K_i \right| \chi_1 \right\rangle \\
 &= \left\langle \chi_2^\dagger \left| f_1 (\vec{\epsilon}_2^* \cdot \vec{\epsilon}_1) \right. \right. \\
 &\quad \left. + f_2 i \vec{\sigma} (\vec{\epsilon}_2^* \times \vec{\epsilon}_1) \right. \\
 &\quad \left. + f_3 \dots \right. \\
 &\quad \left. + f_4 \dots \right. \\
 &\quad \left. + f_5 \dots \right| \chi_1 \rangle, \tag{1.2}
 \end{aligned}$$

where $\vec{\sigma}$ is the Pauli spin operators, χ_2 (χ_1) is the final (initial) nucleon state, $\vec{\epsilon}$ is the polarization vector of the Compton scattered photon and \dots stand for various terms that vanish with $\vec{\epsilon} \cdot \vec{k}$ for real photons, where \vec{k} is the photon momentum vector.

The only non-vanishing combinations of the functions f_1 and f_2 correspond to the parallel and antiparallel combinations of the nucleon and gamma, namely

$$f_{3/2} \equiv f_1(\nu) - f_2(\nu), \quad (1.3)$$

$$f_{1/2} \equiv f_1(\nu) + f_2(\nu). \quad (1.4)$$

From the modified Dirac equation for the nucleon, the Compton scattering amplitude to first non-vanishing order in the forward direction is

$$f(\nu) = \frac{-\alpha}{m} \vec{\epsilon}_2^* \cdot \vec{\epsilon}_1 - \frac{\alpha}{2m^2} \kappa^2 \nu i \vec{\sigma} \cdot (\vec{\epsilon}_2^* \times \vec{\epsilon}_1), \quad (1.5)$$

where κ is the nucleon anomalous magnetic moment and α is the fine structure constant.

The optical theorem, which depends only on the assumption of unitarity, is applied to the amplitudes in Equations 1.3 and 1.4

$$\text{Im } f_1(\nu) = \frac{\nu}{8\pi} [\sigma_{1/2}(\nu) + \sigma_{3/2}(\nu)] \quad (1.6)$$

$$\text{Im } \frac{f_2(\nu)}{\nu} = \frac{1}{8\pi} [\sigma_{1/2}(\nu) - \sigma_{3/2}(\nu)]. \quad (1.7)$$

Finally, the Kramers-Kronig relation³

³The integral here is actually the principle value \mathcal{P} , defined by $\mathcal{P} \int_{-\infty}^{\infty} \equiv \lim_{\epsilon \rightarrow 0} \int_{-\infty}^{\nu-\epsilon} + \int_{\nu+\epsilon}^{\infty}$.

$$\operatorname{Re} f(\nu) = \frac{2}{\pi} \int_0^\infty d\nu' \nu' \frac{\operatorname{Im} f(\nu')}{\nu'^2 - \nu^2} \quad (1.8)$$

is applied to relate Equations 1.3, 1.4, 1.5 and 1.7 to yield the GDH Sum Rule⁴

$$\frac{\alpha\kappa^2}{2m^2} = \frac{1}{4\pi^2} \int_0^\infty \frac{\sigma_{3/2}(\nu') - \sigma_{1/2}(\nu)}{\nu} d\nu. \quad (1.9)$$

Again, this result is so important because it directly relates a measured lab asymmetry to the purely quantum mechanical anomalous magnetic moment of the target, without relying on any model-specific or phenomenological parameters. It is therefore no overstatement to say a test of the GDH Sum Rule is a test of some of the most foundational pillars of modern physics.

Further order expansions to the gamma energy ν in Equation 1.5 adds the terms $\alpha_E + \beta_M$ and γ_0 to f_1 and f_2/ν , respectively, leading to further dispersive sum rules relating the electric and magnetic polarizabilities

$$\alpha_E + \beta_M = \frac{1}{2\pi^2} \int_0^\infty \frac{\sigma_{1/2}(\nu) + \sigma_{3/2}(\nu)}{2\nu^2} d\nu, \quad (1.10)$$

and the forward spin polarizability, γ_0 , given later in Equation 1.20.

The importance of the GDH Sum Rule is that it is a model-independent result. A laboratory measurement of Equation 1.9 tests the most fundamental assumptions of modern physics.

⁴Values of ν below the inelastic threshold do not contribute to the integral. As such, the lower bound may be written $\nu_\pi \approx 140$ MeV for the pion production threshold on a proton target, and $\nu_0 \approx 2.2$ MeV for the photodisintegration threshold on the deuteron.

Proton Measurements

The GDH Sum Rule for the proton has been measured at energies from 140-800 MeV at MAMI in 2001. The integration corresponds to a result of $-216 \pm 20 \mu\text{b}$ in that range[dV01]. A sister experiment at ELSA was run to continue the integrand measurement from 0.7-3.1 GeV, with the combined value of the integrand found to be $254 \pm 5_{\text{stat}} \pm 12_{\text{sys}} \mu\text{b}$ [DHK⁺04].

Compared to the theoretical prediction for the sum rule of $205 \mu\text{b}$, the MAMI/ELSA collaboration's extrapolation to higher energies yields $215 \mu\text{b}$ for the total value of the proton GDH integrand, within the total experimental uncertainty of 10%[Hel04].

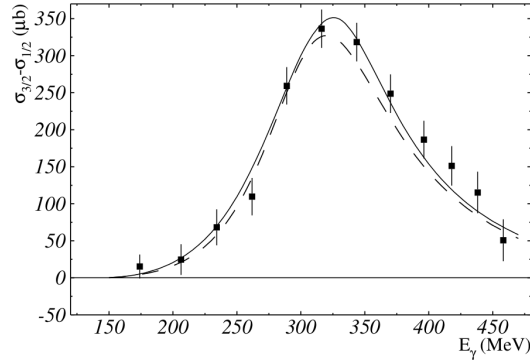


Figure 1.1: The asymmetry measurements taken on the proton at energies above pion production threshold.[A⁺00]

Deuteron GDH

A measurement of the deuteron GDH integrand was made at the Mainz Microtron facility by the A-2 collaboration in 2003 for energies between 0.2-1.9 GeV, with the intention of isolating the first GDH measurement on the neutron⁵.

The results for the data analysis of the proton and neutron contributions to the integrand are approximately $400 \mu\text{b}$ [Bra08]. The large divergence from the theoretical value of $0.65 \mu\text{b}$

⁵This is extracted from deuteron data because $I_{\text{GDH}}^{\text{d}} = I_{\text{GDH}}^{\text{p}} + I_{\text{GDH}}^{\text{n}} + I_{\text{GDH}}^{\text{nuclear effects}}$ [Jah04].

Target	κ	$\int \text{GDH}$
Proton	1.79	$204.0 \mu b$
Neutron	-1.91	$232.0 \mu b$
Deuteron	-0.14	$0.6 \mu b$

Table 1.1: Values for the GDH Sum Rule for different species targets.[Nor09]

is due to the large, low energy contribution to the photodisintegration cross section, which is not accessible at the Mainz facility.

Since the deuteron can be treated as the object of the sum rule, rather than just a necessary target to extract the neutron integrand, measurements on it can be compared to the anomalous magnetic moment just like either nucleon[Nor09]. The sum rule values are given in Table 1.1.

In this way, the HIGS facility and the Hifrost target will provide the missing link, the energy regime from the photodisintegration threshold to $\mathcal{O}(100 \text{ MeV})$, to complete the measurement of the deuteron GDH integrand (see Figure 1.2). As mentioned earlier, the large contribution is due to the inverse gamma energy scaling in the GDH integrand.

1.3.2 Deuteron Tensor Polarization Measurement

As discussed later in Chapter 2, the definition of polarization for a spin-1/2 (two spin state) particle is

$$\mathcal{P} = \frac{N_{\uparrow} - N_{\downarrow}}{N_{\uparrow} + N_{\downarrow}}, \quad (1.11)$$

where N_{\downarrow} (N_{\uparrow}) is the population of spins with m_z equal to $-1/2$ ($+1/2$). The deuteron has spin-1 (three states), so the definition of polarization takes the form

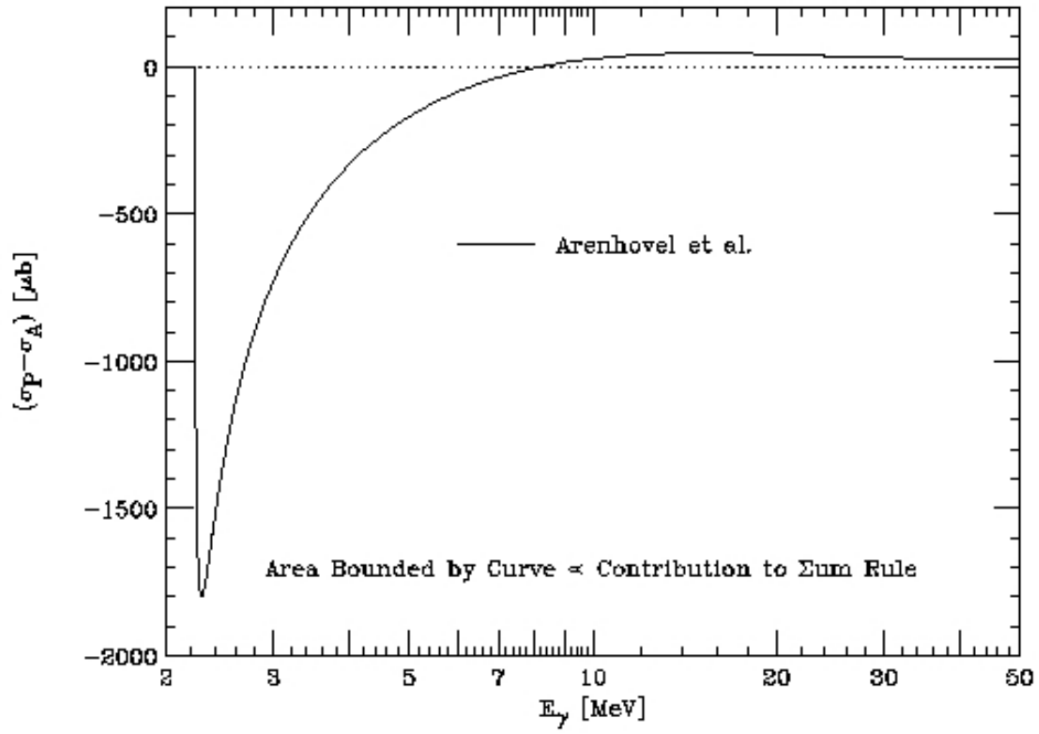


Figure 1.2: A theoretical calculation of the cross section asymmetry for the deuteron at low energies near the photodisintegration threshold[Nor09].

$$\mathcal{P} = \frac{N_{\uparrow} - N_{\downarrow}}{N_{\uparrow} + N_{\downarrow} + N_0}, \quad (1.12)$$

where now N_0 is the population of the $m_z = 0$ state. There is another expression for the relative populations of spin-1 particles, called alignment (or vector polarization), defined by

$$\mathcal{P}_{zz} = \frac{(N_{\uparrow} - N_0) - (N_0 - N_{\downarrow})}{N_{\uparrow} + N_{\downarrow} + N_0} = \frac{N_{\uparrow} - 2N_0 + N_{\downarrow}}{N_{\uparrow} + N_{\downarrow} + N_0}. \quad (1.13)$$

If \mathcal{P} represents the asymmetry between the highest and lowest spin states in a magnetic field, normalized by the total population of all states, then \mathcal{P}_{zz} is the normalized difference between asymmetries of the two upper and two lower states. Note that while polarization has a range from 1 to -1, alignment has a range of 1 to -2, where the latter describes an ensemble entirely in the $m = 0$ state.

If the sum of the state populations is normalized, $N_{\uparrow} + N_{\downarrow} + N_0 = 1$, then the definitions read

$$\mathcal{P} = N_{\uparrow} - N_{\downarrow}, \quad \mathcal{P}_{zz} = 1 - 3N_0.$$

In this way, the polarization \mathcal{P} can be interpreted as a preference in direction for spin, and the alignment \mathcal{P}_{zz} demonstrates a preference in axis[Kei94].

A non-zero alignment affects the differential cross section of the two-body photodisintegration of polarized deuterium[Nor16]

$$\begin{aligned}
\frac{d\sigma}{d\Omega} = \frac{d\sigma_0}{d\Omega} \bigg\{ & 1 - \sqrt{3/4} \mathcal{P}_z \sin \theta \sin \phi T_{11} \\
& + \sqrt{1/2} \mathcal{P}_{zz} \left[\left(3/2 \cos^2 \theta - 1/2 \right) T_{20} \right. \\
& - \sqrt{3/8} \sin 2\theta \cos \phi T_{21} \\
& \left. + \sqrt{3/8} \sin^2 \theta \cos 2\phi T_{22} \right] \bigg\}, \tag{1.14}
\end{aligned}$$

where T_{1m} are the vector analyzing powers and T_{2m} are the tensor analyzing powers[NRS12]. The tensor analyzing power T_{20} in deuteron photodisintegration has never been measured in the 4-20 MeV range, a regime where other discrepancies between theory and world data occur. In practice, the relationship between \mathcal{P} and \mathcal{P}_{zz} is given in thermodynamic equilibrium by[Kie91]

$$\mathcal{P}_{zz} = 2 - \sqrt{4 - 3\mathcal{P}^2}, \tag{1.15}$$

so a 40% polarization implies a 20% alignment.

1.3.3 Active Proton Target Experiment

In Compton scattering experiments on the nucleon, fundamental structure constants called polarizabilities can be probed. Polarizabilities appear when the interaction between the incoming gamma and the electromagnetic field of the nucleon are expanded in higher orders of the energy ω , and can be viewed as the “stretchability” of the nucleon under influence of the external E and B fields[PDV07]. The first and second order terms in the expansion are determined by fundamental constants such as charge, mass and anomalous magnetic moment, and are usually put in terms of the electric (α) and magnet (β) polarizabilities[TSHN98]

$$H_{\text{eff}} = -\frac{1}{2}\alpha_{E1}\vec{E}^2 - \frac{1}{2}\beta_{M1}\vec{H}^2. \quad (1.16)$$

In a naive view of the proton, α represents how the distribution of the pion cloud around a central quark cloud changes under the effect of the external electric field, and β corresponds to the paramagnetic and diamagnetic ordering of the quarks and pions under the external magnetic field[HMP16]. At higher order, the next term in the Hamiltonian H' can be rewritten to include terms that describe how the nucleon's spin is affected by the incoming gamma

$$\begin{aligned} H' = & -\frac{1}{2}\gamma_{E1E1}\vec{\sigma} \cdot (\vec{E} \times \dot{\vec{E}}) - \frac{1}{2}\gamma_{M1M1}\vec{\sigma} \cdot (\vec{B} \times \dot{\vec{B}}) \\ & + \gamma_{M1E2}\sigma_i E_{ij} B_j - \gamma_{E1M2}\sigma_i B_{ij} E_j, \end{aligned} \quad (1.17)$$

where $\vec{\sigma}$ is the nucleon's spin, γ_1 , γ_2 , γ_3 , and γ_4 are the spin polarizabilities, and there is one derivative of the fields with respect to space, $E_{ij} = \frac{1}{2}(\nabla_i E_j + \nabla_j E_i)$, or time, $\dot{\vec{E}} = \partial_t \vec{E}$ [SNP09]. They relate to the terms in the Hamiltonian by

$$\begin{aligned} \gamma_{E1E1} &= -\gamma_1 - \gamma_3, \\ \gamma_{M1M1} &= \gamma_4, \\ \gamma_{M1E2} &= \gamma_1 + \gamma_4, \\ \gamma_{E1M2} &= \gamma_3. \end{aligned} \quad (1.18)$$

The spin polarizabilities can be determined by considering the corresponding energy

shifts of the polarized nucleon in the external field of the gamma, which are proportional to the γ terms. Note that unlike α and β in Equation 1.16, the spin polarizabilities can only be invoked by dynamic fields.

One linear combination of the polarizabilities, the forward spin polarizability γ_0 , is experimentally accessible. It is defined by[HMP16]

$$\gamma_0 = -(\gamma_{E1E1} + \gamma_{E1M2} + \gamma_{M1M1} + \gamma_{M1E2}). \quad (1.19)$$

The well known Gell-Mann-Goldberger-Thirring dispersion relation relates γ_0 to the total photoabsorption cross section with a polarized beam[GMGT54]

$$\gamma_0 = \int_{\nu_0}^{\infty} (\sigma_{1/2} - \sigma_{3/2}) \frac{d\nu}{4\pi^2\nu^3}, \quad (1.20)$$

where $\sigma_{3/2}$ and $\sigma_{1/2}$ are the parallel and antiparallel configurations of the nucleon and photon spin and ν_0 is the threshold for elastic scattering[LN99]. It is this quantity that can be measured with a polarized proton target in the Hifrost system.

Unfortunately, the organic ^{12}C targets used in proton DNP have a coherent Compton scattering cross section 20 times larger than the cross section of interest in Equation 1.20[Mis09]. This background will be eliminated by the presence of a scintillating target, which can discriminate between the proton Compton scattering events and heavy nuclear recoil. Work with different scintillators and target inserts for installation in Hifrost has been done by collaborating group members at the University of Massachusetts, Amherst.

Chapter 2

Polarized Target Theory

2.1 Spin-1/2 Polarization

In the presence of a magnetic field, spin-1/2 nuclei tend to align themselves along the axis of the field. The polarization of the ensemble of particles is defined by

$$\mathcal{P} = \frac{N_{\uparrow} - N_{\downarrow}}{N_{\uparrow} + N_{\downarrow}}, \quad (2.1)$$

where N_{\downarrow} (N_{\uparrow}) is the population of spins with m_z equal to $-1/2$ ($+1/2$). For simplicity, the remainder of this section assumes particles of spin-1/2 unless otherwise stated.

2.1.1 Zeeman Splitting

The effect of a constant magnetic field B in the vicinity of an electron, i.e., a simple spin-1/2 particle, on its Hamiltonian is

$$H = -\vec{\mu} \cdot \vec{B}, \quad (2.2)$$

where μ is the magnetic moment of the electron and the vector multiplication accounts for the direction of the field relative to the axis of the magnetic moment. Taking both to be in the z -direction, we write the energy shift caused by this change in the Hamiltonian in terms of $\vec{\mu} = \mu\sigma_z$ as

$$\langle H \rangle \propto \langle \mu B \sigma_z \rangle \quad (2.3)$$

$$\propto \mu B \langle \sigma_z \rangle \quad (2.4)$$

$$\propto B m_z, \quad (2.5)$$

where m_z is the eigenvalue of the σ_z operator and is positive (negative) when the spin is (anti-)aligned with the field. For the spin- $1/2$ particle, the absolute value of m_z is $1/2$.

2.1.2 Thermal Polarization Derivation

A macroscopically sized target has N particles, where N is very large. While any spin has exactly equal probability of being \uparrow or \downarrow , it is not given that exactly half of N are \uparrow . The relative odds of the system having a particles \uparrow to the system having b particles \uparrow is interesting. To simplify notation, we give the name M_x to number of ways of getting x particles \uparrow and call it the *multiplicity* of getting x . Now it becomes apparent that the probability P_a of the system having a spins \uparrow is related to the probability P_b of having b spins \uparrow is

$$\frac{P_a}{P_b} = \frac{M_a}{M_b}, \quad (2.6)$$

since a higher multiplicity is associated with a higher probability for each state.

Using the fundamental relationship for the system entropy $S = k \ln M$ we arrive at

$$\frac{P_a}{P_b} = \frac{e^{-E_a/kT}}{e^{-E_b/kT}}, \quad (2.7)$$

which is known as the Boltzmann factor that relates P_a to P_b . For the spin- $1/2$ system this gives us the ratio of populations

$$\frac{N_{\downarrow}}{N_{\uparrow}} = \frac{e^{E_{\downarrow}/kT}}{e^{E_{\uparrow}/kT}}. \quad (2.8)$$

We are now in position to rewrite the definition of polarization (Equation 2.1) in terms of thermodynamic variables:

$$\mathcal{P} = \frac{N_{\uparrow}}{N_{\uparrow} + N_{\downarrow}} - \frac{N_{\downarrow}}{N_{\uparrow} + N_{\downarrow}} \quad (2.9)$$

$$= \frac{1}{1 + \frac{N_{\downarrow}}{N_{\uparrow}}} - \frac{1}{\frac{N_{\uparrow}}{N_{\downarrow}} + 1} \quad (2.10)$$

$$= \frac{1}{1 + e^{-\Delta E/kT}} - \frac{1}{1 + e^{\Delta E/kT}} \quad (2.11)$$

$$= \tanh\left(\frac{\mu B}{kT}\right) \quad (2.12)$$

where $\Delta E \equiv E_{\uparrow} - E_{\downarrow} = 2\mu B$, the typical difference in energy levels from a system

undergoing Zeeman splitting.

2.1.3 Thermal Polarization Values

Equation 2.12 gives the degree of polarization for a proton in magnetic field B and temperature T . With modern cryogenic technology, it is relatively straightforward to cool a target sample to 1 K and, using a superconducting solenoid magnet, magnetic fields as high as 7 T.

Plugging these numbers and the magnetic moment of the proton into the thermal polarization equation yields

$$\mathcal{P} = \tanh\left(\frac{\mu B}{kT}\right) \quad (2.13)$$

$$= \tanh\left(\frac{(1.4 \times 10^{-26} \text{ J/T})(7 \text{ T})}{(1.3 \times 10^{-23} \text{ J/K})(1 \text{ K})}\right) \quad (2.14)$$

$$= 0.75\%. \quad (2.15)$$

The deuteron's polarization, which has a different dependence on B and T due to being a spin-1 system (see Section 2.2), can achieve thermal polarizations of

$$\mathcal{P} = \frac{4 \tanh \frac{\mu B}{2kT}}{3 + \tanh^2 \frac{\mu B}{2kT}} \quad (2.16)$$

$$= \frac{4 \tanh \frac{(4.3 \times 10^{-27} \text{ J/T})(7 \text{ T})}{(21.3 \times 10^{-23} \text{ J/K})(1 \text{ K})}}{3 + \tanh^2 \frac{(4.3 \times 10^{-27} \text{ J/T})(7 \text{ T})}{(21.3 \times 10^{-23} \text{ J/K})(1 \text{ K})}} \quad (2.17)$$

$$= 0.02\%. \quad (2.18)$$

While the most modern systems can reach lower temperatures and higher fields, the marginal increase in polarization does not warrant dealing with practical issues of such

systems. For example, lowering T from 1 K to 10 mK, a very difficult task, translates to a deuteron polarization of 1.9%.

It should also be noted that a target with an enhanced polarization, such as those undergoing DNP, will decay towards the thermal equilibrium polarization value once the dynamic orientation processes ceases. The time it takes the polarization to reach a characteristic fraction of its maximum is called the spin-lattice relaxation time, T_1 . Like the thermal polarization expressions above, the time T_1 is a function of μ , B and the temperature T .

2.2 Spin-1 Polarization and Alignment

For the experiments outlined in Chapter 1, the polarized species of interest is the deuteron, a spin-1 particle. While derivation of spin-1 polarization is similar to spin-1/2 polarization, a second description of the ensemble's nuclear spin orientation called the alignment (or tensor polarization) arises. As mentioned in Section 1.3.2, if the polarization describes a preferred direction of the ensemble's spins, the alignment describes a preferred direction.

The derivation of the spin-1 polarization and alignment follows that of the referenced work[Kie91] which was originally done by Goldfarb[Gol58]. We begin by introducing the basis states of the spin-1 spinor

$$\chi_{\uparrow} = \begin{pmatrix} 1 \\ 0 \\ 0 \end{pmatrix}, \chi_0 = \begin{pmatrix} 0 \\ 1 \\ 0 \end{pmatrix}, \chi_{\downarrow} = \begin{pmatrix} 0 \\ 0 \\ 1 \end{pmatrix}, \quad (2.19)$$

and the usual corresponding spin-1 matrix operators

$$S_x = \frac{1}{\sqrt{2}} \begin{pmatrix} 0 & 1 & 0 \\ 1 & 0 & 1 \\ 0 & 1 & 0 \end{pmatrix}, S_y = \frac{i}{\sqrt{2}} \begin{pmatrix} 0 & -1 & 0 \\ 1 & 0 & -1 \\ 0 & 1 & 0 \end{pmatrix}, S_z = \begin{pmatrix} 1 & 0 & 0 \\ 0 & 0 & 0 \\ 0 & 0 & -1 \end{pmatrix}. \quad (2.20)$$

We wish to introduce the density matrix ρ for an ensemble of spin-1 particles¹ such that for any Hermitian operator \mathcal{O} we can find the ensemble average by

$$\langle \mathcal{O} \rangle \equiv \text{Tr } \rho \mathcal{O}. \quad (2.21)$$

In order for ρ to span the entire 3×3 spinor space, it should generally be written in terms of nine linearly independent matrices. While we do not go into origin of the preferred convention, we use the identity matrix $\mathbb{1}$, the basis matrices S_x, S_y, S_z , and six matrices $S_{i,j}$ formed from the basis matrices given by

$$S_{ij} = \frac{3}{2} (S_i S_j + S_j S_i) - 2\delta_{ij}, \quad (2.22)$$

where we use only $S_{xy}, S_{xz}, S_{yz}, S_{xx}, S_{yy}$ and S_{zz} , which are symmetric, traceless and have rotational properties desirable for the density matrix basis[JGO74]. While the ten matrices are now overcomplete, it is still possible to write any general ρ in terms of the basis matrices and coefficients c_i

¹Henceforth, we refer to generalized spin-1 constructs as deuteron constructs, since that is the only spin-1 species of interest in the scope of this dissertation.

$$\begin{aligned}
\rho = & c_1 \mathbb{1} + c_x S_x + c_y S_y + c_z S_z \\
& + c_{xy} S_{xy} + c_{xz} S_{xz} + c_{yz} S_{yz} \\
& + c_{xx} S_{xx} + c_{yy} S_{yy} + c_{zz} S_{zz}.
\end{aligned} \tag{2.23}$$

We now impose the constraint on ρ that it be cylindrically symmetric about the z -axis, which we will take to be the quantization axis of the polarized target. In terms of the generator of rotation, an infinitesimal rotation of ρ by an amount θ is given by

$$\rho \longrightarrow \rho + i\theta [S_z, \rho], \tag{2.24}$$

where the symmetry constraint requires the second term on the right to vanish. Expanding out the commutator using Equation 2.23 gives

$$\begin{aligned}
[S_z, \rho] = & c_{xy} [S_z, S_{xy}] + c_{xz} [S_z, S_{xz}] + c_{yz} [S_z, S_{yz}] \\
& + c_{xx} [S_z, S_{xx}] + c_{yy} [S_z, S_{yy}] \\
& + c_x [S_z, S_x] + c_y [S_z, S_y] \\
& + c_z [S_z, S_z] + c_{zz} [S_z, S_{zz}] + c_1 [S_z, \mathbb{1}],
\end{aligned} \tag{2.25}$$

and the only commutators that vanish are those on the last line of Equation 2.25. Since no S_{ij} terms are linearly dependent, the only way for the transformation 2.24 to hold is for all the coefficients except c_1 , c_z and c_{zz} to vanish. We can now write the density matrix for the deuteron spinor with the constraint of cylindrical symmetry

$$\rho = c_1 \mathbb{1} + c_z S_z + c_{zz} S_{zz}, \quad (2.26)$$

or in matrix form

$$\rho = c_1 \begin{pmatrix} 1 & 0 & 0 \\ 0 & 1 & 0 \\ 0 & 0 & 1 \end{pmatrix} + c_z \begin{pmatrix} 1 & 0 & 0 \\ 0 & 0 & 0 \\ 0 & 0 & -1 \end{pmatrix} + c_{zz} \begin{pmatrix} 1 & 0 & 0 \\ 0 & -2 & 0 \\ 0 & 0 & 1 \end{pmatrix}. \quad (2.27)$$

Since S_z and S_{zz} are traceless, we immediately see that $\text{Tr } \rho = 3c_1$ or $c = 1/3$ from the normalization condition $\text{Tr } \rho = 1$. Since $A_m A_n = 0$ for A in $(\mathbb{1}, S_z, S_{zz})$ and $n \neq m$, we can solve the other coefficients in terms of the ensemble averages defined in Equation 2.21

$$\begin{aligned} \text{Tr } \rho S_z &= c_z \text{Tr } S_z S_z = 2c_z \equiv \langle S_z \rangle, \\ \text{Tr } \rho S_{zz} &= c_{zz} \text{Tr } S_{zz} S_{zz} = 6c_{zz} \equiv \langle S_{zz} \rangle, \end{aligned} \quad (2.28)$$

or $c_z = \langle S_z \rangle / 2$ and $c_{zz} = \langle S_{zz} \rangle / 6$. Renaming the ensemble averages the polarization $P \equiv \langle S_z \rangle$ and alignment $A \equiv \langle S_{zz} \rangle$, we finally write the density matrix in terms of P and A

$$\rho = \frac{1}{6} (2\mathbb{1} + 3PS_z + AS_{zz}), \quad (2.29)$$

or in matrix form

$$\rho = \frac{1}{6} \begin{pmatrix} 2 + 3P + A & 0 & 0 \\ 0 & 2 - 2A & 0 \\ 0 & 0 & 2 - 3P + A \end{pmatrix}. \quad (2.30)$$

Recalling from Equation 2.19 that the components of the state represent the quantum number $m_{\uparrow} = 1, m_0 = 0, m_{\downarrow} = -1$, we now compare the density matrix ρ to that of an ensemble ρ' of $N = N_{\uparrow} + N_0 + N_{\downarrow}$ deuterons each in one m state

$$\rho' = \frac{1}{N} \begin{pmatrix} N_{\uparrow} & 0 & 0 \\ 0 & N_0 & 0 \\ 0 & 0 & N_{\downarrow} \end{pmatrix}. \quad (2.31)$$

Comparing ρ and ρ' yields expressions for the polarization P and alignment A in terms of the populations $N_{\uparrow}, N_0, N_{\downarrow}$,

$$A = \frac{N_{\uparrow} + N_{\downarrow} - 2N_0}{N}, \quad P = \frac{N_{\uparrow} - N_{\downarrow}}{N}, \quad (2.32)$$

which are the deuteron versions of the proton's Equation 2.1. Note that the limits on A and P are

$$-1 \leq P \leq 1, \quad -2 \leq A \leq 1, \quad (2.33)$$

each corresponding to the entire ensemble in one m sub-level. In particular, $A = -2$

signifies all deuterons are in the N_0 state.

Finally, consider the energy level splitting from the Zeeman interaction of a deuteron in a magnetic field, Equation 2.2. If the energy zero is taken so the partition function can be written $\mathcal{Z} = e^{-\beta} + 1 + e^{\beta}$, then the corresponding density matrix is

$$\rho^{\text{MB}} = c_{\text{MB}} \begin{pmatrix} \beta & 0 & 0 \\ 0 & 1 & 0 \\ 0 & 0 & \frac{1}{\beta} \end{pmatrix}, \quad (2.34)$$

where c_{MB} is the normalization constant for the density matrix obeying Maxwell Boltzmann statistics. Such an ensemble arises when a system of spins is in thermal equilibrium with a reservoir, as described in Section 2.1.2. Again, from the normalization condition $\text{Tr } \rho^{\text{MB}} = 1$ we find $c_{\text{MB}} = \beta (\beta^2 + \beta + 1)^{-1}$. Comparing the terms in the matrices 2.30 and 2.34 produces the equations

$$\frac{2 + 3P + A}{2 - 2A} = \frac{\beta}{1}, \quad \frac{2 - 3P + A}{2 - 2A} = \frac{1}{\beta}, \quad (2.35)$$

which can be solved to put A in terms of P

$$A = 2 + \sqrt{4 - 3P^2} \quad (2.36)$$

$$A = 2 - \sqrt{4 - 3P^2}, \quad (2.37)$$

of which only the solution Equation 2.37 is physical from the inequalities in Equation 2.33. This shows that, in thermal equilibrium, a vector polarization necessarily implies a non-zero

alignment. Comparing the matrix forms of ρ^{MB} and ρ' , the definitions of A and P from Equation 2.32 are written

$$\begin{aligned} P &= \frac{\beta}{\beta^2 + \beta + 1} \left(\beta - \frac{1}{\beta} \right) = \frac{\beta^2 - 1}{\beta^2 + \beta + 1} \\ &= \frac{e^{2x} - 1}{e^{2x} + e^x + 1} \end{aligned} \quad (2.38)$$

$$\begin{aligned} &= \frac{2 \sinh x}{2 \cosh x + 1} = \frac{2 \sinh \frac{x}{2} \cosh \frac{x}{2}}{4 \sinh^2 \frac{x}{2} + 3} \\ &= \frac{4 \tanh \frac{x}{2}}{3 + \tanh^2 \frac{x}{2}}, \end{aligned} \quad (2.39)$$

$$\begin{aligned} A &= \frac{\beta}{\beta^2 + \beta + 1} \left(\beta + \frac{1}{\beta} - 2 \right) = \frac{(\beta - 1)^2}{\beta^2 + \beta + 1} \\ &= \frac{(e^x - 1)^2}{e^{2x} + e^x + 1} \end{aligned} \quad (2.40)$$

$$\begin{aligned} &= \frac{4 \sinh^2 \frac{x}{2}}{2 \cosh x + 1} = \frac{4 \sinh^2 \frac{x}{2}}{4 \sinh^2 \frac{x}{2} + 3} \\ &= \frac{4 \tanh^2 \frac{x}{2}}{3 + \tanh^2 \frac{x}{2}}. \end{aligned} \quad (2.41)$$

In lines 2.38 and 2.40, the substitution $\beta = e^x$ was made since in thermal equilibrium the ratio of the populations between two states is a ratio of exponentials of the form $e^{-E/kT}$ (see Section 2.1.2). Equation 2.39 is the deuteron form of the proton's polarization (see Equation 2.12), and Equation 2.41 shows the dependence of the magnetic field B and the temperature T on the alignment.

2.3 Dynamic Nuclear Polarization (DNP)

If allowing the spin system to take on its thermal polarization distribution according to Maxwell-Boltzmann statistics is called *static nuclear polarization*, then disturbing the

equilibrium configuration to preferentially flip nuclear spins is called *dynamic nuclear polarization*, or DNP. There are several different processes that end up achieving net nuclear orientation, but all of them involve optically pumping a spin species in a magnetic field to a different Zeeman state. Only two mechanisms, the solid effect and the cross effect, are discussed here.

We follow the descriptions of DNP laid out for us by Borghini in his *Mechanisms of Nuclear Dynamic Polarization by Electron-Nucleus Dipolar Coupling in Solids* [Bor71], which is strongly recommended for further reading on DNP, augmented with up to date information found in the *Polarization Mechanisms* chapter of Crabb and Meyer[CM97].

2.3.1 Optical Pumping

In any system with discrete energy levels E_1 and E_2 , the separation can be described with a frequency ω defined by $E = \hbar\omega$, where E is the energy difference $E_1 - E_2$. If the system consists of a single particle in the lower state, an incoming photon of frequency ω can stimulate the particle to transition to the higher energy state². Likewise, if the particle is already excited, the photon can stimulate a transition to the lower energy state.

If the system now has many particles which may occupy either state, an incoming photon has an equal chance to interact with any of them, stimulating a transition up or down. Therefore, the odds of the photon exciting a particle to energy E_2 is proportional to the number of particles already in the state with energy E_1 . After bombarding the system with many photons, and barring any other path through which the particles may change states, we then expect the equilibrium state of the entire system to have half of its particles with energy E_1 and the other half with E_2 .

If the particles are spin- $1/2$ nuclei and the E_1 and E_2 are the particles' corresponding

²For this to be true, other constraints like angular momentum conservation must be obeyed; further mention of this and similar caveats are omitted for the rest of this section.

Zeeman energies in a magnetic field, it is clear from Equation 2.1 that there will be no net polarization. Therefore, optically pumping a two state system is not a solution to polarizing a target.

Now consider a third state with energy $E_{1.5}$ such that $E_1 < E_{1.5} < E_2$, and two additional spontaneous decay paths particles can take from energies $E_2 \rightarrow E_{1.5}$ and $E_{1.5} \rightarrow E_1$. If the latter process is much slower than the former, then particles with energy $E_{1.5}$ will begin to accumulate! If the transition $E_{1.5} \rightarrow E_1$ is negligibly slow, then almost all the particles will end up with energy $E_{1.5}$ and the ensemble will have a preferred state, as desired.

Of course, there is no such thing as a spin- $1/2$ particle with three Zeeman states, so the above discussion regarding $E_{1.5}$ is strictly hypothetical. However, more complicated systems can use several particles (and/or several particle species) to achieve the same desired result. The additional particles are usually either electron dopants, added to the target material via irradiation, or chemical dopants mixed into the material before target solidification.

2.3.2 Solid State Effect

In a system of unpaired electrons and spin- $1/2$ nuclei, an applied magnetic field will polarize the electrons almost entirely, as their magnetic moment μ is nearly three orders of magnitude greater (recall $P = \tanh \mu B / kT$ from Equation 2.12). In a nutshell, the mechanism of the solid state effect is to excite a pair of spin- $1/2$ particles (an electron and a proton) simultaneously, and allow the the electron to spontaneously decay back to its ground state at a much faster rate (see Figure 2.1). In this way, a single electron is capable of polarizing many nuclei.

2.3.3 Cross Effect

Another DNP process, called the Cross Effect, takes place when free-electron dopants are densely scattered throughout the nuclear sample. When electron spin-spin interactions are no longer negligible, there exist distinct thermal reservoirs for the Zeeman and spin-spin interactions simultaneously. The spin reservoir can be independently cooled by optically pumping electrons of two breeds (that is, two different Zeeman energy splittings) at a frequency near their separation energy. This exchange between the two types of electrons is the “cross” in the Cross Effect. Since the energy of the spatially dense spin ensemble varies slightly with the magnetic ordering, a narrow continuum band of energies for each type of electron exists and may be cooled by selecting pumping into different energy substates.

Once the spin reservoir is cooled in this way, sufficient thermal contact to the nucleon reservoir is achieved and the result is a net enhanced polarization. This concept is called Equal Spin Temperature theory and, for the purposes of this description of DNP, is tightly related to the Cross Effect.

2.4 NMR

Nuclear Magnetic Resonance (NMR) is the method we use to measure the polarization of the target material. Essentially, a coil in the immediate vicinity of the target acts as the inductor in a series LCR circuit, the inductance of which changes as a function of the magnetic susceptibility of the nuclei in the coil. Since the magnetic susceptibility and polarization are related, the resonance frequency of the LCR circuit tell us information about the polarization of the target material[CG80].

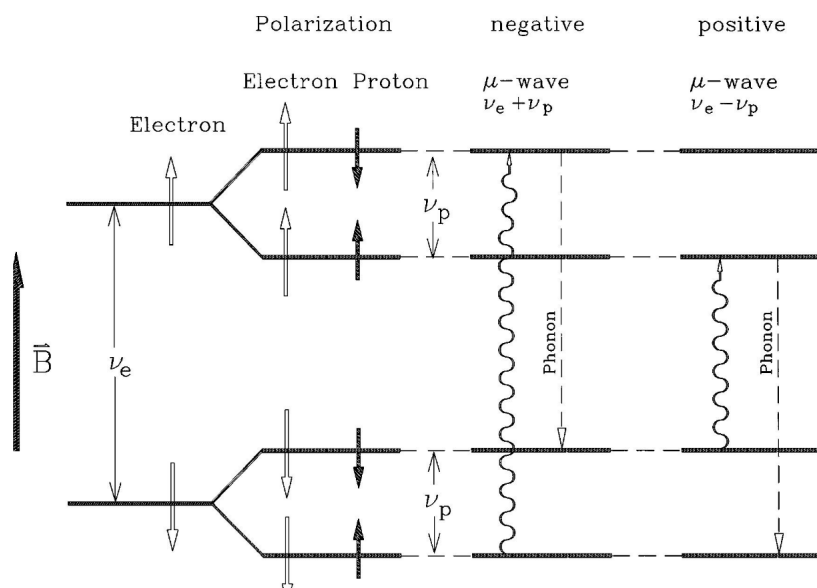


Figure 2.1: DNP diagram [CM97]. The white arrows are electron polarization and the black arrows are proton polarization. Microwaves at a frequency difference $\nu_e \pm \nu_p$ flip the spins of both particles, and the electron's superior lattice coupling ensures it will flip back before the proton.

2.4.1 Liverpool Q-Meter

The Q-Meter houses the capacitor and resistor for the LCR circuit, as well as detectors that transform the signal into usable data representing polarization³. The Q-Meter is entirely encased in gold-plated copper case to keep out RF noise from the lab, and all connectors and cables carrying RF signals that connect to the Q-Meter must also be similarly shielded.

LCR Circuit

The *Liverpool NMR Module* is a system for measuring the polarization of polarized nuclei using Q-Meter measurements of their resonant frequency. It uses an LCR circuit with the polarized material contained in the inductor. The resonant frequency of the circuit is calibrated to be the same as the magnetic resonant frequency of the material, given the value of the base magnetic field. The polarized material affects the inductance of the circuit

³Much of this section is from PTGroup's Lab Overview[DS15]

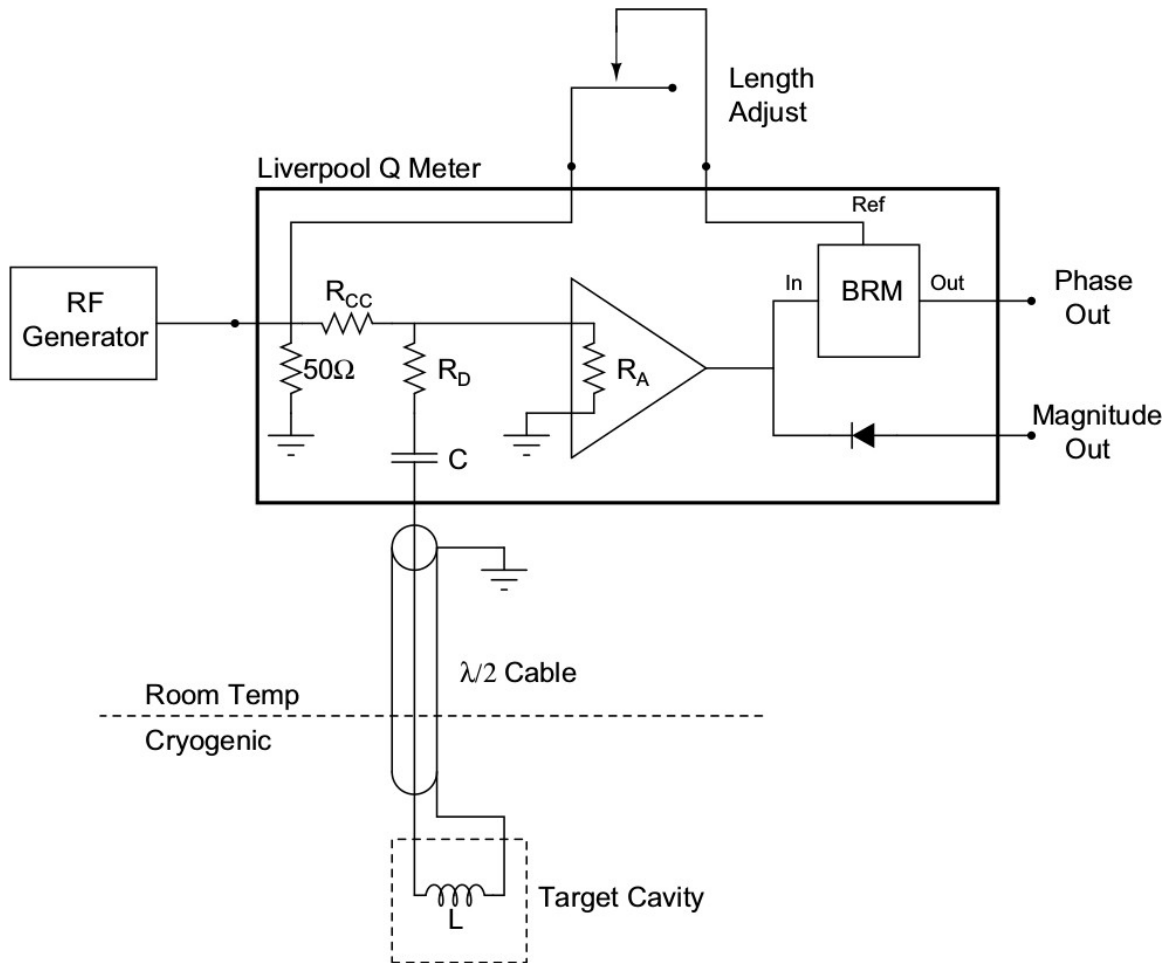


Figure 2.2: Schematic of the Q-Meter circuit. As mentioned in the text, the LCR circuit makes a resonance pass filter that is tuned to the nuclear Larmor frequency of interest. More details are found the referenced dissertation [McK00].

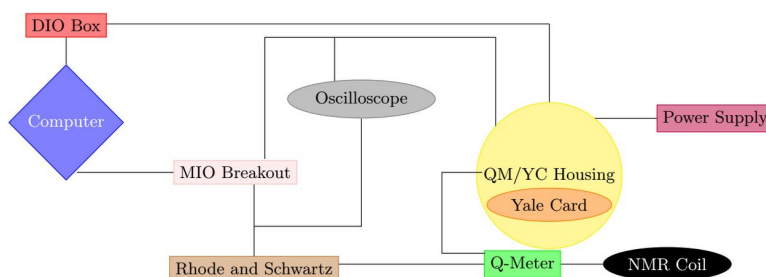


Figure 2.3: Q-circuit schematic

and therefore produces a change in the quality factor, Q , as measured by a device called a Q-Meter, as well as impedance. This change is measured by applying a frequency swept RF voltage to the tuned circuit and detecting the change in impedance as a change in current or voltage. The different elements of the Liverpool Module are arranged in the *Q-Circuit* (Figure 2.3).

Q-Curve

A plot of the RF frequency on the x-axis and the max signal (in volts) seen by the scope is called a *Q-Curve* (Figure 2.4).

This curve can be shown on the scope's XY mode by plugging the RF input to channel 1 and the diode detector on channel 2. A Q-Curve is referred to as *tuned* when the central frequency of the RF sweep is at the center of the Q-Curve. Since the central frequency is fixed, this is achieved by adjusting L and C of the circuit so the LCR resonance equals the desired frequency.

A Q-Curve tuned to the resonance frequency of a polarized target has a very special quality. When something is placed inside the inductor of the circuit, like an actual polarized target or a “dummy” oscillator chip that absorbs EM radiation at the resonance frequency, we see a signal on the scope where the x-axis marks resonance (Figure 2.5b). The more

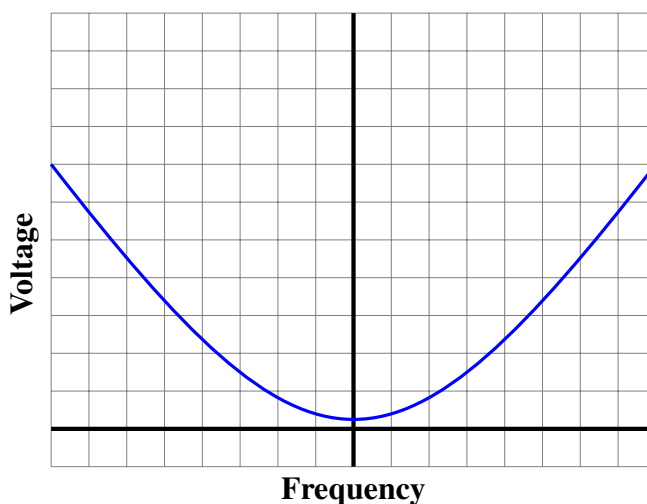


Figure 2.4: A Q-Curve plot with RF frequency on the X-axis and scope (detector) signal on the Y-axis.

polarized a target is, the larger the signal will be.

The nature of the signal is dependent on the nuclear species, the molecular structure the nucleus is in (usually an ammonia or alcohol) and some other factors. In all cases, the signal arises because the resonance frequency corresponds to a photon of energy equal to the nuclear Zeeman splitting that stimulates emission/absorption from the target material (see Section 2.1.1).

The Q-Curve without the signal is subtracted from the Q-Curve with the signal (called a *background subtraction*) and what remains is a bump with an area proportional to the polarization of the target material. In this way, an LCR circuit is used in the NMR setup to measure nuclear polarization.

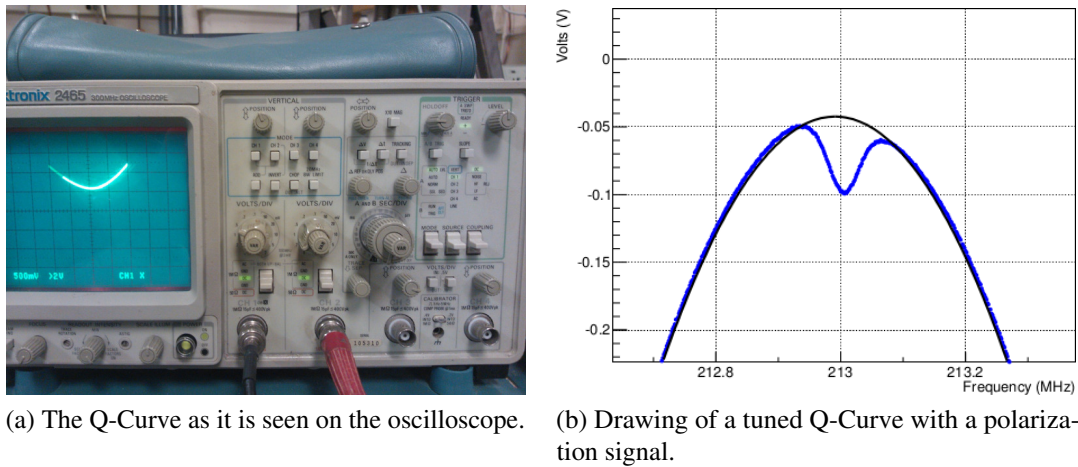


Figure 2.5: The Q-Curve shown on the scope and on a computer program[Kel13].

Diode Detector

The output of the LCR circuit is a sine wave of the same frequency as the RF output. A diode detector is basically a full wave rectifier that smooths out the magnitude of the resulting waveform (Figure 2.6).

The output can be thought of as a DC voltage comparable to the peak signal from the LCR circuit. Tuning always begins by looking at the diode because it makes finding the correct $\lambda/2$ cable length and Q-Meter capacitance simpler.

Phase Detector and Phase Cable

Once a signal is seen with the diode detector, we switch to a more sensitive detector built into the Q-Meter. The phase detector has a core component called a balanced ring modulator (BRM) that takes two inputs, the LCR signal and the RF signal, and provides one output, an phase-dependent signal that indicates target polarization.

Generally, a BRM multiplies the two input signals and outputs a signal proportional to the phase difference between them. When no polarized target is present, the relative phase

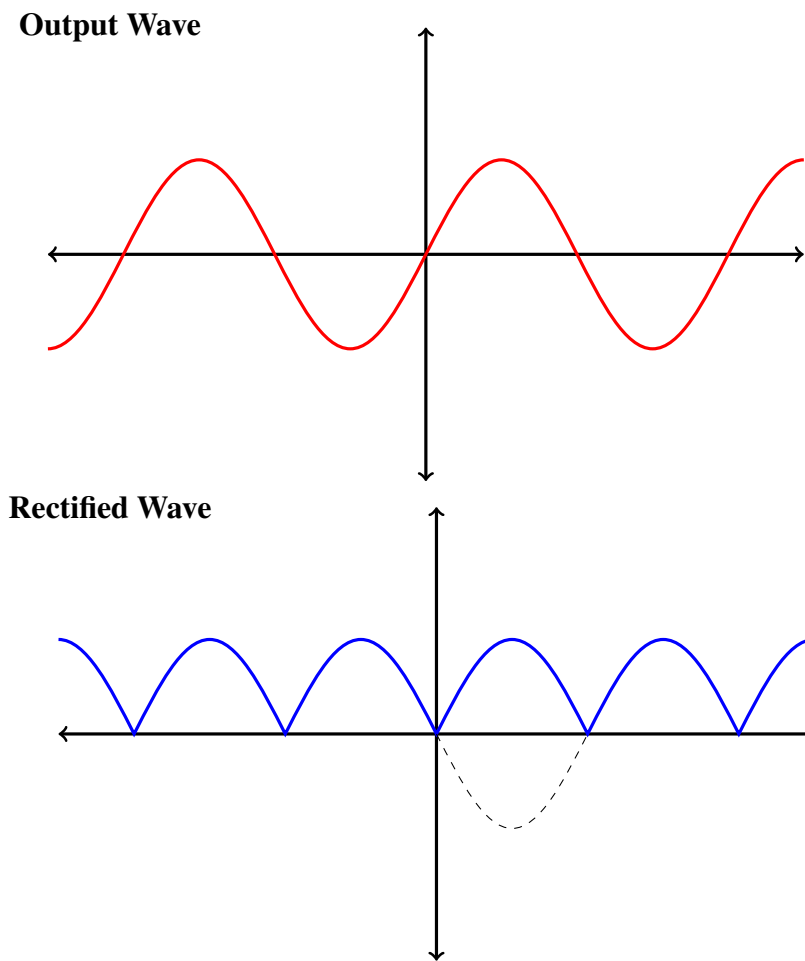


Figure 2.6: The output of the LCR circuit (top) and that same output rectified by a diode detector (bottom)

between inputs is adjusted to zero by adding electrical path length with a so-called phase cable. When the phase difference is set to zero, the BRM output is proportional to the real part of the LCR signal. For this reason, the phase detector is also sometimes called a “real part” detector. The phase cable is adjusted just like the $\lambda/2$ cable, except it is shorter and both ends are connected to the Q-Meter (see PTGroup’s “Q-Meter Tune” document for tuning details).

2.4.2 $\lambda/2$ Cable

Because polarization requires that the target material be kept at a very low temperature and the lab’s electronics are difficult to operate at such temperatures, the inductor coil must be coupled to the circuit by use of cables of length comparable to the wavelength of the RF (that is, λ). In this way, the impedance due to the inductor is the same as it would be if there was no cable attachment.

If the electrical path between the Q-Meter and coil had a length different than $n\lambda/2$, the Q-Meter would see an (input-) impedance larger than the coil’s actual (load-) impedance. For our purposes, the load impedance is the actual resistance of the NMR coil, and the input impedance is the resistance the coil appears to be from the Q-Meter. If the Q-Meter is some length l from the coil, then the input impedance it sees is given by

$$Z_{\text{input}} = K \frac{Z_L + K \tanh(i2\pi l/\lambda)}{K + Z_L \tanh(i2\pi l/\lambda)}$$

where K is a constant characteristic of the cable, called its *characteristic impedance*. Clearly, this is at a minimum when the Q-Meter is a multiple of half a wavelength, which is when the input impedance equals the load impedance.

The above is a simplification: the cables are actually lossy so the given equation has an attenuation component, the velocity of light in the cable needs to be taken into account when determining l , refrigerator temperature and phase-transition temperatures of materials within the cables can play a role, etc. However, these effects are easily corrected for or otherwise tend to be negligible.

In the lab, the length l is already at some minimum value because of the finite electrical path inside the Q-Meter and inside the refrigerator. In addition to that unchangeable length, the Q-Meter is connected to the refrigerator with a $\lambda/2$ cable. l is adjusted by adding or removing length to this cable, which can be tedious since there is no continuous variable adjustment. Suboptimal connections between the constituent $\lambda/2$ cable components leads to unpredictable and often irreproducible signals on the scope. Additionally, all cables are “semi-rigid” meaning they have copper shields which make them resistant to bending. The biggest difficulty trying to get the right $\lambda/2$ -cable length tends to be finding the right combination of cables that sum to the desired length.

2.5 Frozen Spin

A typical nuclear polarized target is continuously polarized with a large external magnet⁴. The material that comprises and surrounds the magnet is thick and contains heavy elements which affect the trajectories of the observed particles.

One way to avoid positioning the polarizing magnet between the target and detectors during an experiment is the “frozen spin” mechanism. A weak magnet internal to the target cryostat maintains a field in the same direction as the polarizing magnet. Once the

⁴See, for example, the G2P experiment at JLab[JLA12]

target material is polarized, the holding field is ramped up while the polarizing field is ramped down and physically removed from around the target. The holding field provides a quantization axis to prevent the target nuclei from immediately becoming disoriented. Without the polarizing magnet in the way, the particles of interest are free to exit the dilution refrigerator and head unobstructed to the detectors.

2.6 Dilution

At the heart of the refrigerator is the mixing chamber, a vessel that cools a mixture of $^3\text{He}/^4\text{He}$ isotopes below liquid evaporative temperatures. The process of cooling the mixing chamber below 1 K is called dilution, which exploits an endothermic reaction involving two phases of helium mixtures, absorbing heat from the system in the process.

Before dilution can be explored, the separation of a $^3\text{He}/^4\text{He}$ mixture needs to be understood. Above about 0.87 K, a mixture of ^3He and ^4He liquid does not exhibit special characteristics not manifest in pure ^3He or ^4He liquid. Figure 2.7 shows the phase separation temperature as a function of ^3He concentration, which is a consequence of the ideal free energy of mixing vanishing as $T \rightarrow 0$ while the excess free energy of mixing is positive at $T = 0$ [Che55]. This phase separation is just like any other, and can be viewed as the ^3He atoms being more strongly bound to one another than to ^4He atoms. They then float upwards due to the higher density of ^4He liquid, spatially separating the phases. The area below the curve is inaccessible to a helium mixture. For example, if a mixture of equal parts $^3\text{He}/^4\text{He}$ were cooled from 1 K to 0.85 K it would not qualitatively change since the coordinate (50%, 0.85 K) on Figure 2.7 is not in the forbidden region. After continuing to cool to 0.5 K, it would separate into two mixtures of differing ^3He fractions, one 20% and the other 80% ^3He .

The helium does not separate in purely ^3He and ^4He phases as might be expected. To see

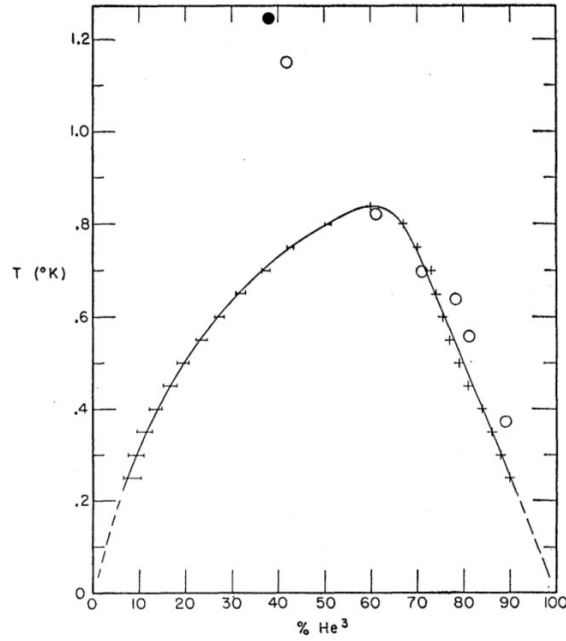
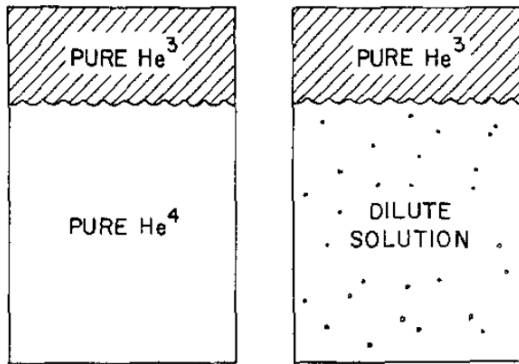
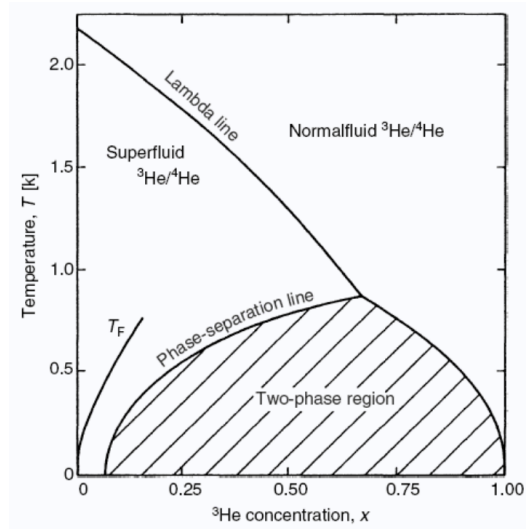


Figure 2.7: Walters and Fairbank's measurements of the phase separation of ^3He and ^4He mixtures at different ^3He concentrations[WF56]. The white circles are measurements by a previous group. The dotted line at low temperatures is was a common extrapolation at the time, since no one thought the curve should intercept the x-axis anywhere except $T = 0$.



(a) Two candidates for the result of a cooled mixture of pure liquid helium isotopes[Whe68].



(b) Dilution diagram[Pob07].

Figure 2.8: The candidates for a cooled mixture of ^3He and ^4He isotopes and their accompanying phase diagram.

why, consider what happens when a volume of pure ^3He liquid is in contact with a volume of pure ^4He liquid beneath it and subsequently cooled⁵. The equilibrium condition between ^3He particles in the two phases is given by

$$\mu_U = \mu_L, \quad (2.42)$$

where μ_U (μ_L) is the chemical potential for ^3He in the upper (lower) phase. Near $T = 0$, the fermi particles are simply “stacked” by energy as they are added to the system, with each new particle taking up the lowest accessible energy state, as shown on the left hand side of Figure 2.9. Here, the positive quantity L_{03} is the latent heat of vaporization, the energy required to remove from the system entirely one atom of ^3He from the liquid state, and E_{03} is the positive energy of one ^3He atom in a reservoir of liquid ^4He .

If $E_{03} > L_{03}$, as shown on the diagram and is consistent with experiments referenced in the literature[Whe68], then the ^3He atom will be more strongly bound to the ^4He reservoir than a neighboring liquid ^3He reservoir at low temperatures. Thus, there is some ^3He solubility in ^4He at low temperatures, as illustrated in Figure 2.8. However, the solubility is limited. The cartoon on the left side of Figure 2.9 shows the helium atoms “filling up” the available phase space between energies $-E_{03}$ and $-L_{03}$ (two per state to account for the spin- $1/2$ property), with the energy coming from the translational degree of freedom equivalent to a fermi momentum⁶. Taking the lower phase as the diluted ^4He in Equation 2.42, we can take $\mu_L = -E_{03} + kT_F$ and rewrite the equation as

⁵This thought experiment, as well as the remainder of this chapter, closely follows the discussion of Wheatley[Whe68], which is strongly recommended for an introductory overview of dilution.

⁶The mass in $kT_F = p_F^2/2m^*$ is an effective mass since the ^3He atom is not in a true vacuum, but an inert ^4He background. It is this background that serves to modify the mass into an “effective mass” $m^* \approx 2.4m$ in the energy equation.

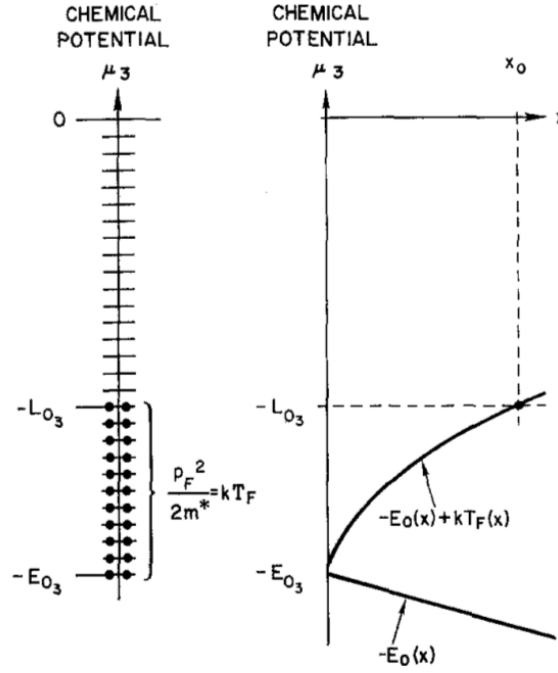


Figure 2.9: On the left, the chemical potential of a new ^3He atom being added to a system[Whe68]. On the right, the energies of a ^3He atom in a ^3He (^4He) reservoir is shown on the top (bottom).

$$-L_{03} = -E_{03} + kT_F. \quad (2.43)$$

The plots for these expressions for the ^3He chemical potential are shown on the right side of Figure 2.9, and their intersection marks where the maximum solubility x_0 of ^3He in liquid ^4He . A derivation of the linear relationship of E_0 on the ^3He solubility x is beyond the scope of this chapter, but Wheatley derives it by considering all combinations of ^3He atoms, ^4He atoms, and holes in the ^4He background. The curve of μ_U , on the other hand, can be derived from elementary statistical mechanics. The density of states for a phase-sphere of three positive momentum coordinates \vec{p} and a volume Ω requires all states n with kinetic energy less the fermi energy to be populated,

$$x = \frac{n}{\Omega} \propto p_F^3. \quad (2.44)$$

Plugging this into the fermi energy we have

$$kT_F = \frac{p_F^2}{2m^*} \quad (2.45)$$

$$\propto a(x) \left(\frac{x}{\Omega} \right)^{2/3}, \quad (2.46)$$

where the “constant” a contains the effective mass m^* and varies weakly enough with x to consider it static[Whe68]. Putting this dependence in Equation 2.43 yields the curve on the right side of Figure 2.43 and completes the (extremely simplified) discussion of the finite solubility of ^3He in ^4He at low temperatures.

Given there are dilute and concentrated phases in the mixing chamber, we follow Pobell’s derivation of the cooling power of dilution unit by performing an enthalpy balance involving the liquids entering and leaving the final heat exchanger[Pob07]. In equilibrium, the molar flow of ^3He circulated \dot{n} will determine the cooling power of the refrigerator \dot{Q} . Energy in the form of heat in the mixing is absorbed for each ^3He atom circulated through the refrigerator, or more specifically across the dilute/concentrated helium mixture phase boundary, because the enthalpy of ^3He is greater in the dilute phase than in the concentrated phase.

Taking H_d as the enthalpy of saturated, i.e., $\approx 6\%$ ^3He , dilute mixture and H_3 as the enthalpy of pure incoming ^3He , the enthalpy balance gives us

$$\dot{Q} = \dot{n} \{ \Delta H_{\text{cooling}} - \Delta H_{\text{incoming}} \} \quad (2.47)$$

$$= \dot{n} \{ [H_d(T_{\text{MC}}) - H_3(T_{\text{MC}})] - [H_3(T_{\text{HX}}) - H_3(T_{\text{MC}})] \}, \quad (2.48)$$

where T_{MC} and T_{HX} are the temperatures of the mixing chamber and final heat exchanger, respectively. Numeric values for the specific heats⁷ taken from different measurements[Pob07] allow the enthalpies to be written in terms of the temperatures

$$\dot{Q} = \dot{n} (95T_{\text{MC}}^2 - 11T_{\text{HX}}^2) \quad (2.49)$$

where \dot{n} is in moles of ^3He per second and the constants contain units so \dot{Q} has units of watts. The Hifrost refrigerator, which was designed to run at a circulation rate of 20 mmol/s, can therefore theoretically reach a minimum of 24 mK while providing 1 mW cooling power.

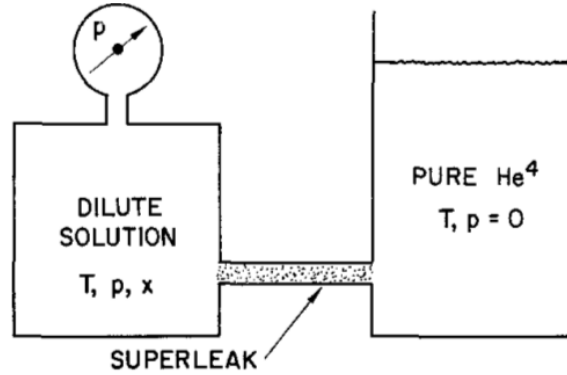


Figure 2.10: Wheatley's illustration of pure superfluid helium separated from a dilution solution by a "superleak".

⁷Recall the equilibrium condition Equation 2.42 and the definitions $\mu = H - TS$ and $S = \int C_P/T dT$.

Chapter 3

The Hifrost Target

The principle components of the Hifrost target, such as the refrigerator, NMR and magnets, are addressed theoretically in Chapter 2 and in technical detail in Chapter 4. This chapter serves to bridge the two, providing an overview of how the target operates and the interdependence of the constituent subsystems during practical operation.

3.1 Refrigerator

The cryogenic components of Hifrost may be considered the foundation of the target¹, with the other system built and operated within the constraints imposed by them. Therefore, we will explain how the refrigerator works first, and delay mention of the other subsystems for later.

Figure 3.1 shows the principle components of the refrigerator with the upstream end² on the left. Liquid helium, driven by a pressure differential between the separator and external dewar, enters the refrigerator through a transfer line inserted in the upstream end of the

¹Hifrost is often referred to as a “refrigerator” instead of a polarized target.

²The upstream end is where the beam enters the target during an experiment. Closer to the target material, the downstream end (right hand side on Figure 3.1) is where the beam exits.)

refrigerator. The delivery end of the transfer line coincides with an opening in the top of the separator, which itself is pumped on by two separator pump lines, called the shield and counter-current lines. The helical shield line is cooled by the evaporated gas and forms a heat sink for the radiation shields anchored to it from the outside. Eventually, the orifice will cool allowing liquid helium to fall through the porous, sintered copper separator, while the gas is continuously rejected and pumped away.

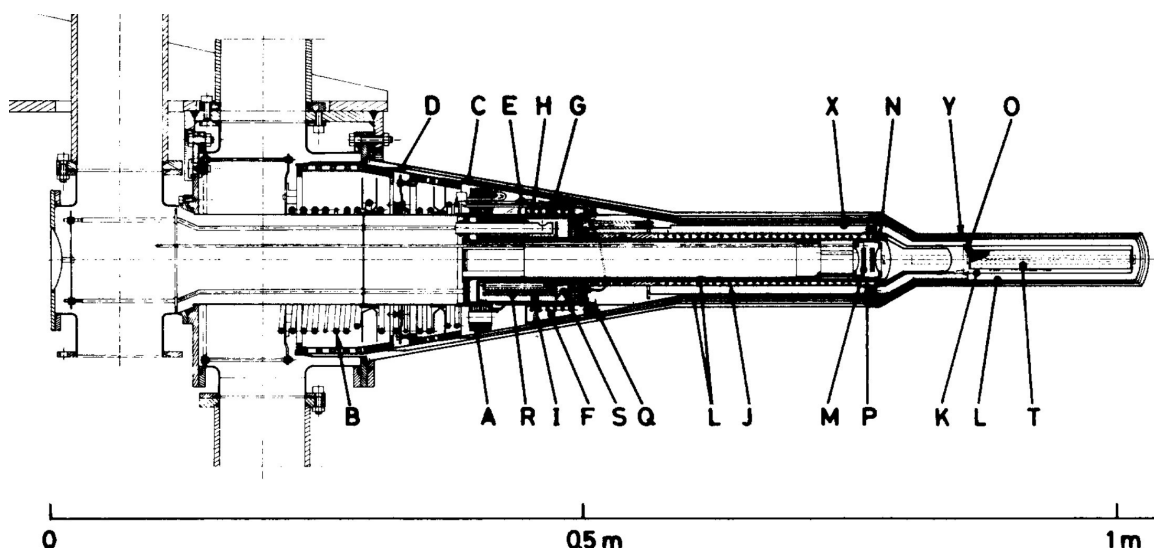


Figure 3.1: A schematic of the Hifrost polarized target, taken from the original publication describing it[Nii76], with the critical components labelled: **A**) separator, **B**) counter-current heat exchanger, **C**) outer heat shield, **D**) inner heat shield, **E**) 1K valve, **F**) evaporator (1K pot), **G**) condenser impedance (capillary), **H**) bypass valve, **I**) still, **J**) final heat exchanger, **K**) mixing chamber, **L**) IVC chamber, **M**) *components since removed*, **N**) thermometers, **O**) dam, **P**) MC indium joint, **Q**) IVC indium joint, **R**) still heater, **S**) still heat exchanger, **T**) target material, **X**) microwave guide holder, **Y**) *components since removed*.

Two lines coming out of the downstream face of the separator allow the LHe to reach other parts of the refrigerator, with the flow carefully controlled by two needle valves. The lower line, called the 1K line, allows flow from the bottom of the separator into an open, annular pot called the evaporator. Of course, in order for helium to take this route the separator must be entirely cooled, since LHe cannot make it to the bottom otherwise. The upper line has no such restriction is therefore called the bypass, which allows flow from

the separator orifice³, beyond the evaporator and through an extended capillary terminating at the holding magnet coil. The purpose of the bypass is to quickly cool the thermal heat reservoirs supplied by downstream components at the beginning of a cooldown.

Liquid enters the evaporator by flowing from the separator through the 1K valve, and leaves via evaporation. The gas pressure over the liquid in the evaporator is lowered through the use of pumps, causing the helium to evaporatively cool to about 1-1.5 K (hence the naming convention *1K pot/valve/line*). As shown in Figure 3.1, the evaporator is located roughly halfway down the length of the refrigerator, and there are no additional liquid helium lines to control flow further downstream. However, once the evaporator cools below the superfluid critical temperature 2.16 K, a superfluid film creep transports helium out of the pot and downstream towards the refrigerator nose. This concludes the evaporative ⁴He cooling mechanisms of the polarized target, which in general serve as a precooler for circulated ³He in the dilution circuit.

While the target is operating as designed in thermal equilibrium, the bypass needle valve is closed and all sections of the refrigerator downstream from the separator are cooler than 4 K. The evaporator pump flow is determined by ambient heat load to the refrigerator, which is largely unavoidable⁴ since the entire target sits in a 300 K environment. The liquid is replenished by the 1K line, whose flow is controlled by the 1K needle valve to equal the liquid lost to evaporator boiloff. The liquid drained from the separator via the 1K line is replenished by liquid coming in to the whole system from the transfer line, whose flow is regulated by the difference in pressure at each end. As mentioned above, the delivery end pressure is regulated by the separator pump flows via the use of adjustable valves at the pump inlets. The withdrawal end pressure is controlled by pressurizing the vapor in the

³Since the LHe flowing through the bypass line does not need to flow through the sintered copper separator, it may be thought of as coming “directly from the transfer line.”

⁴Some of the heat load is controllable, such as the heat brought into the refrigerator by the circulating ³He gas and various E&M loads, but those are negligible compared to the ambient heat load, which is on the order of watts.

liquid helium dewar with an external helium gas cylinder. Since the dewar is generally kept at a constant pressure (a few PSI above atmosphere), in practice it is the separator pump flows that control the stability of the rest of the ^4He section of the refrigerator.

The ^3He section is designed to have poor thermal conductivity with the ^4He section, lest the base temperature of the MC be limited by the warmer evaporator. If the ^3He lines were left under vacuum while the evaporator operates at 1 K, they would eventually reach liquid helium temperatures, although not in any reasonable time. There are two methods to speed the cooling of the ^3He section and MC in particular: exchange gas and ^3He circulation.

The exchange gas procedure begins after the LTL is inserted in the refrigerator and before the evaporator reaches 1 K. The turbo pump on the IVC is valved out and the pressure is brought to 40-60 mbar with He gas, called exchange gas in this context. The purpose of the exchange gas is to mediate heat transfer from the MC, final heat exchanger and still to the superfluid-cooled IVC can surface. The exchange gas is purged from the system once the MC reads 20-40 K, because it becomes difficult to remove once it gets too cold.

Cooling the MC by ^3He gas circulation begins once the evaporator reaches 1 K. He gas from the ^3He storage tanks is used to pressurize the condenser line to about 1 atm, and becomes very cold since the condenser feeds into a tube that loops around inside the evaporator. The cooled gas then flows through the rest of the ^3He system, eventually cooling it down. This molar gas flow will be minuscule until the entire system is below 4 K since the impedances in the ^3He line are meant for liquid flow.

The principle of operation for the dilution refrigerator is explained in Section 2.6 and will not be reviewed here. In practice, the condenser, main flow impedance, heat exchangers, mixing chamber and still are all statically configured and can not be adjusted once the refrigerator is assembled. The only mechanisms to control the dilution circuit are the power dissipated through the still heater and the ratio of the two helium isotopes in the circulated mixture (as well as the total mixture volume). Additionally, on the Duke system there is a

^3He pump which can bring the condenser pressure above that of the storage tanks.

Power dissipated through the still heater is controlled with a standard power supply, where either the voltage regulates the current or vice versa. Either way, the power $P = VI$ warms up the still to 600-800 mK and preferentially boils away the ^3He gas.

The ratio of $^3\text{He}/^4\text{He}$ in circulation is easy to control initially if the storage tanks contain purely ^3He or ^4He . During recovery, it can be assumed in most conditions that the ^3He purity in the boiloff from the still exceeds 90% and can be stored as “concentrated” ^3He . After the ^3He is recovered, the rest of the mixture is captured in a “dilute” or “ ^4He ” storage tank. The surest way to be confident of the contents of any one storage tank is to sample it with an RGA (see Section 4.4.5).

3.2 Holding Coil

In theory, the holding coil should be cooled by superfluid ^4He from the evaporator as described above. As expanded upon in Section 4.7, we do not see a superconducting coil unless the downstream end of the refrigerator is being coiled by liquid flow through the bypass line. A resistance measurement, made with a constant current supply and an ADC, informs us when it is safe to begin ramping up the holding magnetic field.

There are two sets of hardware that perform this task, with the simplest being a single Oxford module that contains the magnetic power supply, programming, quench protection and load. Once the coil is superconducting, the leads are disconnected from the ohmmeter and connected to the power supply, which is slowly ramped to the operational current.

3.3 NMR

The NMR system that measures the polarization is only set up to operate at the polarizing magnet field, 2.5 T. The NMR is connected and tested for a low-noise signal using an external oscillator crystal before the refrigerator is assembled. Once the MC is cold and the polarizing field applied to the target material, the NMR can measure a proton polarization of around a percent and a deuteron signal of a fraction of a percent.

Polarization measurements are carried out for the duration of the DNP procedure until the target is put into frozen spin mode at 0.5 T. After the experimental run, the polarizing field is returned so another polarization measurement can be made, allowing all polarizations during run time to be interpolated.

3.4 Microwaves

The microwave guides required for DNP are ready before the cooldown begins, tested with a microwave frequency counter and power meter. In practice, the EIO providing the microwaves outputs tens of watts of power, and is cut down by the use of microwave couplers before channeling the microwaves into the polarized target.

The microwave guides can be connected to the refrigerator any time after cooling begins. Microwave power is sent to the MC after the NMR signal has been acquired and the MC temperature is $\mathcal{O}(100 \text{ mK})$. Due to the way the EIO works, there is a relationship between the output frequency and power, so the MC temperature should be monitored while the microwave frequency is swept for the optimal polarization.

Chapter 4

Equipment Commissioning

“ When I started low-temperature experimental work in graduate school and wanted to know “how to do it,” I was struck by the abbreviated “experimental detail section” of most publications that simply stated the sample was mounted in the test apparatus, leads were attached, and the measurement made. But try to “simply” do that. The details are everything.

”

Jack W. Ekin, *Experimental Techniques*

Before the polarized target can be used for a data taking experiment, each subsystem must be commissioned independently to ensure it is in working order. In many cases, the subsystems had to be repaired or entirely rebuilt as a result of the early commissioning results.

4.1 Electronics and Instruments

The three primary measurements used to monitor an operational dilution refrigerator are thermometers, pressure gauges and mass flow meters. Instruments of each type come in several varieties, usually to access a different order of magnitude for that measurement.

4.1.1 ^4He Thermometers and Wiring

The ^4He thermometers connect through a hermetically sealed feedthrough on the back of the refrigerator next to the shield pump port. Lakeshore Cryotronics' AWG 36 Quad-Lead cryogenic wire is soldered to the reverse side of the connector and fed between the copper baffles to the separator and evaporator annuli. The wire is protected by non-fraying, braided fiberglass sleeve to keep the wire's polyvinyl formvar insulation from being scratched by sharp edges in the refrigerator, including the holding magnet leads and copper heat exchangers[LSC].

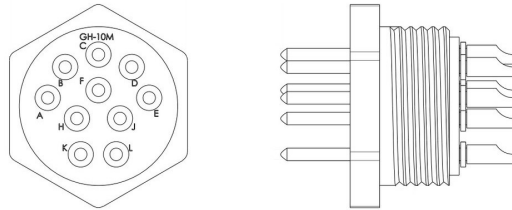


Figure 4.1: The ^4He wiring connector: a 10-pin feedthrough on the back refrigerator flange. The green o-ring seals the circumference of the feedthrough and is tightened with the black locking mechanism. The drawing and pin out of the ^4He feedthrough was provided by Ice Oxford technical support.

All thermometers on the separator and evaporator are Lakeshore Cryotronics DT-670 silicon diodes in SD packages. The diodes are good choices for the warmer parts of the refrigerator because there is a linear voltage reading with temperature from room temperature

down to 25 K and a highly-sampled curve (resolution as fine as 0.1 K) from 25 K down to 1.4 K. See Figure 4.2 for details.

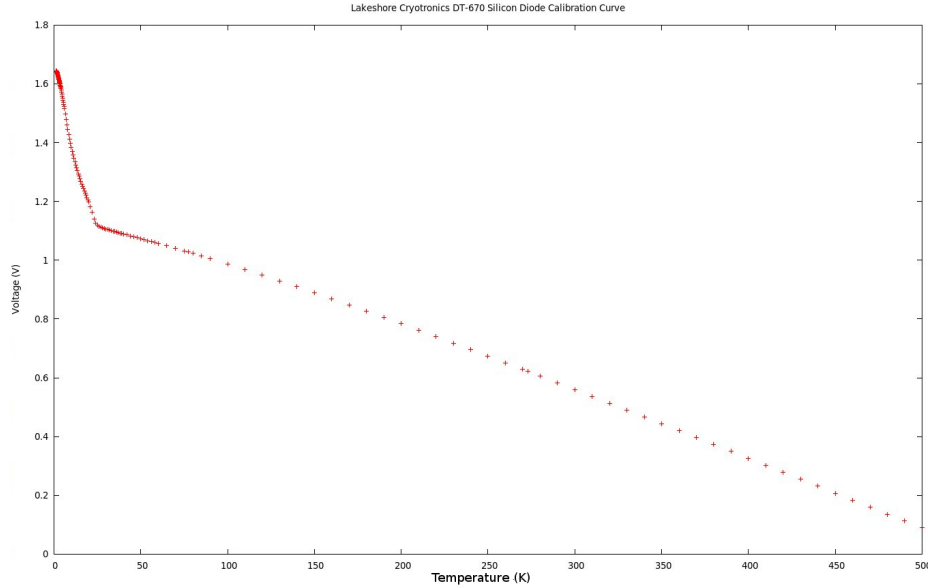


Figure 4.2: The calibration curve for the Lakeshore DT-670 silicon diode[Cry16].

The SD package leads are soldered to Lakeshore’s AWG36 Quad-Lead cryogenic wire. The leads are about 380 microns wide by 100 microns thick, so they must be handled with care during heat sinking and soldering.

We decided to configure two-wire solder connections instead of four-wire connections for all diodes in the ^4He section of the refrigerator in order to make the most out of our limited 10-pin connector (Figure 4.1). Normally, four-wire configurations have less measurement error associated with them because the resistance of the leads do not influence the measurement. This does not affect the ^4He section of the refrigerator, and justification is shown below for the special case of $T = 6.5\text{ K}$, the temperature at which the voltage response changes the most for some change in temperature[Cry16]. From the Lakeshore documentation, we know at 6.5 K:

$$V = 1.50 \text{ V}, \frac{dV}{dT} = -36.9 \text{ mV/K} \quad (4.1)$$

For a resistance of 100Ω , a very conservative bound for any reasonable sum of cable, patch panel and connector resistances, and the recommended excitation current of $10 \mu\text{A}$, the voltage and corresponding temperature error is

$$V = IR \quad (4.2)$$

$$= 10 \mu\text{A} \times 100 \Omega \quad (4.3)$$

$$= 1 \text{ mV} \quad (4.4)$$

$$\Rightarrow \mathcal{E} = \frac{1 \text{ mV}}{36.9 \text{ mV/K}} = 27 \text{ mK}, \quad (4.5)$$

where \mathcal{E} is the error in temperature which is certainly within the level of precision we need for the ^4He thermometers.

Until November 2015, there had been only one diode pressed against the upstream surface of the separator and secured with teflon tape. We later augmented the reading with a second diode, such that one was placed at about 30% of the height of the separator and the other was around 70% of the full height. The idea was to have a “two-point separator level probe” that would tell us when we were overflowing LHe or about to run dry. Instead, we found the two diodes mostly tracked one another during the initial cooling, as shown in Figure 4.3a, and that the upper diode more tightly coupled to the helium gas being pumped out of the refrigerator from the upstream ^4He sections at liquid temperatures (Figure 4.3b).

When we received the refrigerator from Geesthacht in 2012, it came with a DT-470 silicon diode and a custom level probe installed in the evaporator. We upgraded the diode to

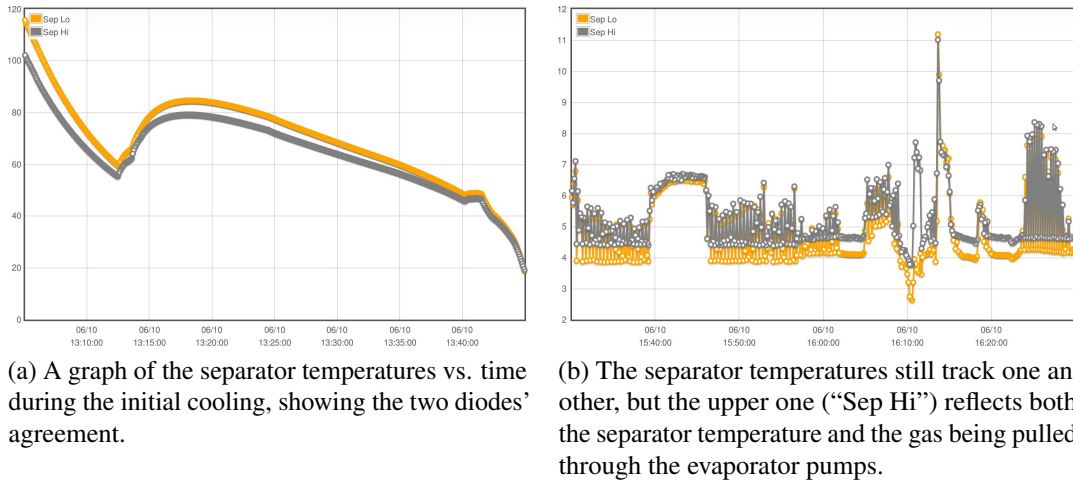


Figure 4.3: Graphs of the separator temperature, in K.

a DT-670, which has a lower temperature reading floor, and tried many times to get the level probe to work. Without documentation on the probe, we could not determine if the probe had an automatic superfluid helium burnout protective resistor installed, and eventually uninstalled it and replaced it with a series of diodes.

The “evaporator 3-point probe”, the name given to the series of evenly spaced diodes submerged in the evaporator superfluid, had the remaining six IceOxford connector leads allocated to it.

We chose three points on the probe because we wanted to know when the pot was being starved and when we were overflowing, as well as when we were trending toward either extreme. During stable operation, only the bottom two sensors are under liquid and the 1K valve would be throttled if the third sensor is ever submerged. Likewise, if the middle sensor is no longer under liquid, we know the pot is drying up and we need to immediately open the 1K valve to replenish the supply of LHe. We eventually plan for this feedback to go on an automatic PID loop, which would control a servo motor connected to the 1K valve, thus always maintaining a moderate amount of liquid in the pot, as was previously done with operation of the refrigerator at Geesthacht.

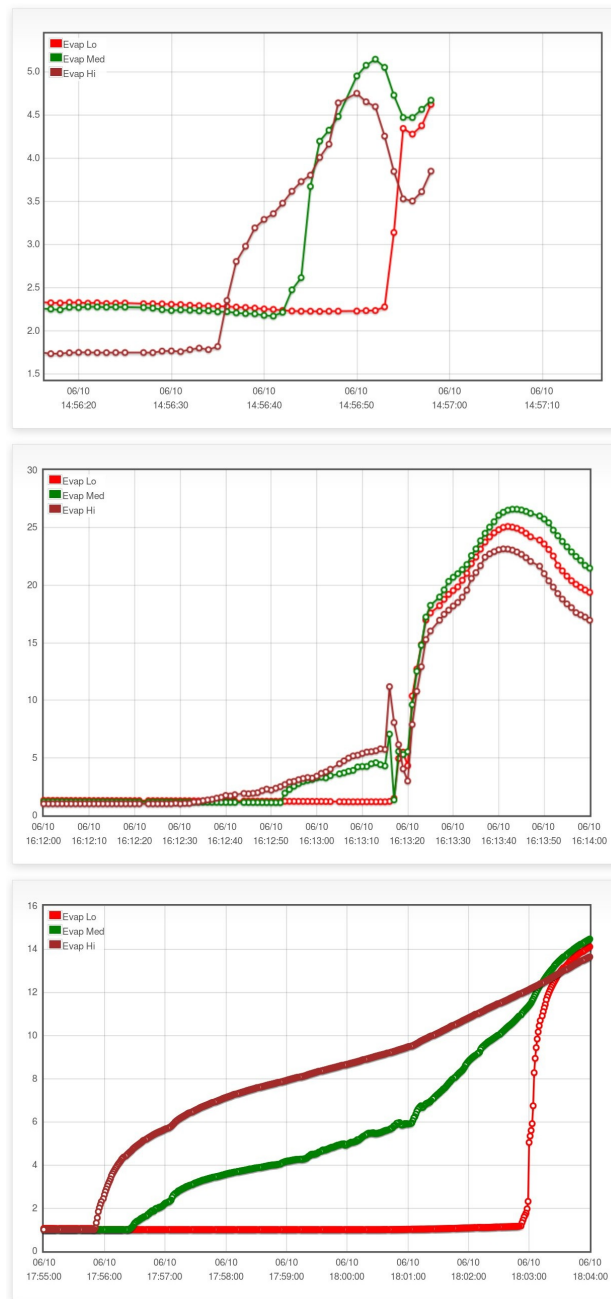


Figure 4.4: Results of the evaporator three point probe in action during the June 10, 2015 cooldown. On each occasion, all three sensors were under superfluid liquid when the pot began to become starved for helium (smooth, horizontal section). The order the sensors warmed up are high, medium, low, as expected for a level probe.

4.1.2 ^3He Heaters

The ^3He section of the refrigerator has two heaters and up to five thermometers. The thermometers are in the still and in the mixing chamber. Unfortunately, we know very little about the $100\ \Omega$ still heater because that region of the refrigerator was sealed before it arrived at UVa.

The MC heater is a 10 mil thick strip of Kapton (polyimide film) insulating heating element with a power output of 10 W over a 1 square inch surface, with the 2.5 micron thick heating element wrapped in FEP adhesive[OE16]. Its purpose is to provide the MC with a known heat load while running in steady-state dilution mode, from which the cooling power can be determined at that particular temperature. It also has the added benefit of speeding up the dilution mixture recovery process by boiling away the liquid at an accelerated rate during the end of a cooldown.

4.1.3 ^3He Thermometers

At the start of a run with a cold target load, the MC temperature is at 77 K. as the target material is stored under LN_2 . It is important to monitor this temperature and make sure it never exceeds 100 K or the paramagnetic centers in the target material may be annealed out, rendering the target unpolarizable. Once the 1 K section of the refrigerator is cooled, the temperature can be lowered to 20 K with vacuum chamber exchange gas. If the gas is left in the insulating chamber as the MC cools below 20 K, it will begin to condense and become difficult to pump out. Any residual gas left in the IVC during dilution operation will act as a heat exchanger between the MC and 1K pot, limiting the final MC temperature. It is clear that measuring the MC temperature is important during the first stages of the experiment.

Once the dilution mixture is ready to be condensed, the temperature is monitored until it reaches below the 0.9 K level, indicating the threshold of ^4He evaporation, 0.3 K,

indicating the threshold of ^3He evaporation, and down until it reaches its minimum frozen spin temperature. Also, without an NMR system operating at the holding field larmor frequency, the only measurement of the polarization decay is the measurement of the MC temperature. This makes a precise MC measurement tantamount to knowing the target polarization during an experimental run.

The MC is outfitted with several thermometers to make measurements across this temperature range, as well as extras for redundancy. The primary thermometer used above 4 K is a DT-670 silicon diode, the same model discussed in Section 4.1.1. The other thermometers are a germanium diode, a calibrated ruthenium oxide (ROX) sensor, and an uncalibrated ROX sensor. The refrigerator came with two additional Matsu-Chita sensors but no accompanying calibration curves, so we removed them.

The sensors are kept out of the beamline by a ring of perforated FEP tied to a copper insert, as shown in Figure 4.5. In addition to managing the sensor cables and localizing all sensors, this has the added benefit of anchoring the thermometers in place so the turbulence from the $^3\text{He}/^4\text{He}$ mixture does not affect their reading.

The calibrated ROX sensor is the primary thermometer in the MC. It has been calibrated by Lakeshore Cryotronics from 40 K down to 17.25 mK, and has its leads heat sunk to a copper block, which then connect to the refrigerator's four pin TCS connectors.

4.1.4 Flow Meter Installation and Calibration

Flow meters have three general purposes on Hifrost:

1. measuring LHe consumption through the separator
2. calculating the heat load to the evaporator
3. determining the circulation rate (and therefore cooling power) of the dilution refriger-

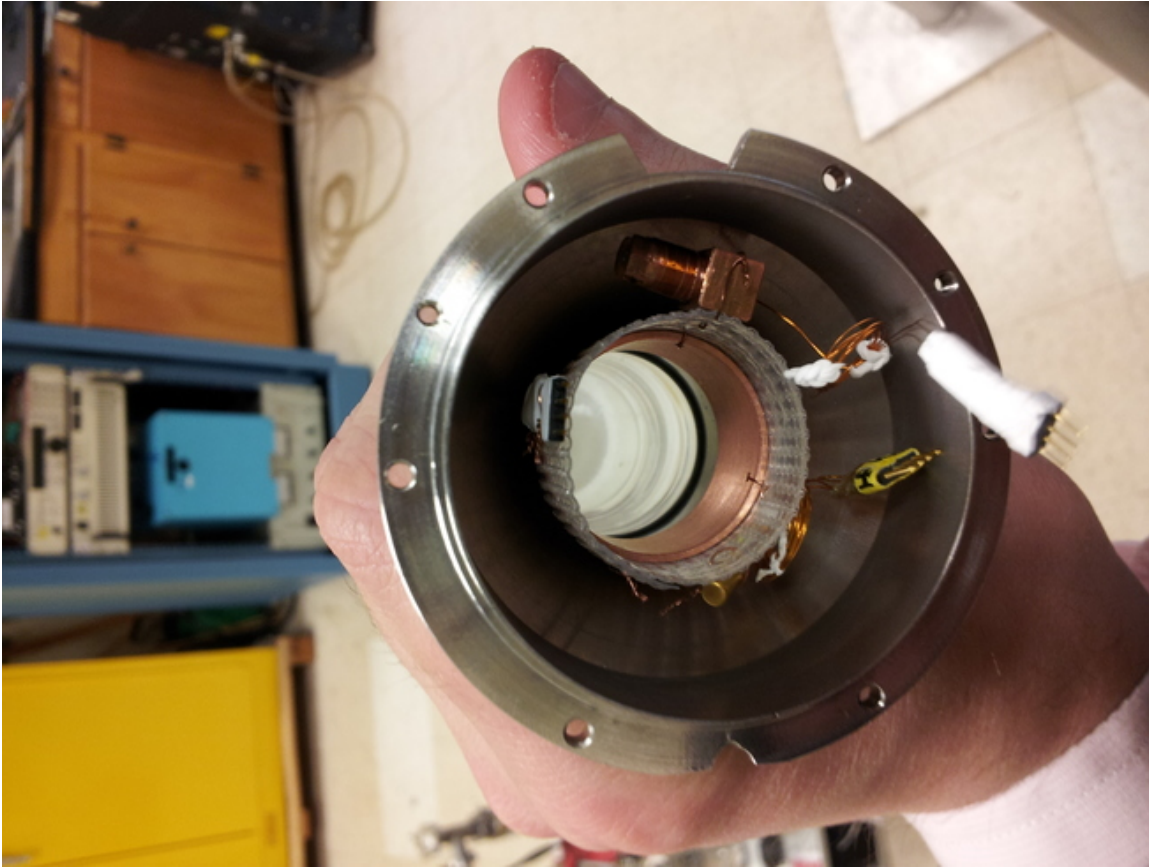


Figure 4.5: Mixing chamber thermometers anchored to FEP insert. Clockwise from top: calibrated ROX, uncalibrated ROX, germanium diode, silicon diode.

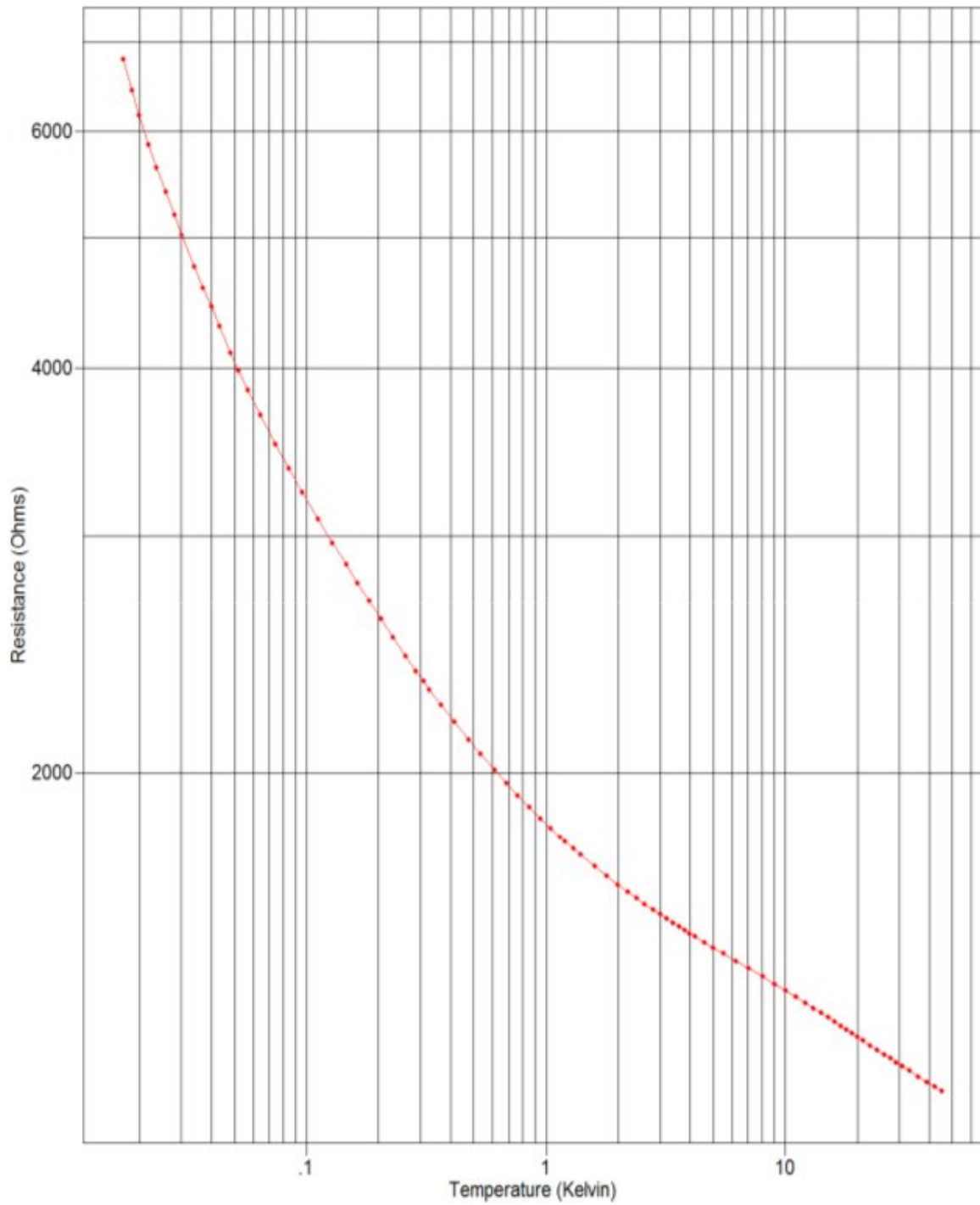


Figure 4.6: The calibrated ROX curve provided by Lakeshore serves as the primary measurement of MC temperature.

ator

The consumption of LHe is best measured with a level probe in the 100 L dewar. This method accounts for not only liquid consumed by the refrigerator, but also liquid lost due to heat leaks in the dewar (including transfer lines) and due to heat brought in by pressurizing gas. Sometimes, it is better to isolate only the helium used by the refrigerator, which can be done by monitoring the gas flow through the separator pumps and using the liquid to gas expansion ratio of helium (approximately 1:750).

The liquid boiled away from the evaporator can be calculated from the gas flow through the evaporator pump in a similar way. Additionally, we can estimate the heat load to the evaporator by assuming all energy goes into the latent heat of evaporation of the evaporator helium. This crude but effective approximation accounts for about 1 W of heat load for every 15 SLPM of gas flowing through the pump.

Almost all Hifrost flow meters are of different makes and models, with the oldest being 30+ year old Leybolds and the newest being a Teledyne model bought in 2014. They are mostly read out into homemade integrated circuits that feed various front panel displays, but we were able to tap the voltage lines to get a reading proportional to the flow through trial and error.

Some flow meter readout front panels only read in units of volts, and others could only display a limited range (up to 20 SLPM), despite the analog outputs of the corresponding flow meter having a larger range. By connecting the separator, shield, and evaporator flow meters in series, a known amount of helium gas flow was passed through simultaneously and the output measurements recorded (Figure 4.8).

The Duke evaporator flow meter is rated for a maximum flow of 100 SLPM despite the maximum flow for the evaporator pump stack exceeding 1000 SLPM. To prevent a high pressure buildup and subsequent pump damage, a normally-closed, electronically actuated

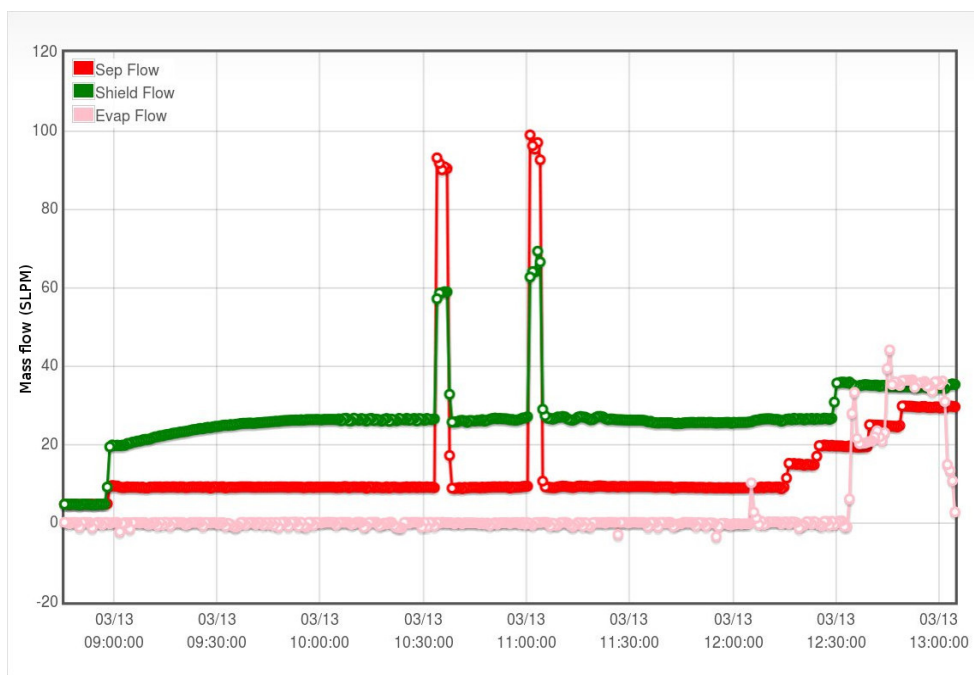


Figure 4.7: The flow meter readouts on each system are partially commercial and partially homemade solutions. Analog output voltages were tapped from the circuits connecting the readouts to the flow meters and fed to an ADC for logging (see Section 4.4.7 for details). The spikes reflect a sudden increase in flows, illustrating the full range of the DAQ.

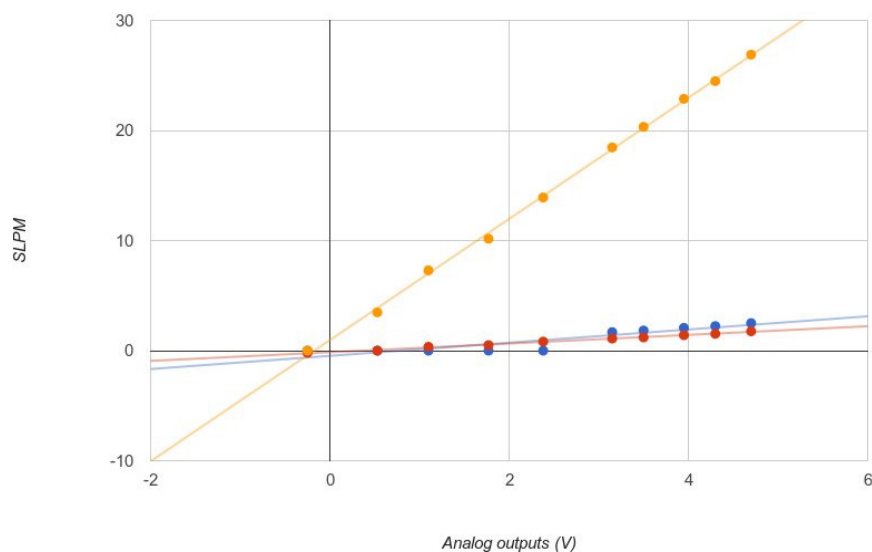


Figure 4.8: The analog output voltage was linear with the available front panel reading in the evaporator (blue), shield (red) and separator (yellow) flow meters, so extrapolating to off-scale measurements was justified. Note that the evaporator flow meter reads zero until the analog output reaches about 3 V.

valve was plumbed in parallel to the flow meter and set to open when the flow meter reads over 100 SLPM, an unusual but possible scenario.

4.1.5 Pressure Gauge Installation and Measurements

Vacuum and pressure gauges, both henceforth referred to as “pressure gauges”, exist in many places on the Hifrost system, including: delivery and buffer dewars, both pump stack inlets¹, ³He gas storage tanks, throughout the ³He gas manifold, the evaporator pump line, both separator pump lines, both IVC and OVC manifolds, the mash cleaning system, helium gas distribution manifold, the portable vacuum rise test system, manifolds internal to leak detectors, the pneumatic gate valve controller and ISO-100 flex lines.

Several of these subsystems have multiple gauges for different vacuum or pressure regimes corresponding to different operational scenarios, and others have pressure management without an actual gauge (pressure relief valves, internal blow off valves, emergency popoff valves).

Instead of enumerating every gauge on the system, we discuss some general uses of the pressure gauges and give examples of how they are installed and used.

Over-pressure gauges Helium gas cylinders and the manifolds they feed are not adequately sealed for vacuum purposes, and as such should never have a pressure below atmosphere. The pressure gauges used on these systems only read in excess of 1 atm and usually serve to warn users of dangerously over pressured volumes. There are also some occasions, such as backfilling a critical system, when a gas line cannot have a pressure below an atmosphere without becoming contaminated by air. In these cases, the over-pressure gauges indicate how fast one can fill a volume without risking the compromise of the vacuum line.

¹In some cases between pumps.

Combination gauges A combination gauge is an over-pressure gauge that can also read “negative” pressures (i.e., those below 1 atm). These simple mechanical gauges represent vacuums from several psi above atmosphere down to 30 inHg below atmosphere on a linear scale. They are useful for course measurements on large pumping lines, where even a few psi can translate to hundreds of newtons of force on the vacuum components.

Capacitance diaphragm gauges A diaphragm vacuum gauge measures pressure using the straightforward the mechanical principle $P = F/A$. The force applied by the measured gas is sensitively detected by a capacitance sensor and is independent of the gas species [Tec12]. Since it becomes more and more difficult to measure this force at lower pressures, the diaphragm is only useful from 1 atm down to about 1-10 mbar. This is ideal for vacuum rise tests, which measures the pressure of an unknown combination of air and helium, and while using IVC exchange gas, which functions between 10-50 mbar.

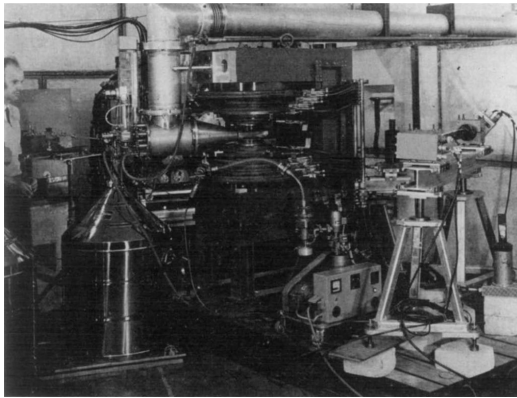
Pirani gauges Vacuum measurements between 10^{-3} mbar and 10 mbar are made with a pirani gauge using principles of thermal transfer. In a pirani gauge, a conducting wire is held a fixed distance from a thermally sensitive wall and heated up by passing a known current through it[PV16]. The heat transfer between the wire and wall is proportional to the gas pressure in the range that the pirani gauge is useful. The liquid helium saturated vapor pressure curve provides a cross check for the evaporator thermometers down to about 5×10^{-2} mbar, so the pirani vacuum gauge in a sense doubles as a sanity check for evaporator temperature.

Cold-cathode gauges The OVC and IVC volumes are evacuated by a turbomolecular pump station and, later on, cryopumping. The pump stations can reach pressures down to $\mathcal{O}(10^{-5}$ mbar) and cryopumping can reach two orders of magnitude lower. To measure these extremely low pressures, we rely on the operating principle of the cold cathode gauge,

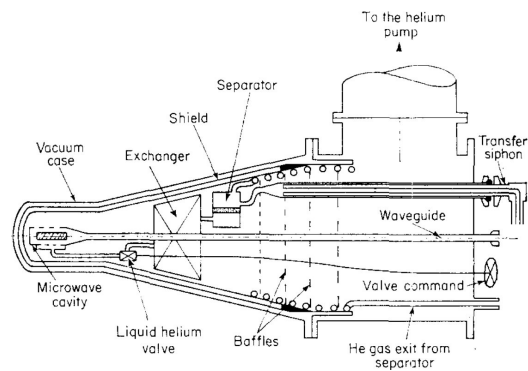
where electrons are generated at a cylindrically symmetric cathode and fall to a wire anode at the gauge's central axis[PV16]. The electrons ionize gas molecules during collisions, leaving behind a gas discharge current which is collected and calibrated to the pressure of the chamber. In order to maximize the probability that the electrons will strike a gas molecule, the whole gauge is encased in a permanent magnetic field which cause the electrons to spiral towards the anode, greatly increasing the chances of a collision. Operationally, users must take extreme caution around this permanent magnetic field and be sure not to rest the gauge near electronics, steel tools or other equipment that could be suddenly affected by the field.

4.2 ^4He Cryogenics

The 4 K section of the refrigerator was inherited from a previous CERN design developed by P. Roubeau[Nii71a] and shown in Figure 4.9a, which was used to precool a continuous ^3He evaporation target. The precooler has been modified enough to introduce new terminology and discussion, but the Roubeau cryostat serves as a useful starting point.



(a) A 1966 photo of the cryostat.



(b) Precooler schematic.

Figure 4.9: The ^3He cryostat used at CERN served as the foundation for the Hifrost ^4He precooler[Rou66]. The notable similarities (Hifrost equivalences) are the helium pump line (evaporator line), transfer siphon (LTL), separator, shield, liquid helium valve (1K valve), and valve command (needle valve).

Liquid helium first enters the warmest part of the refrigerator through a vacuum jacketed “L”-shaped transfer line (LTL) from a storage or delivery dewar into the top of an annular, sintered copper volume called the separator. A pressure differential caused by two separator pumps and a slightly pressurized dewar drives the liquid through the LTL. The first pump line, called the shield, is a copper coiled heat exchanger that makes firm contact with the inner wall of the OVC can, which acts as a sink for all the heat intercepted by the 40 K radiation shields. The second pump line, the counter current pump line², makes a tube-in-tube union with the ^3He condenser line, so the cold gas leaving the separator takes heat from the warm gas coming in from the ^3He manifold, hence the name *counter current*. Both lines operate around 1 atm using metal bellows compressor pumps.

4.2.1 Outer Vacuum Chamber

The outer vacuum chamber, or OVC, insulates the 4 K section of the refrigerator. It consists of five parts:

1. an inner stainless steel wall
2. an inner copper shield
3. an outer copper shield
4. an outer steel wall
5. an aluminum nose piece

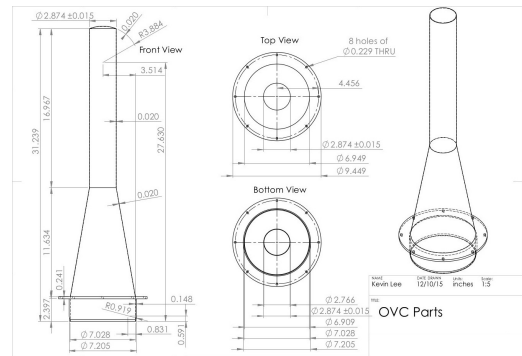
The inner wall is a cylindrical cap welded onto a heat-spun cone made of 0.5 mm thick stainless steel, with thin layers of evaporation-deposited copper and aluminum over it (see

²Unfortunately, this pump line has been given the confusing alternative name *separator line*, despite being one of two lines that pump on the separator.

Figure 4.10a), either for their thermal conductivity properties or as artifacts of brazing by the CERN workshop[Nii15b]. The inner diameter of the nose piece is designed to fit 500 microns from the next inward shell and within 1 mm from the inner copper shield, which is soldered to the base of the inner wall.



(a) A thin layer of steel was machined off the OVC inner can to reveal several deposited layers of metal composing the 0.5 mm thick wall.



(b) Drawings UVa's PTGroup made of a similar OVC from the same CERN workshop as the Hifrost OVC.

Figure 4.10: The OVC inner wall.

The outer copper shield is soldered over the conical base of the inner shield with a 5 mm radial clearance between them, so the three inner shells of the OVC make a single unit. The steel outer can is then placed over them and capped with the aluminum nose piece, which is held on by the OVC vacuum and sealed with a rubber o-ring. In the event of a sudden loss of vacuum and subsequent warming, rapid expansion of trapped gas may occur. In this event, the aluminum nose piece serves as an emergency pop off vent.

Since the copper shields are open at the downstream end, the volume bounded by the two steel cans and the aluminum nose piece form the outer vacuum chamber, which is evacuated with a turbomolecular pump before refrigerator assembly and throughout the cooldown. The vacuum is continuously monitored by a cold cathode gauge (see section 4.1.5), and never vented or backfilled during a cooldown.

4.2.2 Heat Leaks

If the refrigerator is operated in the same manner as it was at CERN, the separator compressors should pump at an approximately combined 20 SLPM gas under normal operation. During cooldowns up until 2015, we required a much higher flow in order to maintain the separator thermometers at liquid temperatures.

On March 2015, a cooldown was begun by running at the prescribed separator flows and measuring the equilibrium separator temperatures. The separator³ pump line was kept at 7 SLPM and the shield at 13 SLPM and the transient response of the thermometers was observed for just over 6 hours, shown in Figure 4.11. The separator asymptotically approached 25 K, indicating the system could neither reach nor maintain liquid temperatures at the prescribed separator flows.

In Figure 4.11 beginning at 15:45, we began increasing the separator flows in 3 SLPM increments at intervals of about 20 minutes until the separator finally fell to liquid temperatures at separator and shield flow rates of 30 SLPM and 25 SLPM, respectively. As shown in Figure 4.12a, the separator temperature responded to an increase in flows, but it never actually filled with liquid helium. The fact that we needed more than triple the prescribed flows was a strong indication that there was a heat leak to the 4 K section of the refrigerator.

In order to better characterize the 4 K heat leak, a DT-670 silicon diode was varnished to the inner shield to measure the shield temperature during runtime (Figure 4.13). The shield appears to behave properly, cooling down to around 50 K and not dropping below 43 K during the entire run.

In May 2015, it was suggested that the evaporator pressure may be related to the heat leak. A pressure of $\mathcal{O}(10 \text{ mbar})$ imparts a convective heat load between the 300 K back flange and all ^4He sections of the refrigerator. While no attempt was made to control the

³The *counter-current line* will be referred to as the *separator line* for the rest of this section to keep terminology consistent with the data logs.

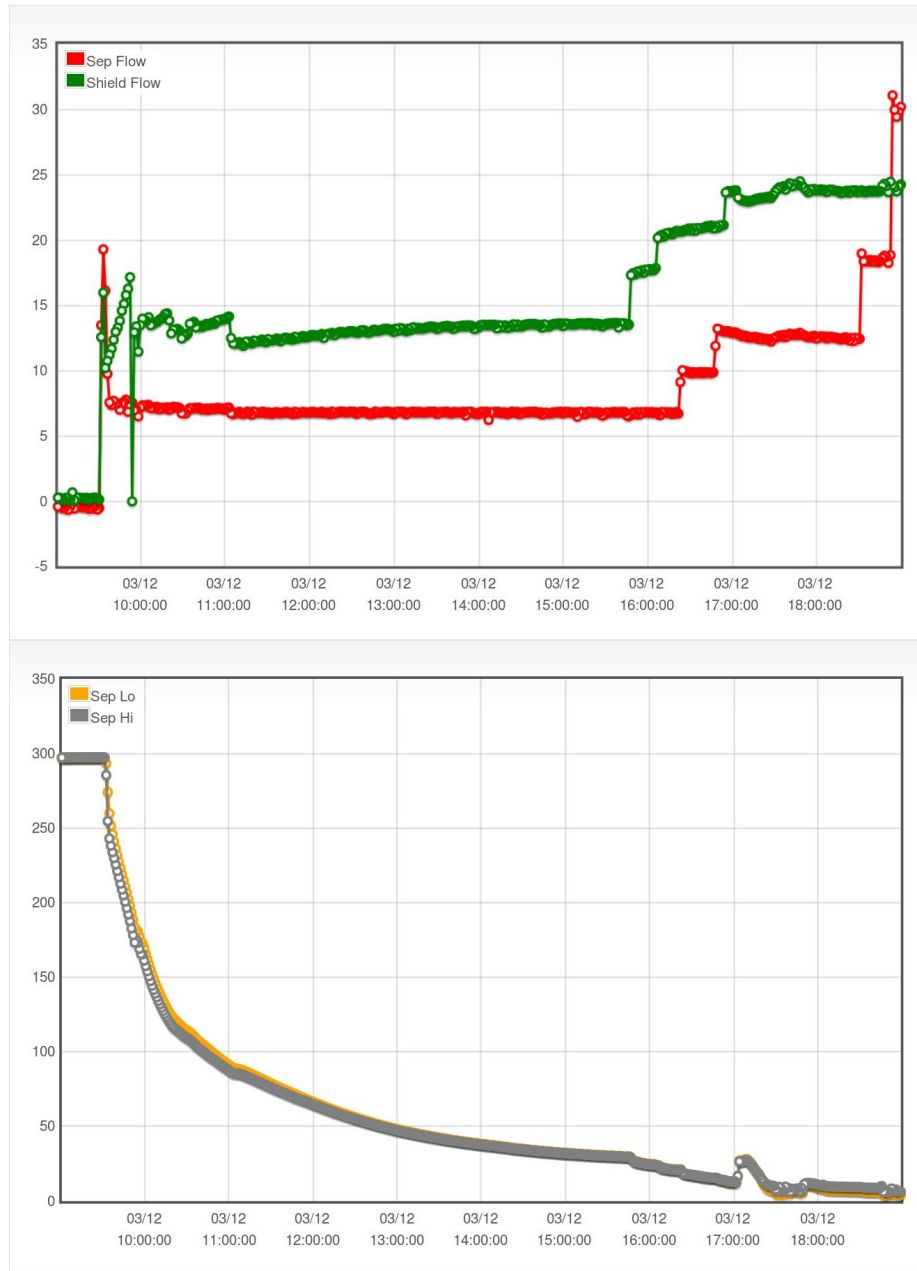
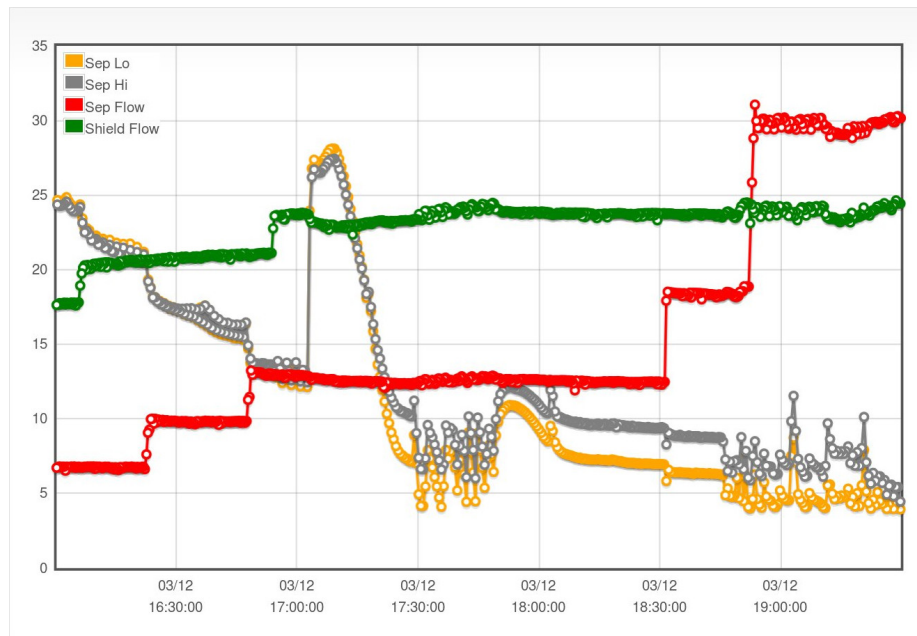
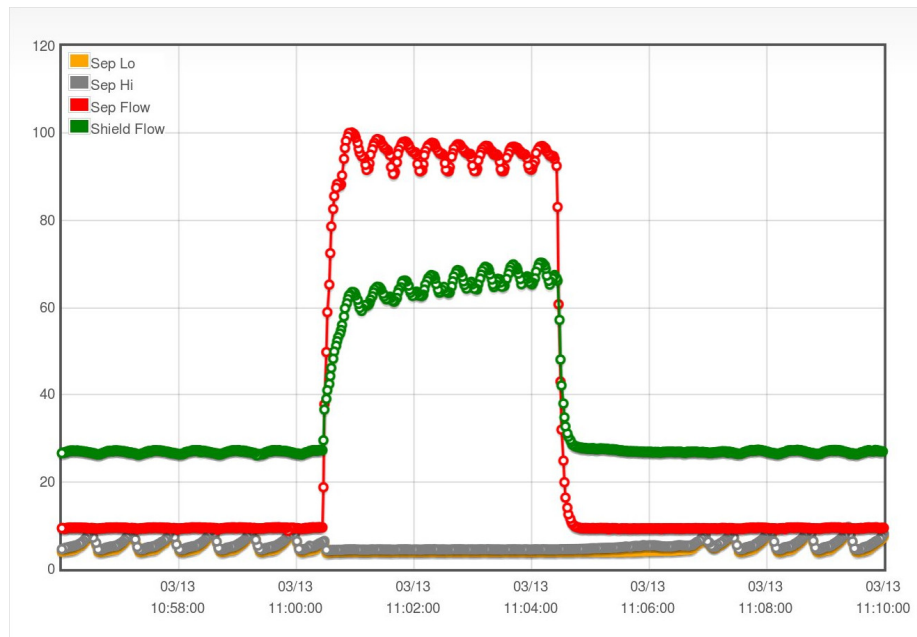


Figure 4.11: March 12, 2015 transient 4 K heat leak test: the upper graph shows the separator and shield lines' throughput in units of SLPM vs. time. The lower graph shows the temperature in K of the separator on the same time scale.



(a) The oscillating thermometer readings around 4-10 K represent liquid beginning to sputter in the vicinity of the separator, but not actually filling it. The temperature reading of the separator when filled with LHe is a steady reading around 4 K.



(b) The separator flows were momentarily pumped at maximum rate to confirm what liquid helium temperatures in the separator look like.

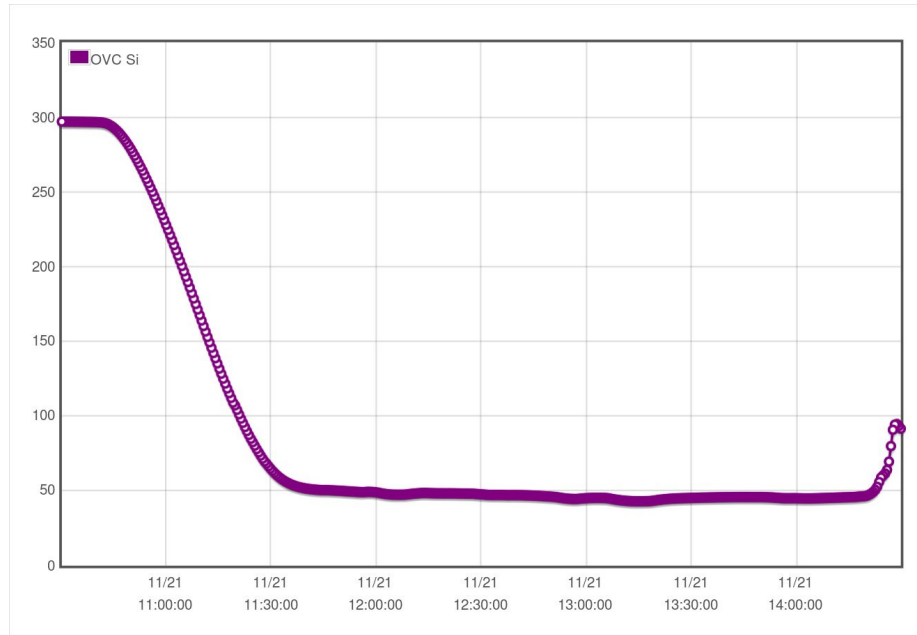
Figure 4.12: March 2015 transient 4 K heat leak test: the separator flows (in SLPM) and thermometer (in K) readings are on the same graph showing the effect of increasing the flows.



(a) The radiation shield thermometer is on the downstream end, farthest from the shield pumpout heat sink.



(b) The clearance is so small between the inner radiation shield and aluminum nose that a four-pin connector couldn't be attached directly to the diode leads. Instead, a length of cryogenic wire trails down to the OVC pump port where the connector is soldered.



(c) The temperature (in K) of the shield thermometer vs. time during a 5 hour cooldown.

Figure 4.13: A DT-670 silicon diode measures the temperature of the shield during cooldowns to determine if the heat leak was caused by a breakdown in the shielding.

evaporator pressure at Duke during the 2013 and 2014 cooldowns, as the evaporator pump stack was not fully operational, the pumps at UVa had been working and could meaningfully be monitored. Figure 4.14 shows we were able to maintain liquid temperatures at combined separator flows as low as 25 SLPM.

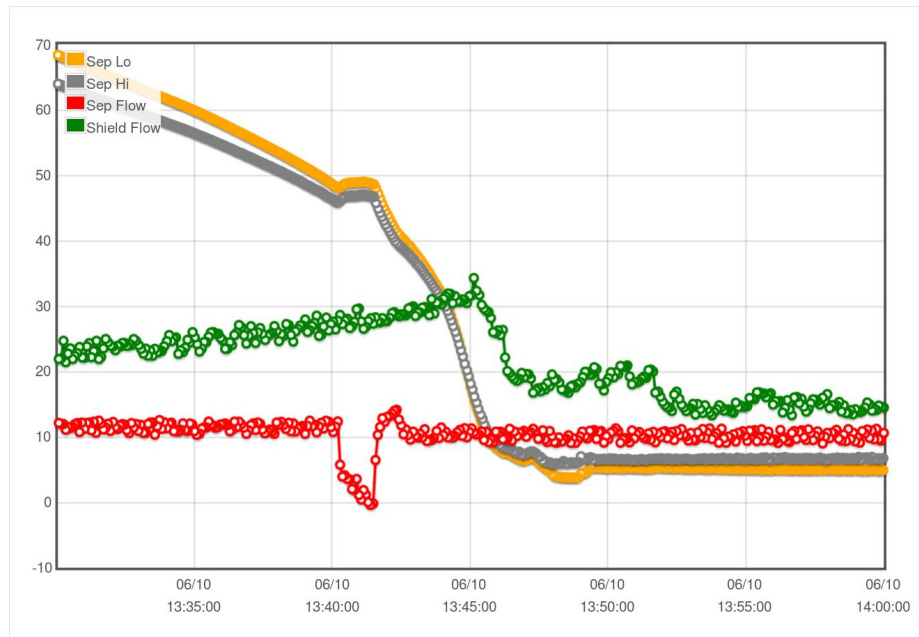


Figure 4.14: The separator was brought to liquid temperatures with much lower separator flows during the June 2015 cooldown, as seen when comparing this graph of separator flows (in SLPM) and temperatures (in K) with those in Figure 4.12a.

4.2.3 Multilayer Insulation (MLI)

One final attempt at solving the 4 K heat leak involved experimenting with multiple layer insulation (MLI). MLI is a stack of thin layers alternating between a highly reflective (low emissivity) surface, such as aluminized mylar, and a mesh of low thermal conductivity material such as silk or bridal veil. Incoming thermal radiation will reflect off the various layers of mylar instead of being absorbed by the surrounded, lower temperature system. In high vacuums, the successful application of MLI reduces radiative heat loads by an order of

magnitude more than the best alternative[Wei98].

The use of MLI in sections of the refrigerator other than the vacuum chambers is questionable because it is generally only used in environments at 10^{-2} mbar and lower. Studies which explore the variability of free parameters such as layer density and interstitial gas species don't present data above this high vacuum regime[Gu03], making our use difficult to justify. However, there exists some data, as in the graph in Figure 4.15, which suggest the evaporator pressure may be just at the high pressure end where MLI is useful.

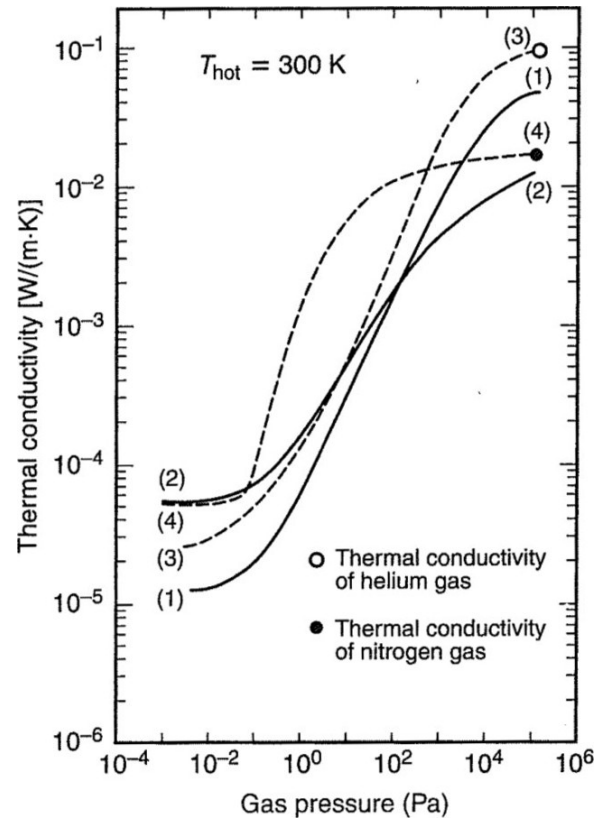


Figure 4.15: Graph of apparent thermal conductivity of various MLI[Eki06]. Plot 1 is most comparable with the Hifrost MLI: aluminum foil spaced with fiberglass paper and residual helium gas. It shows a steep curve in the 1-100 hPa range, which is around the pressure of the evaporator under normal operating conditions.

The refrigerator arrived with insulation in three places; inside the main refrigerator volume against the back flange, around the ^4He pumpout in the same vicinity, and around

the upstream butt weld of the inner OVC wall (drawing in Figure 4.10b). The MLI inside the refrigerator was in very poor shape, so we decided the best room for improvement was the back flange and around the ^4He pumpout, with the latter being the easiest place to start.

Alternative sheets of aluminized mylar and silk were cut out to the shape and size of the steel retaining sheet (see Figure 4.16c) that came with the refrigerator. The silk was cut slightly larger because the fringe effects of aluminized layers touching can be devastating to the overall effectiveness of the MLI, which has a factor of 1000 greater thermal conductivity along the surface of the layers than normal to them[Wei98].

The MLI was installed in early June 2015 and was shortly after part of the cooldown that demonstrated low separator for the first time. However, due to the fragile nature of the MLI and particularly the tendency for thread to tear the aluminized mylar, the MLI did not survive the subsequent repeated installations as we attempted to install properly insulated holding magnet leads. Instead of postponing the magnet cooldowns, we temporarily removed the MLI and carried on, only to find the removed MLI had no effect on the ^4He heat leak. Given the technical difficulties of making another MLI blanket, and the greater difficulties of making a second blanket for the ^4He back flange, the MLI project has been discontinued.

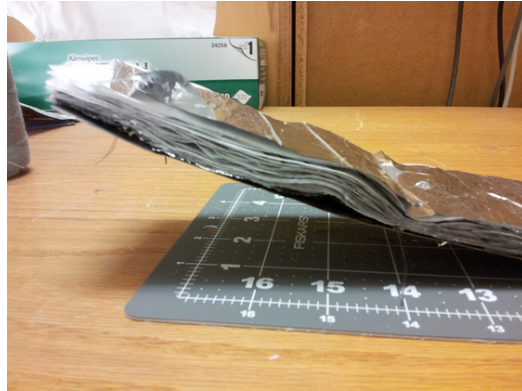
4.2.4 Bypass Capillary

The bypass capillary is a narrow tube separated from the LTL's incoming LHe by a needle valve on the back of the refrigerator. It is called a bypass because it crosses over both the separator and evaporator and heads downstream to the holding magnet coil. Its purpose is to cool the large thermal mass downstream directly, which is more effective than relying on the low thermal conductivity of stainless steel.

The bypass capillary resides in the annular space between the IVC and OVC walls and designed to have an outer wall major axis of less than 500 microns. A capillary was installed



(a) The aluminumized mylar and silk were cut with a 45 mm rotary cutting blade and a self-healing cutting mat.



(b) Aluminumized mylar layers of the finished MLI seen from the side are spaced by silk.



(c) The finished MLI, sewn to the steel retaining sheet with non-conducting thread.

Figure 4.16: The Hifrost MLI blanket.

in early 2015 that did not meet the specifications, with the results shown in Figure 4.17. The collision between the OVC inner wall and this bypass capillary prevented the OVC flange from coming within a few inches from its mating refrigerator flange with the OVC at 1 atm.

After a new coil was wound at UVa in late 2015 (see Section 4.7), a newly designed bypass capillary made of 1 mm OD, hypodermic stainless steel tubing with a wall thickness of 125 microns. The tubing was flattened between rollers to give a minor axis of 500 microns before being soldered to the IVC can.

While within the specification of the IVC-OVC wall gap, wrapping the bypass with 71 micron thick teflon tape and installing the OVC around it shows a severed section where there is still a touch (see Figure 4.18).

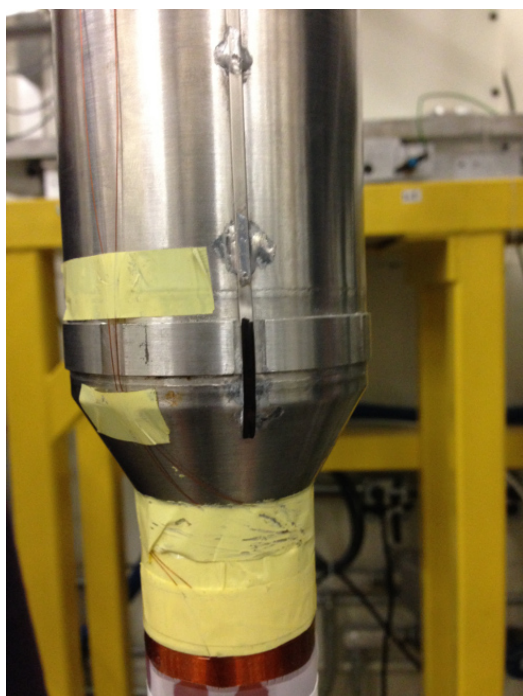
In theory, this thermal connection between the bypass capillary and inner OVC wall should constitute a significant heat leak, but in late 2015 we were able to demonstrate that the IVC holding coil can fall below superconducting temperatures, anyway.

4.3 NMR

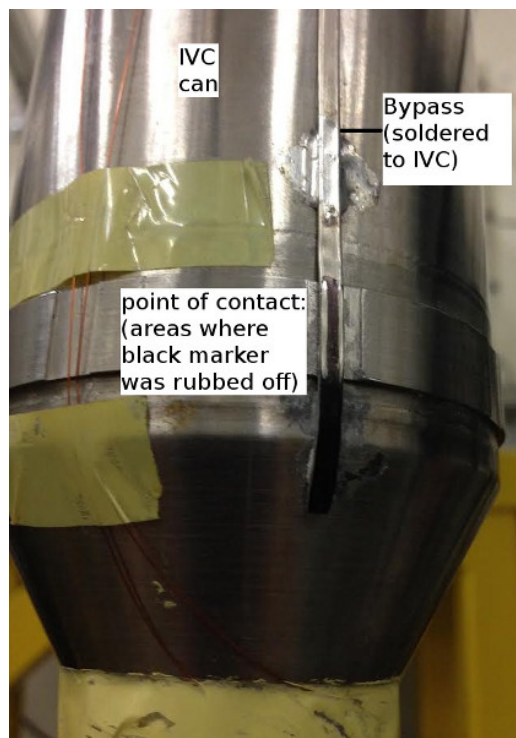
The theoretical underpinning of how the NMR works is covered in Section 2.4. This section discusses the process of building the NMR tower, hooking up the electronics and getting everything operational. Much of the discussion and figures are from a technical document made for UVa's Polarized Target Group[Duv15c].

4.3.1 Yale Card Housing

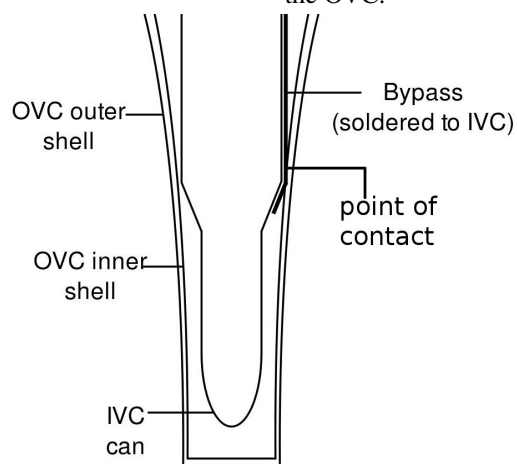
The Yale Card housing, sometimes called the NMR housing, is the physical structure that houses the Yale Cards, has ports for electronic interfaces, and maintains constant temperature through cooling. Since it forms the platform on which the Q-Meter resides, it often defines where the NMR is said to be “located” in the lab.



(a) The 2015 installed bypass capillary before the OVC was installed over it, with a protruding section painted by black marker.



(b) The capillary after the OVC was installed and subsequently removed. Note the area where the black marker was rubbed off by the collision with the OVC.



(c) Diagram showing where the touch occurred.

Figure 4.17: A collision between the bypass capillary and OVC inner wall.



Figure 4.18: The bypass capillary was installed at UVa in late 2015. This angle shows how low profile the capillary needed to be in the radial direction in order to fit within the target's geometric constraints.

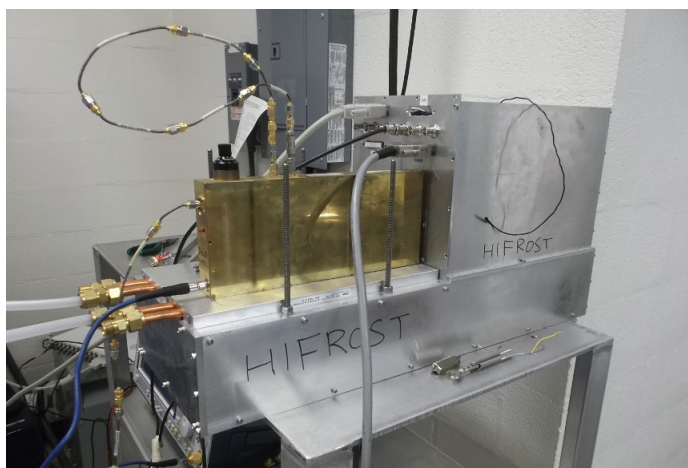


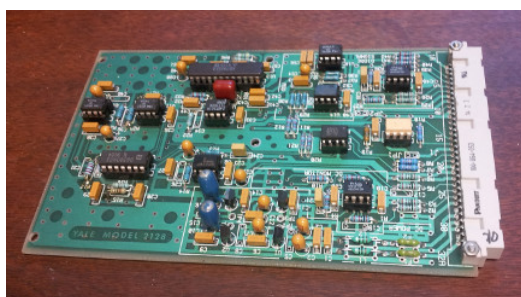
Figure 4.19: The finished NMR system, complete with housing, electronic connections, water cooling, Q-Meter and Yale Cards.

The housing must be made of metal to form a Faraday cage that protects the sensitive RF signal from noise in the lab. While our housing, shown in Figure 4.19, was completed without documentation or technical note, it is surmised aluminum was picked for its low cost and mass density, as well as being easy to machine. Standard copper plumbing ensures effective heat transfer between the coolant and the Q-Meter plate, which itself was made just long enough to fit the Q-Meter.

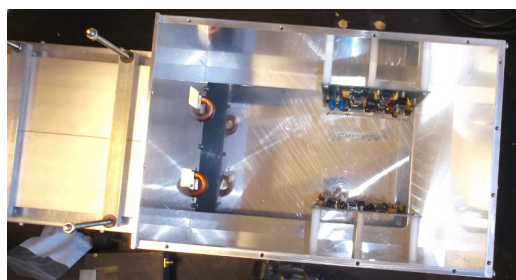
Threaded rods are installed to fasten horizontal aluminum bars that keep the Q-Meters in place. Holes are drilled in the front facing panel for signal outputs, the DIO connector and the power connector. Thermistors are attached nearby to monitor the thermal stability of the Q-Meters.

4.3.2 Housing Electronics

The Yale Cards themselves are installed inside the housing and secured with standoffs for thermal and electronic isolation. Each connects to a Q-Meter, signal output feedthroughs and the power supply through a 64-pin, two-row DIN style “Burndy” connector. The electronic connections were made by copying those in a Liverpool Yale Card module, which is a gold plated box that looks like a Q-Meter but houses a Yale Card and the appropriate connections.

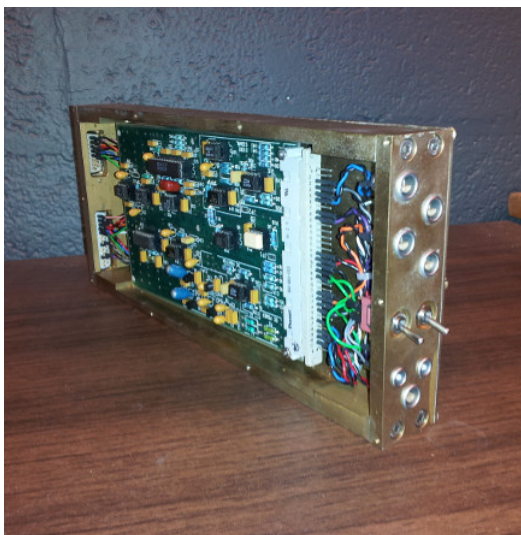


(a) A Yale Card taken out of the housing.



(b) A look down the Hifrost housing during installation.

Figure 4.20: Yale Cards in Hifrost.



(a) The front panel of the Liverpool module has three pin Lemo connectors for the signal, gain, and other connections.



(b) The connections from the 15-pin and 25-pin connectors to the Yale Card inside of the Liverpool module were traced.

Figure 4.21: The Liverpool Yale Card module.

The Yale Card connects to the Q-Meter and DIO circuit via 25-pin DSub connectors, and to the power supply via a 15-pin DSub connector, both of which connect to feedthroughs on the front panel. BNC bulkhead connectors are wired to their respective pins on the Yale Card so we can read them on the oscilloscope and NMR DAQ.

One option we decided to forgo in the Yale Card housing was the manual gain switch override. While all other connections between the Yale Card, Q-Meter, power supply and signal outputs are straightforward, the gain is controlled by two parallel mechanisms: a 5 V TTL signal and a manual contactor (topology shown in Figure 4.22). We did not know whether we would have access to the Gamma Vault while adjusting the NMR from the DFELL counting room, so for simplicity we only built the coaxial gain switching functionality into the system.

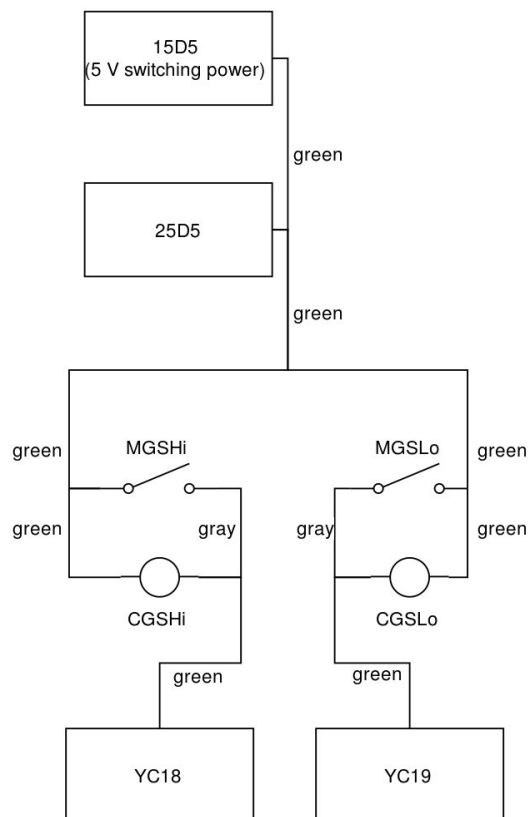


Figure 4.22: The electronic topology for the parallel mechanisms, manual gain switching (MGS) and coaxial gain switching (CGS), controlling the NMR signal high and low gains in the original Liverpool Yale Card module[Duv15c].

4.3.3 $\lambda/2$ Cables

As mentioned in Section 2.4.2, the $\lambda/2$ cable is easier to properly hook up in theory than in practice. The chief problem is the desire for continuous cable length variability, but only a finite number of fixed length cables are available for tuning the Q-Meter circuit. Historically, the problem has been brute forced by having dozens of very small, spare SMA connectors available and, once a proper length has been found, making a custom size $\lambda/2$ cable for that system. The problems with this method are there is no guarantee that the required parts will be available, each connection introduces a chance to have a faulty connection, and there are more cables and connectors around to keep track of. Moreover, if a single cable is in place and needs to be shortened slightly, the process of hunting for a combination of shorter cables to nearly match the longer one begins all over.

The Hifrost group aimed to solve this problem more systematically, utilizing the system of binary counting to make any length of cable, in integer number of cm, with as few SMA connections as possible. Variable length SMA components are then used to fine-tune the length within 1 cm if desired. For example, Table 4.1 shows the binary representation for the first eight cables in the binary sequence.

Cable length (cm)	Binary representation
1	00000001
2	00000010
4	00000100
8	00001000
16	00010000
32	00100000
64	01000000
128	10000000

Table 4.1

Using these constituent parts, we can make a cable of any integer length (in cm) less than 2.56 m with at most eight connections, with some examples shown in Table 4.2.

Required length (cm)	Binary representation	# connections needed
17	00010001	2
28	00011100	3
100	01100100	3
150	10010110	4
200	11001000	3

Table 4.2: Building a $\lambda/2$ cable from smaller, constituent parts using binary addition.

While the theoretical maximum number of connections to form a $\lambda/2$ cable of length l goes like $\log_2(l)$, in practice we use far fewer components than the brute force method. Since a deuteron target in a 2.5 T field requires a cable longer than 7 m, the cables built in Table 4.1 go up to 512 cm.

4.3.4 Finished System Operation

Finally, the Q-Curve was tuned on both the diode detector and phase sensitive signal outputs at UVa and Duke. While the curves respond to an oscillating crystal, the noise on the Duke trial is substantially higher than it was at UVa. In Figure 4.23, the system was on clean power, so it is surmised the noise is getting through improper shielding in the setup, possible through gaps left in the Yale Card housing.

4.4 Support Systems

4.4.1 LN₂ Traps

The LN₂ traps serve as the last filter for the circulated helium gas on its way to the refrigerator. In theory, the ³He circulation loop is closed and does not need inline filters, but in practice the system becomes contaminated with either air that slowly seeps in through the vacuum seals or by exhaust coming from the mechanical backing pump. Additionally, the air

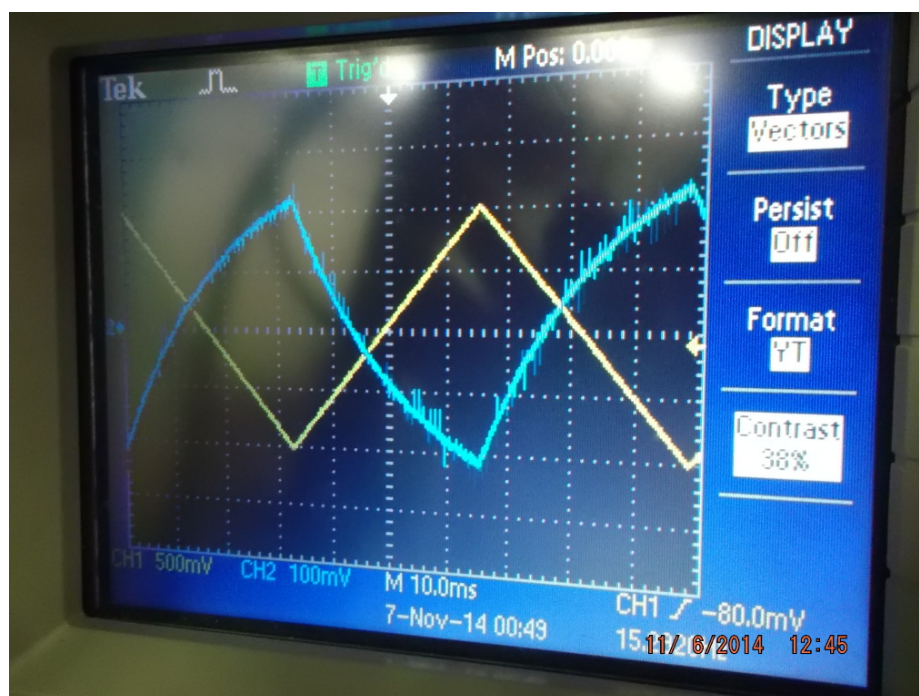


Figure 4.23: The Q-Curve at Duke, shown here in YT mode, shows noise getting into the signal in the form of spikes on the blue curve.

gathered in the system from the refrigerator assembly is only evacuated for about 10 minutes and the remaining pressure in the $\mathcal{O}(1\text{ m}^3)$ will be cleaned by the nitrogen trap[Nii76]. Other than neon, hydrogen and helium, nitrogen has the lowest boiling point of any liquid and is by far the cheapest and safest cryogenic liquid to use for trapping and condensing contaminants before they reach the refrigerator.

UVa's Polarized Target Group received a LN_2 trap with the CERN dilution refrigerator pump system they inherited, which was used for the UVa Hifrost cooldowns. However, it was found in late 2012 this trap had a large vacuum leak on its welded flex bellows, and was no longer useful for operation.

Without accompanying drawings, we chose to split open this broken trap and build another in its image. The vacuum line was a tube-in-tube type, with a circuitous route for the gas to flow built into the outer shell of the can down to the bottom face, where there was

a nested set of filters: course steel mesh, a perforated steel disc, and a sintered copper disc. Finally, the central volume was filled with activated carbon and exited through the inner volume of the tube-in-tube vacuum line. Measurements and details are shown in Figure 4.24.

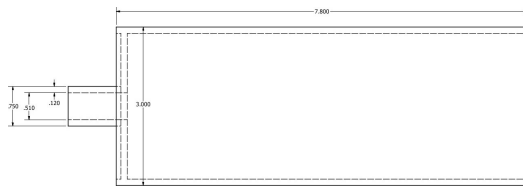
The frozen spin target, Frost, designed and operated at Jefferson National Lab, has a very similar ^3He circulation loop compared to Hifrost. They employed two LN_2 traps plumbed in parallel with only one being operational at a time, so that if one were to require regeneration (see below) the circulation would not have to stop[Kei12]. The Hifrost group decided to investigate reproducing this functionality⁴ and designed a prototype dual trap manifold, a modular vacuum subsystem that replaces the existing individual trap.

Operation of the dual trap manifold is described by the schematic and accompanying caption shown in Figure 4.25. The left and right lines in the image are the copper gasket connectors that hook up to a single trap in the system, making the dual trap subsystem a module installation in theory. In practice, the limited space on the ^3He gas rack and the constraint of only using one LN_2 dewar makes the installation on the Duke system more technically challenging.

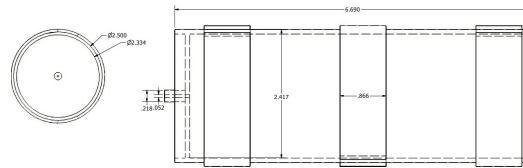
Shortly after being designed, the UVa Polarized Target Group commissioned a compact prototype of the dual trap manifold to be built for use in their pumping system as a joint graduate-undergraduate summer project, as pictured in Figure 4.26. As detailed in a group technical document, an optimal combination of welded vacuum components and o-ring seals limited the risk for a leak but still allowed the valves to be reused for future projects[Gil13].

As the purpose of the LN_2 traps is to become contaminated (to *trap* pollutants in the ^3He gas system), it is necessary to clean them, a process called regeneration. There are three scenarios when the traps are cleaned: before a cooldown (preparational regeneration), during a run (operational regeneration), and after a run (post-cooldown regeneration).

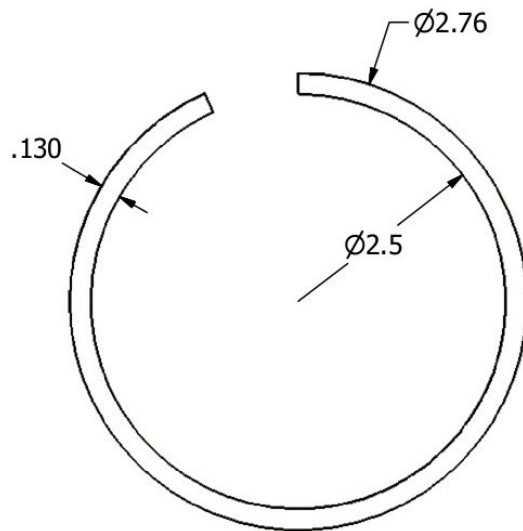
⁴This is an interesting point, since Frost was designed with some of Hifrost's features in mind.



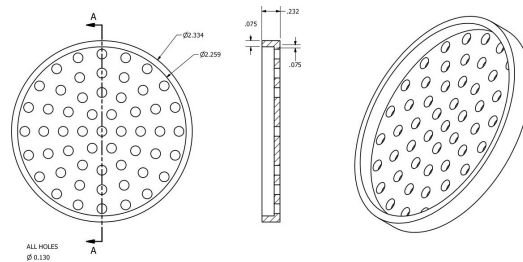
(a) The dimensions of the outer surfaces of the trap.



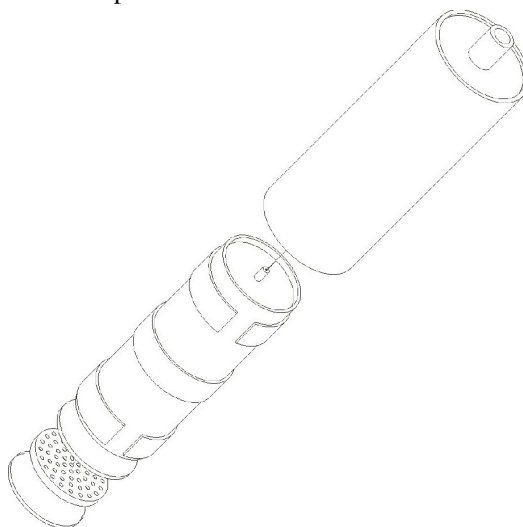
(b) A cross section of the concentric shells are shown on the left, and the profile cutout of the "gas maze" is shown on the right.



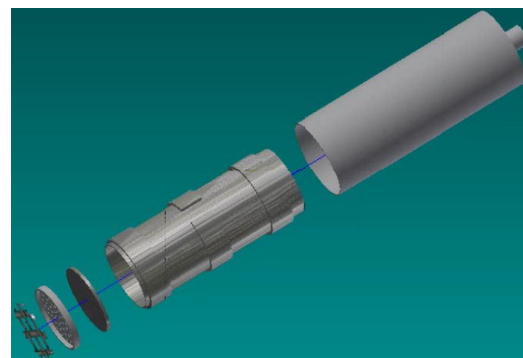
(c) The open-ring spacers that force the incoming gas around a winding path before reaching the bottom cap.



(d) The perforated steel disc that secures the mesh.



(e) Drawing showing the parts assembled.



(f) 3D model of the parts being assembled..

Figure 4.24: Hifrost LN₂ trap design and drawings.

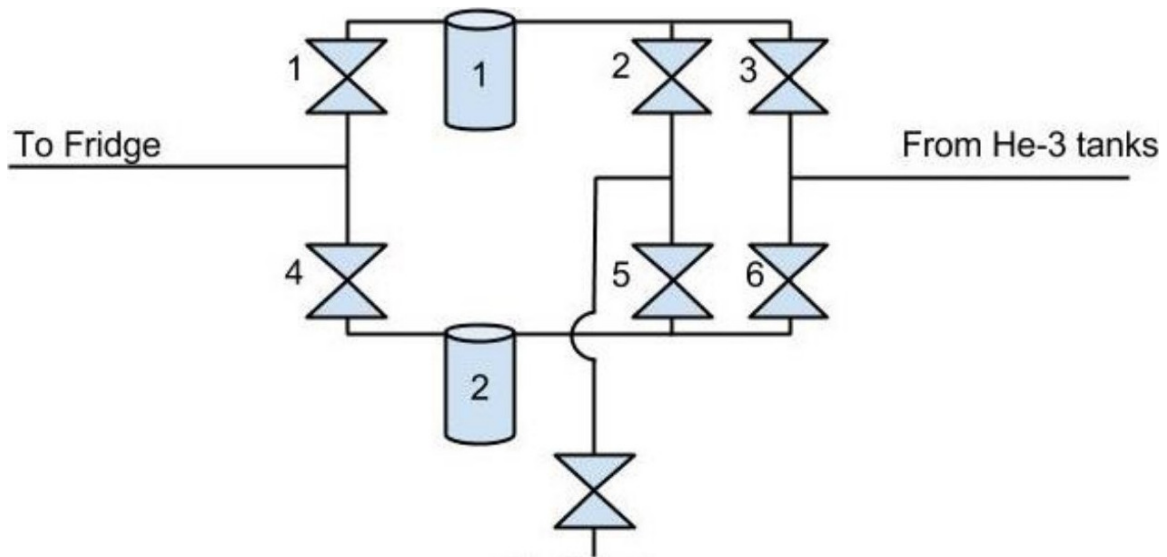
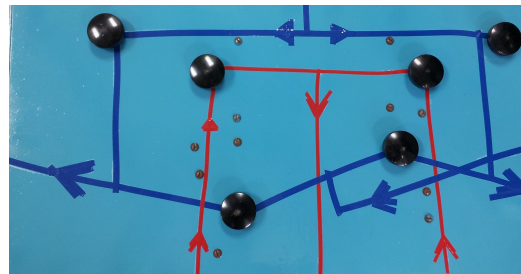


Figure 4.25: Schematic for the dual trap manifold. The unmarked valve at the bottom leads to the evacuation pump, and its implementation depends on whether the system already has a valve there. ^3He gas comes from the tanks (or circulation pump system) on the right, and goes through Valve 3, Trap 1, and Valve 1 before heading to the refrigerator. If Trap 1 should need to be regenerated during a run, the gas is instead directed through Valve 6, Trap 2 and Valve 4 while the regeneration pump evacuates Trap 1 through V2.



(a) Inside view showing the welded and KF-connected plumbing.



(b) View of the front panel. Blue tape designates the circulation loop and red tape indicates the evacuation pump line.

Figure 4.26: The prototype of the dual trap manifold built at UVa[Gil13].

Preparational regeneration, also known as a “bake out”, is the most thorough cleaning the trap undergoes since it is unknown how long the trap has been exposed to air (and atmospheric moisture) and there is more time to operate in a controlled manner. At room temperature, the trap is first wrapped with aluminum foil, which has an order of magnitude greater thermal conductivity than stainless steel, and outfitted with two thermocouple thermometers with accompanying readouts to monitor the trap temperature during the regeneration. A heater cuff is secured around the trap and warmed up before beginning evacuation with the regeneration pump. A photo of a trap being regenerated for preparation for a cooldown is shown in Figure 4.27. After a few minutes, the temperature is gradually ramped up until the thermocouples read about 140 °C. The trap is left to bake out for hours to days, depending on the estimated degree of trap contamination and safety considerations for that particular setup.



Figure 4.27: A LN₂ trap undergoing operational regeneration.

Operational regeneration is required when the LN₂ trap becomes so contaminated that

^3He flow becomes inadequate to operate the dilution refrigerator. The degree to which a trap fills up is monitored by watching the pressure differential across it with two atmospheric-scale pressure gauges while gas flow is in a state of equilibrium. If a dual trap manifold is installed, ^3He flow is directed to the secondary trap while the first one is regenerated, as described by the caption in Figure 4.25. If only one trap is present, the trap can be cleaned without ending the cooldown if the following outlined steps are performed quickly enough[Kei13]:

1. Stop ^3He circulation and close any valve through which ^3He may be vented to atmosphere.
2. Turn on the evacuation pump and open it to the trap.
3. Remove the trap from the LN_2 dewar and heat it with a heat gun until the pressure reads approximately 1 mbar or less.
4. Place the trap back under LN_2 , close the valves to the evacuation pump and power it off.
5. When the trap is cold, slowly open the required valves to resume circulation.

Operational regenerations are significantly more risky with a single trap, so it is advised to always operate with a dual trap manifold.

The need for a post-cooldown regeneration stems from the safety concern of having an unknown amount of gas either condensed or liquified inside a restricted volume. As part of ending a cooldown, the circulation gas is captured in a vessel while the refrigerator warms up, and eventually the LN_2 level of the dewar that houses the trap will fall enough to warm the trapped contents. To prevent the risk of such expansion causing an explosion, the trap is valved off from the system once its pressure falls around 1 mbar and regenerated

with the evacuation pump. In the event that it is desired to know the amount of gas caught in the trap⁵, it may instead be opened to a large external vessel with a pressure gauge and emergency relief valve.

During post-cooldown regenerations, the trap may either be warmed with a heat gun, left in the dewar for the LN₂ to eventually fall, or simply taken out of the dewar and allowed to be warmed by the ambient room temperature.

4.4.2 ³He Recovery System

During a cooldown that uses the dilution refrigerator, the first step of condensing helium gas in the refrigerator is opening up the ³He storage tanks⁶ to the evacuated ³He circulation loop. The pressure differential that drives the gas from a tank can't pressurize the condenser line above the tank pressure, which is initially just under 1 atm. As the gas cools and eventually starts condensing, the condenser line and gas tank pressures drop together, which is suboptimal as the condenser line operates more efficiently at a high pressure. As long as the pressure differential between the tank and condenser line is the only force driving gas into circulation, there is no way to bring gas from a low pressure tank into the higher pressure condenser line.

When the ³He storage tanks are refilled at the end of a cooldown, the valves between the main mechanical ³He pump and the tanks are opened and those between the pump and LN₂ trap (and thus, the rest of the circulation loop) are closed, causing the extended volume between the pump and tanks to be at constant pressure, usually around 1 atm. This trapped gas, possibly containing valuable ³He, will likely be lost between cooldowns, as the system

⁵This is useful information when attempting to quantify the effect of small leaks from atmosphere into the vacuum system.

⁶The phrase *³He tanks* is a bit of a misnomer: of the three gas tanks, one stores nearly-pure ³He, one stores nearly-pure ⁴He, and one stores a mixture of the two in whatever ratio it was collected from the system. The tanks are called the ³He storage tanks because they are attached to the ³He gas panel.

is often being opened and closed for either diagnostic/maintenance purposes or just to verify the vacuum system is behaving as it should before the next cooldown.

These two partially related problems are addressed together with an installation called the ^3He recovery system, which consists of a hermetically sealed pump and an arrangement of valves to allow pumping in both directions between the ^3He storage tanks and the ^3He circulation loop. A schematic of the system is shown in Figure 4.28.

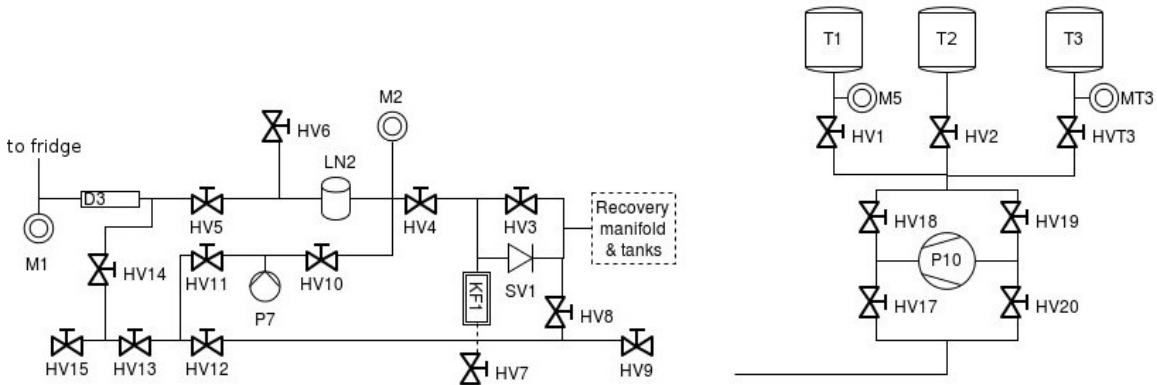


Figure 4.28: The ^3He recovery system is shown on the right. It hooks into the ^3He gas panel region marked by the dotted box; the rest of the gas system is shown for context. Before the recovery system was installed, HV3 was directly connected to the valves HV1, HV2 and HVT3.

When running, the pump extracts gas from the tanks to the condenser line when HV17/HV19 are open (and HV18/HV20 are closed), provided HV3 and the rest of the valves on the gas panel are properly set. When HV18/20 are open (and HV17/19 are closed), the pump collects gas from the panel and recovers it to an open tank.

The design for the ^3He recovery system was started in January 2014 and installation was finish in early July. The technical hurdles included identifying the pump requirements (pressures, flows, acceptable volumes, physical dimensions, leak rate, etc), commissioning and mounting the pump, providing the proper voltage to power it, purchasing vacuum components, working with the welder to assemble the manifold, vibrationally isolating the gas panel from the pump, modifying the steel gas panel structure to accommodate the new

valve panel, and leak/pressure checking the system before running it. The entire project is not covered in detail here, but a flowchart outlining the process of running diagnostics on various candidate pumps is presented in Figure 4.29 to show a sample of the work done. Further details can be found in the Hifrost log book.

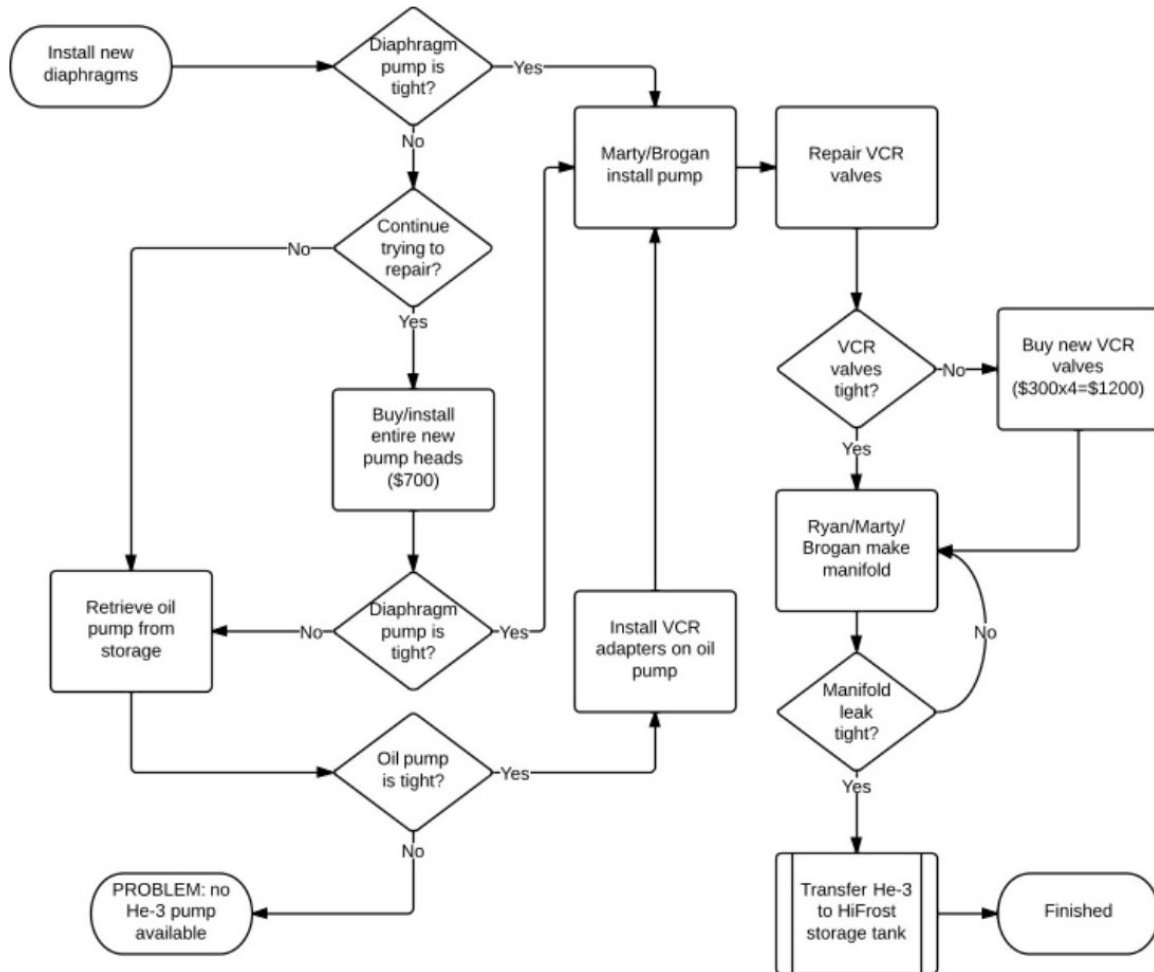


Figure 4.29: Flowchart to illustrate the project management and decision making process that went into the ^3He recovery manifold project. At this stage, we were deciding whether we could utilize an old diaphragm pump or an older oil sealed pump.

The ^3He recovery system ended up working very well for both of its intended purposes. A description of the system performance is included in Section 4.4.4 on mash cleaning.

4.4.3 ^3He Circulation Loop

The ^3He circulation loop is a subvolume of the ^3He gas system through which mixture circulates during normal dilution operation. Schematically, it is comprised of components marked in red in Figure 4.30.

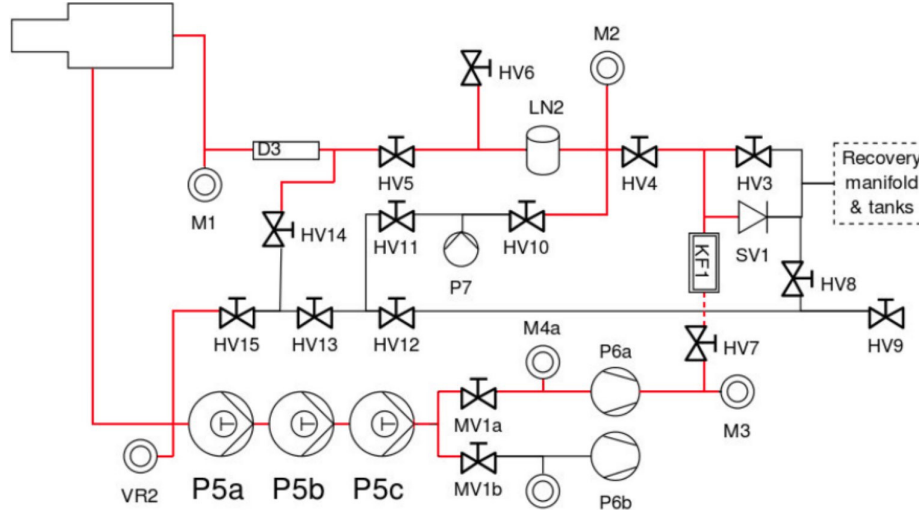


Figure 4.30: The ^3He circulation loop, marked by red lines above, consists of the following components starting with the refrigerator and going counterclockwise around the figure: refrigerator still line, ^3He Roots pumps, ^3He mechanical backing pump, the 300 K trap KF1, the LN_2 trap (or dual trap manifold if installed; see Section 4.4.1), ^3He gas flow meter D3, condenser line of the refrigerator and all internal refrigerator ^3He volumes.

The ^3He circulation loop requires special attention during cooldown preparation work because of the many potential places for a system leak and the repercussions of a pressure or vacuum leak. In the high pressure side of the system, the volume that spans the outlet of mechanical pump (P6a in Figure 4.30) all the way counterclockwise up to and including the refrigerator, a leak during steady state operation will mean constant loss of ^3He gas, which will probably go undetected because the pressure dropping from above an atmosphere will be indistinguishable from condensation in the refrigerator. For the rest of the system, called the low pressure side of the ^3He circulation loop, a leak will mean an undetectable, slow and steady supply of atmospheric air will enter the system and make it as far as the LN_2

trap, clogging it and requiring an operational trap regeneration. Even worse, if it gets in fast enough, enough air might make it past the LN_2 trap and partially or completely block the condenser line as it liquifies and freezes in the refrigerator.

Several layers of protocol are in place to mitigate the risk of the disastrous consequences of a leaking ^3He circulation loop. First, any vacuum components installed are leak checked independently first, and then again once connected to the system. Second, extra steps are taken to prevent vacuum seal breakdown: metal sealed connectors like VCR and Swagelok are used where possible, and if KF must be used on the high pressure system, usage of an overpressure KF o-ring retaining assembly is preferred. Finally, the ^3He circulation loop is only vented with helium gas or dry nitrogen (instead of air, which may be used on other vacuum subsystems) to prevent a leak manifest at low pressures from masquerading as water vapor outgassing. Any vacuum component or connection in question of leaking is checked with a leak detector.

Finally, the ultimate method for determining whether the ^3He circulation loop's vacuum seal is secured is the vacuum rise test (VRT), which is the process of pulling a known volume down to low pressure⁷, isolating it from the pump and monitoring the volume's pressure with respect to time. Also known as a “vacuum decay” test or a “pressure rise” test, the VRT characterizes the integrity of the entire circulation loop, taking into account leaks and cleanliness of vacuum surfaces, and is a “proof-test” that verifies whether the loop will perform as desired when the dilution refrigerator is operated[Ber02].

While performing a vacuum rise test on the entire ^3He circulation loop (Figure 4.30) can show the rate at which the system loses vacuum (Figure 4.31), it is not able to provide additional information regarding where the leak is, if any exists. Tricks are available to determine if the leak rate is dependent on the pressure regime, which might give clues that

⁷The ^3He circulation loop is brought down to about 10^{-3} mbar, while the IVC and OVC are brought down below $\mathcal{O}(10^{-5})$ mbar. Other, less critical systems may not be brought down so low.

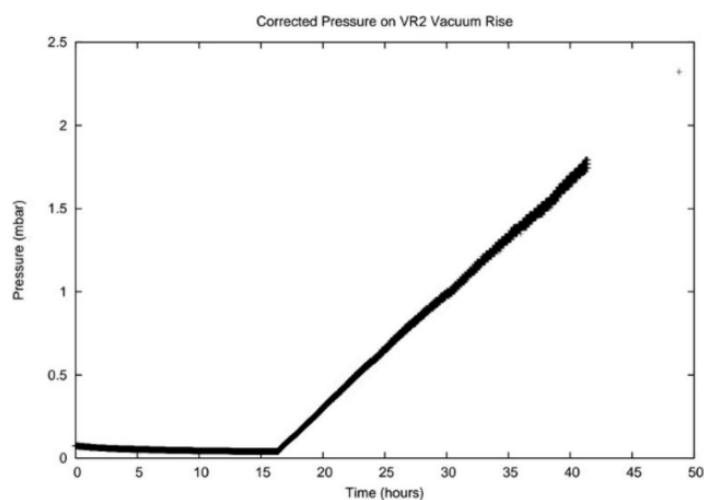


Figure 4.31: Example VRT result showing the ^3He circulation loop pressure vs. time as part of cooldown preparation.

outgassing is more likely the cause of the vacuum rise than a leak to atmosphere (example graph shown in Figure 4.32), but the only way to localize a leak with a VRT is to shrink the volume being monitored.

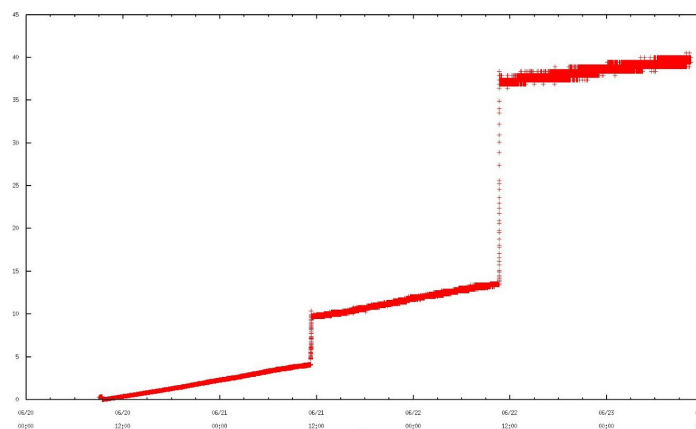


Figure 4.32: The pressure of the ^3He circulation loop, in mbar, is recorded with time for different pressure regimes. Every 12 hours, the pressure is discretely increased to determine if the rate of vacuum change depends on the absolute pressure.

The best way to do this in the ^3He circulation loop is to partition the loop into logical subvolumes and perform a VRT on each section individually. Figure 4.33 shows one way we split the system into four subsystems using valves, blanks and ancillary pressure gauges.

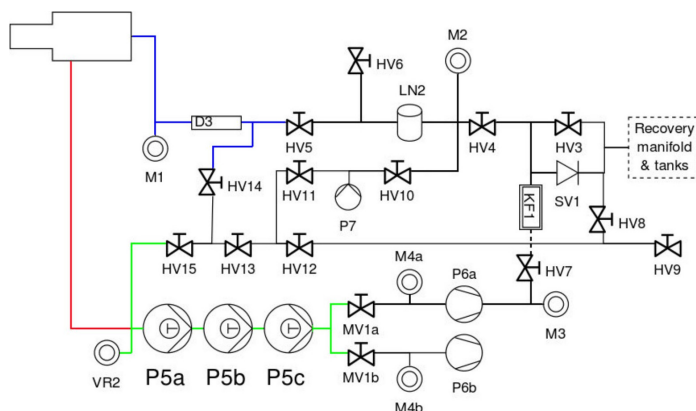


Figure 4.33: The ^3He circulation loop is partitioned into four volumes: the condenser line (blue), the still line (red), the pump stack (green), and the gas panel (black).

By comparing the VRT results for each section in Figure 4.33, we were able to determine which section the leak was coming from (in this case the culprit was the WKP4000 Roots pump, see Section 4.4.6 for details).

Finding problems with the ^3He circulation loop VRT became so common, we eventually installed a gate valve at the inlet of the ^3He Roots stack to isolate the still line from the pumps more systematically and without requiring a technical team to replace vacuum connections with vacuum blanks.

4.4.4 Mash Cleaning

Mash⁸ cleaning is another safety precaution to prevent air from contaminating the LN_2 traps or causing an ice plug in the condenser line of the refrigerator. Ideally, the mash would be transferred to a large tank with a top and bottom port, as shown in Figure 4.34. A hermetically sealed pump, such as an Alcatel 2063H, pumps the gas in a small circuit, through a LN_2 trap and back into the tank for a period of a few hours. Afterwards, the system would

⁸The dilution refrigerator relies on a *still* to preferentially boil off ^3He for circulation. The more common use of the word refers to the modern distillation apparatus, first widely used by the alcohol industry to isolate drinking alcohol from the byproducts of a mixture called *mash*, a mixture of malted barley and water. By humorous comparison in the field of cryogenics[Kei12][Uhl15][GHPM15], the term *mash* refers to $^3\text{He}/^4\text{He}$ mixture used by the dilution refrigerator, a tradition carried on by Hifrost.

be hooked back up to the ^3He gas panel and the recovery pump would store all the mash into the ^3He tank it was initially drawn from.

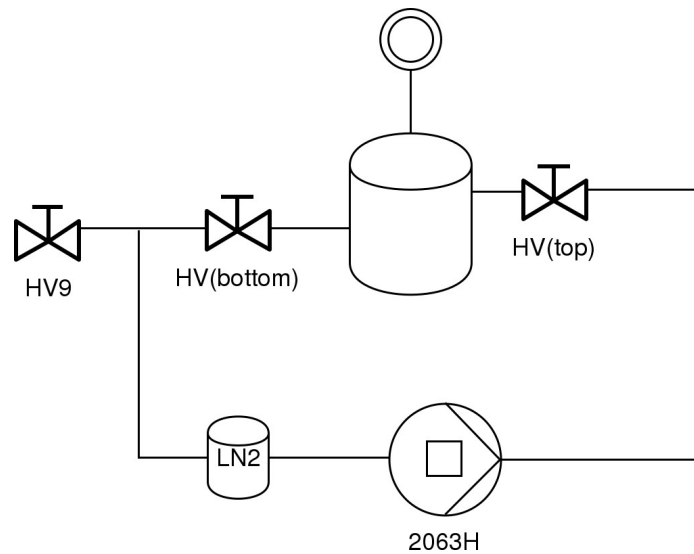


Figure 4.34: Schematic for the ideal mash cleaning setup. The tank would be large enough to store all the mash without the pressure gauge reading above atmosphere.

Unfortunately, despite attempts to gather the resources at Duke to make a setup like the one shown in Figure 4.34 materialize, no such idealized cleaning system was ever built. Instead, we used an improvised system schematically shown in Figure 4.35. Instead of continuously circulating through a LN_2 trap, we utilize the recovery pump to pull the gas from a storage tank and send it to an external tank via the trap. When the storage tank is empty, the direction of the recovery pump system is reversed and gas is pulled out of the external tank, back through the trap and into storage. This process is repeated until two consecutive passes show the same pressure on the storage tank, indicating no contaminants are present in the gas.

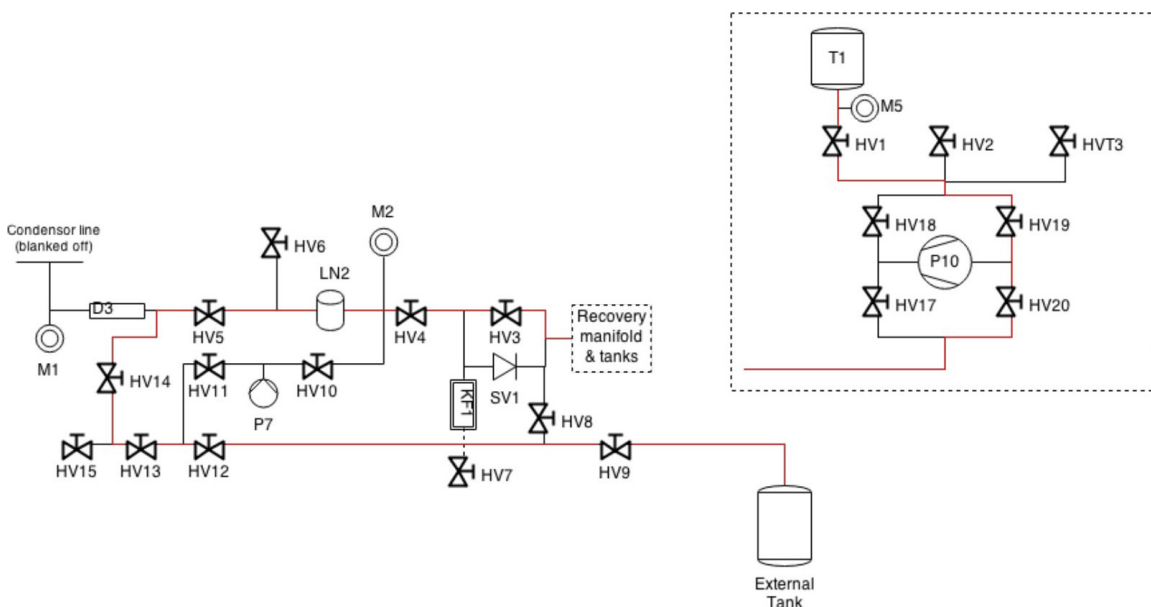


Figure 4.35: The mash cleaning mechanism we actually used involved utilizing the recovery pump to transfer the mash between a storage tank (T1 in this case) and an external tank, via the LN₂ trap and external port HV9. The red lines indicate the gas path.

4.4.5 RGA Measurements

A residual gas analyzer (RGA) is a small mass spectrometer used to identify the species of gas in a sample and provide the relative ratio by volume of each gas present. In the RGA, a sample of the gas is first ionized at low pressure before the trajectory of the resulting beam is accelerated and deflected by an electric and magnetic field, respectively[KJL]. Since ions of different mass will follow different paths, the RGA can bin and count the ions based on their mass and provide a histogram of how many counts it collected for each nuclear mass. The output is given in terms of ion current, but since we are generally only concerned with the ratio of peaks in the histogram we disregard the units.

The information provided by the RGA allowed us to perform our first dilution-centric cooldown at Duke with an idea for how much helium we had. In 2016 at UVa, a similar measurement was made on the uncertain ratio of $^3\text{He}/^4\text{He}$ in the tanks on that system, showing the mixture to be circulated consisted of 10% ^3He .

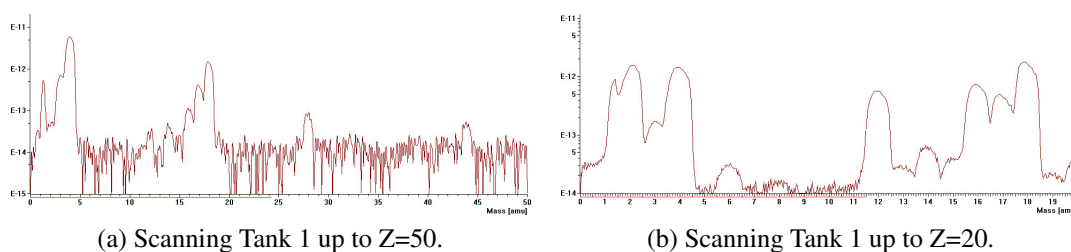


Figure 4.36: The RGA used on the tanks that came from Germany showed they had nontrivial amounts of both ^4He and ^3He . The background peaks, mostly water, carbon dioxide and nitrogen, were compared with a control measurement taken with the RGA before the helium tanks were hooked up.

4.4.6 WKP4000 Roots and ^3He Pump Stack

The commissioning of the ^4He pumps was straightforward and will not be discussed in-depth. To briefly summarize, the Roots pumps were previously unused and the Duke team built a pump stand and installed the electronics for the pumps, interlocks and gauges. The pumps pulled their nominal vacuum and did not malfunction unless overloaded (see Section 6.2.3).

The ^3He pump stack and its crown, the WKP4000 Roots pump, have a very different history. The pumps were used in several experiments, ending around 2006, before being delivered to Duke and stored outdoors, exposed to the elements, from 2010-2011. Once brought inside, a coupling between the WKP4000 motor and main oil reservoir was found to be broken and the protective cage for the motor fan was damaged[Seo12b]. The backing mechanical pump was replaced entirely and the vacuum lines, bellows and flanges were leak checked before the pump stack was deemed fit for experimental runs.

After finding a large air leak into the ^3He circulation loop during the July 2014 cooldown, a VRT (see Section 4.4.3) and subsequent leak checks showed the WKP4000 was leaking to atmosphere. With the oil drained and the WKP4000 inlet and the mechanical backing pump outlet sealed, the system pressure rose at a rate of 1-3 mbar/day. Conservative estimates for the pump volume allow this to be a large percentage of the air we collected during the

cooldown.

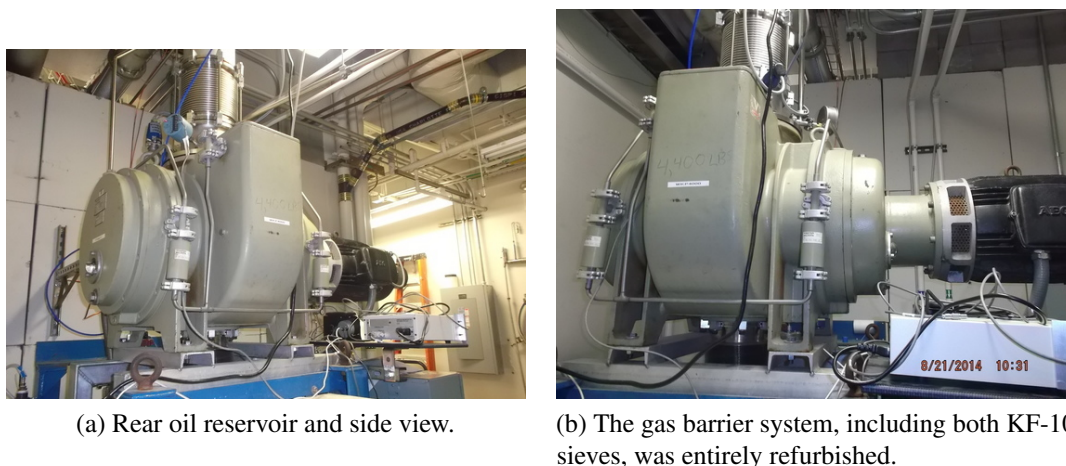


Figure 4.37: The WKP4000 Roots pump.

We attempted to locate the malfunctioning seal on the WKP4000 with a leak detector which pumped through a LN_2 trap into the system⁹, but found too many leaks to quantitatively rank them, even by orders of magnitude. Eventually, the entire gas barrier system, used to equilibrate the pressure between the Roots gear boxes and the main pumping volume (Figure 4.37), was refurbished by replacing all KF o-rings, machining all aluminum KF sealing surfaces and cleaning out the gas lines. The o-rings on the sieves were replaced before replacing the VacSorb molecular sieve charge. After maintenance, all gas barrier system parts were found to be leak tight to 5×10^{-9} mbar L / s.

After refurbishing the WKP4000, a vacuum rise test on the pump stack and still line was 0.46 mbar / day, less than a third of the previous rate of rise test on a similar volume.

The 2063H mechanical backing pumps on the ^3He pump stack were also found to leak in various places. However, due to inconsistencies in the history of logging the pumps' performance, it was impossible to determine if there was a root cause or if all the pumps failed for different reasons. Eventually, we just cycled them until the pump with the best

⁹The oil mist from the Roots pump gear box would ordinarily contaminate a leak detector.



Figure 4.38: The WKP4000 oil plug (of which there are four) shown here was leaking enough to see bubbles rise through the oil in the sight glass. Two other oil seals were found to have similar leaks and all were replaced.

VRT was used in the circulation loop and the others were utilized as secondary evacuation pumps.

4.4.7 Data Acquisition

During the first UVa Hifrost cooldowns, beginning in August 2012, all slow control data was taken by hand as frequently as was allowable. This led to hand-written tables, like the one in Figure 4.39a, in the log book with temperatures, pressures and flows taken as frequently as every ten minutes and as infrequently as every hour.

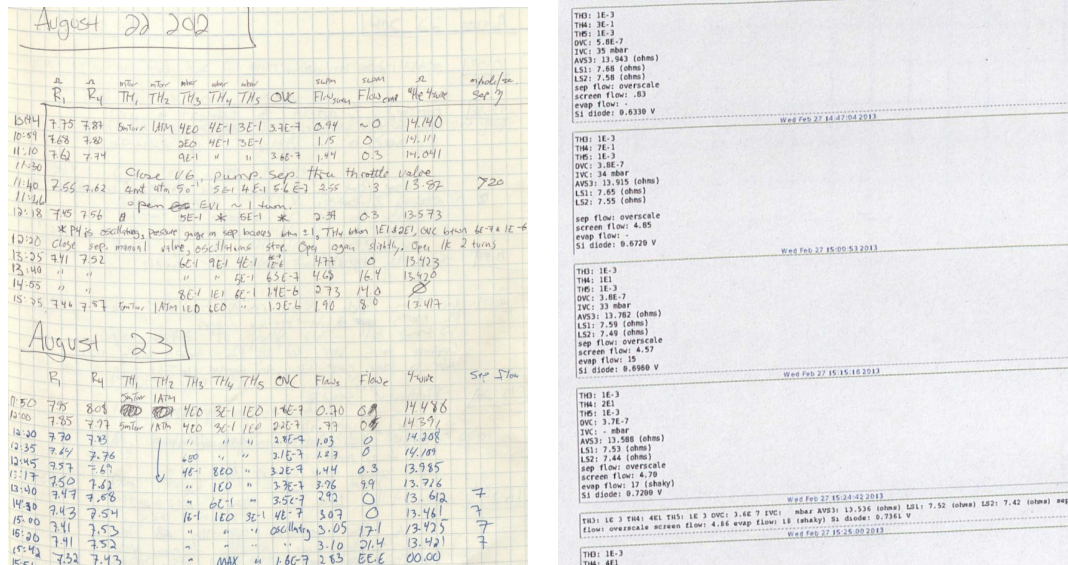


Figure 4.39: Data acquisition systems during early Hifrost work.

In early 2013, the electronic logging software ELOG (Figure 4.39b) was installed for two purposes: typing cooldown notes with automatic timestamping and the systematic completion of a slow control log with a pre-filled HTML form and partial autocompletion functionality. While this improved the readability of the logs considerably, it did not address the requirement that the researcher must be distracted from the target operation to make

rounds of slow control measurements throughout the hours of cooling. Additionally, there was considerable push back from some researchers in the group at the concept of having an electronic log book.

In November 2013, a USB-connected, 4 channel I/O, 1.2 kS/s¹⁰ DAQ was purchased from Measurement Computing Corporation to begin investigating whether the Hifrost system could integrate automatic slow control data acquisition given our limited processing power, network throughput and open source operating system, Linux.

In January 2014, correspondence with Professor Warren Jasper of North Carolina State University led to the first flow meter voltages (see Section 4.1.4) sent to the DAQ being read to hard drive and we saw promising results CPU load, hard drive space consumption and network lag diagnostics. In February, a second DAQ with 8 channel I/O and 250 kS/s was purchased for use in the Gamma Vault. By March, both DAQs were readings simultaneously and storing measurements in a shared database, and in June we had all analog signals from Hifrost slow control instruments measured and recorded.

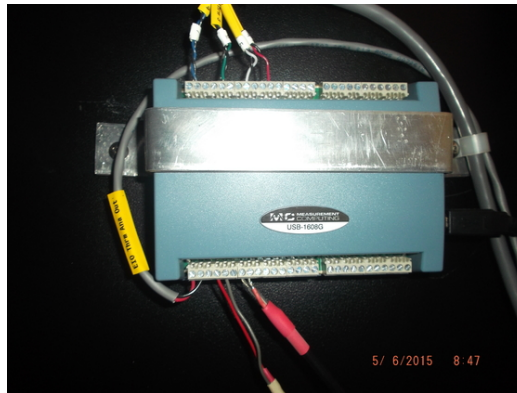


Figure 4.40: The USB-connected MCCDAQ 1608G ADC in the Gamma Vault reading voltages from various instruments.

In July, we integrated serial communications via the RS-232 interfaces of the pressure gauge and thermometer readouts into the data stream over the network. This not only

¹⁰Kilo-sample per second, a standard unit of measure for DAQ time resolution.

completed the list of instruments we wanted automatically read, but freed up some analog channels on the USB DAQs since we could read some modules over both RS-232 and analog signal¹¹.

Analog DAQ Software

All analog DAQ software is hosted on the same computer that the USB module plugs into and must be run locally. In the past, we have used both MCCDAQ's 1608G and 1208LS ADC modules, but we almost exclusively use the former due to its faster time resolution and greater number of analog channels. To simplify the remainder of this section, we will consider only the 1608G.

The program that reads our instrumentation is a derivative of the example program distributed by MCCDAQ¹², and must be compiled after the `libusb` and `libhid` packages are compiled and installed and the `udev` rules are properly set. Detailed installation instructions are found in the instruction file `GET-UP-AND-RUNNING`, available with the data acquisition source code.

Once running, the DAQ source code is in the C source file `mysql-usb1608G.c`, which builds the executable file of the same name. The reason for the MySQL name is explained in Section 4.4.7.

The C code is straightforward: a non-blocking `do-while` loop queries the 1608G on an infinite loop with a hard-coded sleep timer to space the readings in 1 second intervals. Two arrays, `deviceMap` and `channel_activated`, identify which instrument is hooked up to each channel and signal a `for` loop to query them. This is required since querying all channels would waste both system resources and make the data table unnecessarily large.

¹¹It is almost always preferred to read measurements via serial ports instead of analog channels for several reasons: the number of analog channels is limited by the (expensive) DAQ modules, analog cables need to be shielded, the microprocessor in the readout that controls the RS-232 communications often provides more information than just the measurement (device status, error codes, off-scale signals).

¹²A package downloadable as `MCCLIBHID.1.54.tgz`.

Figure 4.41 shows how we implement both of these arrays.

```
//associate channel to device
const char *deviceMap[8];
deviceMap[0]="b17separatorFlow";
deviceMap[1]="b17evaporatorFlow";
deviceMap[2]="b17shieldFlow";
deviceMap[3]="hfResistance";
deviceMap[4]="dev4";
deviceMap[5]="dev5";
deviceMap[6]="dev6";
deviceMap[7]="dev7";

//activate channels
channel_activated[0]=1;
channel_activated[1]=0;
channel_activated[2]=1;
channel_activated[3]=1;
channel_activated[4]=0;
channel_activated[5]=0;
channel_activated[6]=0;
channel_activated[7]=0;
```

Figure 4.41: Of the eight channels in this example code, only four are identified as lab instruments and only three of them are activated to be queried.

While the DAQ is limited to measuring voltages, we often want to record more meaningful units (e.g., Kelvin, mbar, etc). The relationship between most signals and their represented measurement is linear, so two data arrays, m and b ¹³, set the mapping from volts to other units. In the data stream, these two values are called the `raw` and `calculated` measured values, respectively.

For usability, the loop can be terminated with any character entered from the keyboard, although the standard output prompts for `x`. Once in the loop, activated channels are queried for their voltage reading, then have their device name, raw measurement and calculated measurement submitted to a database. See sample code of the loop in Figure 4.43.

¹³As in, $y = mx + b$.

```
float m[8]={
    5.504175466, //channel 0, b17 separator flow
    10.24966922, //channel 1, b17 evaporator flow
    13.94394392, //channel 2, b17 shield flow
    1000,        //channel 3, hfResistance (V = IR, I=1mA)
    1,           //channel 4
    1,           //channel 6
    1,           //channel 5
    1            //channel 7
};

float b[8]={
    0.9571403884, //channel 0, b17 separator flow
    1.473626518,  //channel 1, b17 evaporator flow
    2.992556781,  //channel 2, b17 shield flow
    0,            //channel 3, hfResistance (V = IR, I=1mA)
    0,            //channel 4
    0,            //channel 6
    0,            //channel 5
    0            //channel 7
};
```

Figure 4.42: The m (slope) and b (y-intercept) values are often empirically found by manually comparing the analog output of a sensor to the reading on the front panel of its accompanying readout. We comment the instrument next to its mapping parameters for readability in the source code.

```
do {
    for(i=0;i<8;++i) {

        //skip this channel if not activated
        if(channel_activated[i]==0) continue;

        device = deviceMap[i];

        //get values for database
        raw_meas=volts_USB1608G(i);
        calc_meas=m[i]*raw_meas+b[i];

        //add to db
        if (MYSQL_CONNECTION)
            writeData(device, raw_meas, calc_meas);
    }

    usleep(500000);

}while(!isalpha(getchar()));
```

Figure 4.43: Sampled C code of the do-while loop, which is exited by user input with `getchar()`. Activated channels have their terminal voltages queried and the corresponding measurement calculated before being remotely stored via MySQL connection.

Serial DAQ Software

While serial information is technically any linear sequence of data that is transmitted one bit at a time, the term is commonly used in computer networking to refer to serial communications via RS-232 port, a convention which we adopt.

The serial DAQ system makes use of the microprocessors embedded in our slow control readout modules that relay information digitally instead of through analog voltages. We connect them to computers in the laboratory with special RS-232 cables, called null modem cables, which correctly map the receiving and transmitting pins at each port to the other. In practice, we adapt the RS-232 to USB since there are many more USB ports than RS-232 ports on our laboratory computers. Since we rarely want to query our slow controls faster than 1 Hz, we do not need to worry about the limitations of serial communication. The incorporation of serial acquisition to the Hifrost system is a great improvement over the ADCs because we can send all measurements of one readout to the computer with a single cable.

We control our serial communications with the Python module `pySerial`. Figure 4.44 shows a sample configuration for setting up a temperature readout.

```
ser = serial.Serial('/dev/ttyUSB0',  
                    9600,  
                    parity=serial.PARITY_ODD,  
                    rtscts=False,  
                    bytesize=serial.SEVENBITS,  
                    stopbits=serial.STOPBITS_ONE,  
                    timeout=0,  
                    xonxoff=True,  
                    dsrdtr=False)
```

Figure 4.44: Example code setting up `pySerial` to read the Lakeshore 218s temperature controller readout via serial connection.

Each instrument module has its own communication protocol which can be found in its

accompanying manual or on the manufacturer’s website. The principle is the same as the analog query: enter a loop, read the instrument measurement from the serial port, calculate the true measurement value, store the data and exit on user interaction.

```
try:
    while True:
        data=ser.read(ser.inWaiting())
        if len(data)>0:
            writeTemps(data)

        time.sleep(1)
        ser.write("KRDG? 0\r\n")

except KeyboardInterrupt:
    print "\nStopping data acquisition"
```

Figure 4.45: The Python loop that reads the Lakeshore 218s temperature controller readout.

One key difference between the Python loop shown in Figure 4.45 and the aforementioned C loop is the order of reading and writing. At the end of each loop, the instrument readout is queried (in this case with KRDG? for “Kelvin reading”) after the sleep timer returns. This is because serial communication devices aren’t perpetually transmitting information, but must first be prompted. Once the reading is transmitted, it is stored in a buffer that we copy to the `data` variable. Once that variable contains a finite length string, we send the measurements to a parsing/calculating function (`writeTemps()`), in the case of the Lakeshore 218s) which then stores the data permanently.

MySQL Database

A database program allows us to define characteristics of data, manipulate data optionally based on those characteristics, and utilize standard functions so we don’t have to build them from scratch. Since they are supported on a variety of platforms, we can use one set of syntax to request and control data regardless of whether we’re in a C, Python or PHP environment.

Most importantly, databases are optimized for efficiency, so for the most part we don't need to concern ourselves with the most efficient way of searching through hundreds of MB (or even tens of GB) at a time.

Hifrost uses the well known MySQL database for storing slow control data. MySQL was largely chosen because of the support many coding environments have for accessing it on a remote server, making the distributed nature of the Hifrost instrumentation less of an obstacle for the researcher.

A database is also very useful for selecting a subset of data matching a list of conditions. For example, Figure 4.46 shows some examples of common operations on a table of nearly 100 million records.

In Python, we use the `mysql.connector` module to send our pySerial information to a remote server. After instantiation, the MySQL connection is handled by a `cur` variable, called a cursor, and a `cnx` connection variable.

The `writeTemps()` function in Figure 4.47 is written nearly identically to the production code version. The temperatures are taken from the `data` variable and put into an array of temperatures called `temps`. A standard formatted string named `query` uses MySQL syntax to build a database entry, which is then populated with `temps`. The cursor executes the database call and `cnx` commits the operation before the function returns.

Discussion of web server calls to MySQL is discussed below, but the MySQL call from PHP (the web server programming language) is given in Figure 4.48 to show how similar it is to the Python code. This similarity exists for all languages connecting to the database and greatly simplifies accessing the data from a variety of environments.

Apache and Strip Charts

A strip chart is a live-updating graph with time on the horizontal axis and a measurement on the vertical axis. It is used to not only show what the current value of a measurement

```
mysql> SELECT COUNT(*) FROM slowcontrolreadings;
+-----+
| COUNT(*) |
+-----+
| 91128953 |
+-----+
1 row in set (37.31 sec)
```



```
mysql> SELECT device, created_at, measurement_reading FROM
slowcontrolreadings WHERE device = "mcSi" AND created_at
BETWEEN '2016-03-11 16:00:00' AND '2016-03-11 16:05:00';
+-----+-----+-----+
| device | created_at | measurement_reading |
+-----+-----+-----+
| mcSi | 2016-03-11 16:00:00 | 139.1800 |
| mcSi | 2016-03-11 16:00:01 | 139.1600 |
| ...283 rows omitted
| mcSi | 2016-03-11 16:04:59 | 134.8200 |
| mcSi | 2016-03-11 16:05:00 | 134.8000 |
+-----+-----+-----+
287 rows in set (0.02 sec)
```



```
mysql> SELECT device, created_at, MAX(measurement_reading) FROM
slowcontrolreadings WHERE device = "b17shieldFlow" AND
created_at BETWEEN '2016-03-11 10:00:00' AND '2016-03-11
20:00:00';
+-----+-----+-----+
| device | created_at | MAX(measurement_reading) |
+-----+-----+-----+
| b17shieldFlow | 2016-03-11 10:00:00 | 42.5418 |
+-----+-----+-----+
1 row in set (0.88 sec)
```

Figure 4.46: Examples of common MySQL functionality showing: top) how to count the number of data points in the database; middle) return all measurements of a specific instrument within a time frame; bottom) get the maximum measurement for a specific device within a time frame. Note the very quick, sub-second run times for the specified queries despite the nearly 100 million data points to search through.

```
def writeTemps(data, cur, cnx):
    temps = data.split(",")

    query = "INSERT INTO slowcontrolreadings (device,
        raw_reading, measurement_reading) VALUES (%s,%s,%s) "

    entries=
        [ ('sepSiHi', temps[0], temps[0]), ('sepSiLo', temps[1], temps[1])]

    cur.executemany(query, entries)
    cnx.commit()
```

Figure 4.47: Writing to the MySQL database from Python.

```
$begTimestamp=getBegTimestamp();
$endTimestamp=getEndTimestamp();

$prepQuery="SELECT measurement_reading, created_at FROM $table
    WHERE device=$dev AND (created_at BETWEEN $begTimestamp
    AND $endTimestamp) ORDER BY id DESC";

$STH=$this->DBH->prepare($prepQuery);

//execute statement
$STH->execute();
$result=$STH->fetchAll(PDO::FETCH_ASSOC);
```

Figure 4.48: Example code requesting data from MySQL using variable parameters in PHP, with some security code removed for readability. An SQL structure similar to that in the Python code (Figure 4.47) is stored in `$prepQuery`, which is executed by the database module and the resulting rows stored in `$result`.

is, but the recent history of what it was. Strip charts allow researchers to visually make distinctions regarding measurements quickly and in the middle of an experiment. They often have user interactivity features, such as a selection of which values should be present and how far back the chart history should reach.

Because a strip chart is a dynamic, user-interactive feature, it cannot be displayed as a standard file like a PNG image or PDF file. There do exist large frameworks, such as the distributed control system EPICS, that come with built-in data conversion, access security, modeling and simulation, data analysis and much more[Joh14]. While widely deployed solutions like these are popular for large experiments at national labs, the investment cost of installing and configuring one for Hifrost was too high, and it remained unclear if EPICS would run on the wide range of systems we were considering installing. Instead, we chose to tap a more familiar user interface: the ubiquitous web browser.

The basic control system is this: a client sets parameters in a web browser to populate a strip chart. The browser connects to an Apache web server that translates the user's parameters into an SQL request using PHP. Since there is overhead with every network connection, it is best for the Apache server be installed on the same computer as the MySQL database. The database returns the results of parameterized query to the web browser via Apache, which uses a Javascript toolkit called Flot to make the actual plot on the client's machine. On even underpowered and outdated systems, this whole process is fast enough to give a real-time scrolling strip chart that updates at 1 Hz.

Ignoring the HTML markup code and CSS aesthetics, we start from the web browser code and follow the data. Each URL supports a different strip chart and has an `index.html` file containing the code from Figure 4.50. The `reportparams` array contains the devices incoming to the database request as well as the time bounds for the data. The `callAjax()` function sends that array, along with other information, to a PHP script on the web server.

The script at `slowcontrols/getReport.php` instantiates a “SlowControlRe-

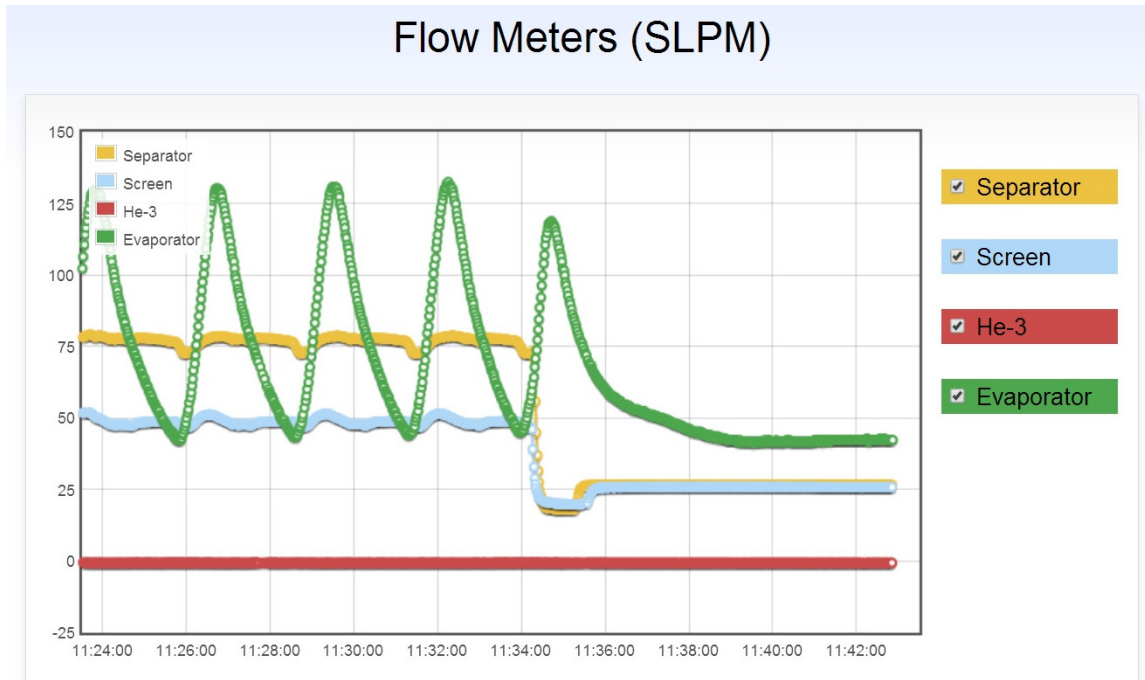


Figure 4.49: The first iteration of the Flot strip chart shows updated readings of all four flow meters in real time, a vast improvement from Figure 4.39a. In addition to freeing up the researcher from periodically recording readings by hand and providing much better time resolution, we are now able to see features in the slow control reading plots, such as the oscillations in the evaporator flow above, as well as relationships between readings like the out of phase features of the other flows.

```
//index.html
function getReportParams() {
    var reportparams={};
    reportparams['incomingDevs']=[];
    reportparams['incomingDevs'].push('b17separatorFlow');
    reportparams['incomingDevs'].push('b17shieldFlow');
    reportparams['incomingDevs'].push('b17evaporatorFlow');
    reportparams['nData']=$("#nData-value").val();

    //user defined timestamp
    reportparams['begTimestamp']=NMinAgo($("#nData-value").val());

    //"now" timestamp
    reportparams['endTimestamp']=moment().format("YYYY-MM-DD
        HH:mm:ss");

    return reportparams;
};

function callAjax(){
    $.ajax({
        url:"../slowcontrols/getReport.php",
        type:"POST",
        data:getReportParams(),
        dataType:"json",
        success: onReportReceived
    });
}
```

Figure 4.50: Each web page has a different list of instruments that it will list the latest measurements of, and is connected to by navigating to that particular URL.

porter” object, with implementations defined in `SlowControlReporter.php`. After sanitizing the input¹⁴, the script passes the user parameters to the reporter object and waits for a response (the requested data set), which it will send to the user.

Internally, `SlowControlReporter` uses PHP’s PDO package to populate an array of data points that meet the user’s criteria. Since MySQL and Javascript store timestamps in their own formats, a conversion process takes place before the time/measurement pairs are returned.

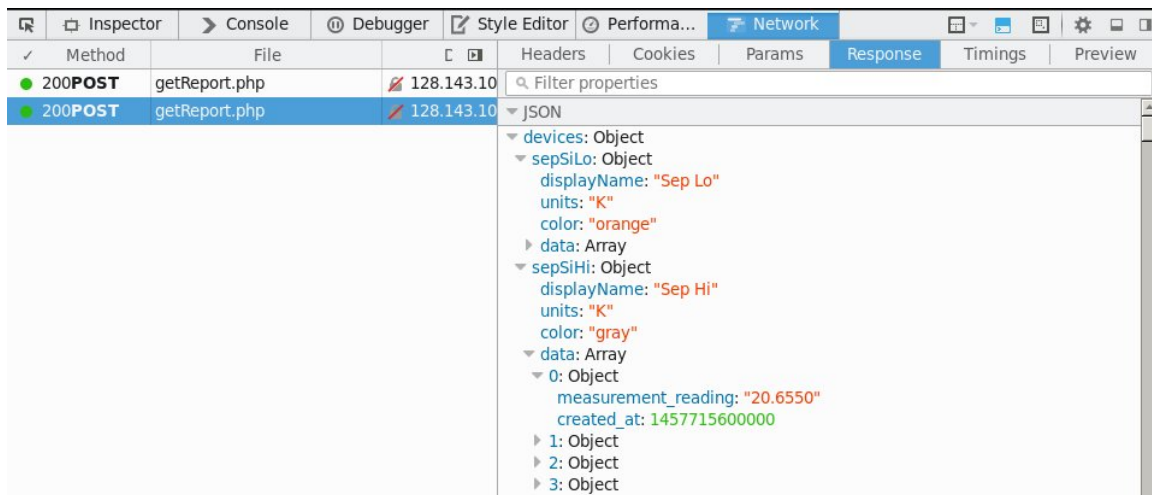


Figure 4.51: The response from `SlowControlReporter` as viewed in the web browser’s debugger. Thousands of data points can be returned in this way within tens of milliseconds, making the strip chart functionality possible.

Finally, what is returned from the server to the client is a JSON¹⁵ array called `devices`, as shown in Figure 4.51. Its children objects are the same devices listed at the top of Figure 4.50, which themselves have child properties such as `units` and a handle for the web browser to display in a user friendly fashion. The `data` child array of each instrument holds

¹⁴Despite being a restricted network and only being physically accessible by trusted lab members, the DAQ network is connected to the internet and many precautions must be taken as if this were a publicly accessible website. Such safety precautions are numerous and permeate the source code, so they will be mentioned no further except where they affect the program logic.

¹⁵Javascript Object Notation: an XML-like format all web browsers understand involving nested key-value pairs to form complex objects.

enumerated data pair objects with the actual time (`created_at`) and measurement data.

Data Request Form

While strip charts like the one shown in Figure 4.49 are very useful during an experiment, it is desirable to see the logs from past hours, days, or even in the months between cooldowns. The task of manually logging into the server and querying MySQL for data sets to be plotted with offline software (e.g., Gnuplot, Mathematica) became highly burdensome and required all lab members to learn SQL syntax and gain access to the server.



(a) The HTML form allowing the user to request past slow control data.

(b) A preview graph of the data returned by the API.

Figure 4.52: The Data Request Form is the front end for the MySQL database that users request data from past cooldowns with.

To alleviate this burden, a web-based API called the Data Request Form (shown in Figure 4.52) was made. When the form is loaded, an object called `SlowControlDataRequester` is instantiated, which finds the unique names of all instruments that have recordings in the database. The user selects which devices they want to view records for and enter the time

boundaries in MySQL's timestamp format. The data is sent to the browser and, after a pruning operation, a preview of it is generated with Flot. The complete data can only be accessed in the browser's developer view window (shown in Figure 4.51), but a data file output mode is in development.

One final point about the data acquisition with the data request form should be expanded upon. Since only one data point per pixel may be plotted and there is no upper bound to how much data is requested, the web browser first prunes the data, possibly destroying valuable information. As such, we refer to the plot in Figure 4.52b as a "Preview".

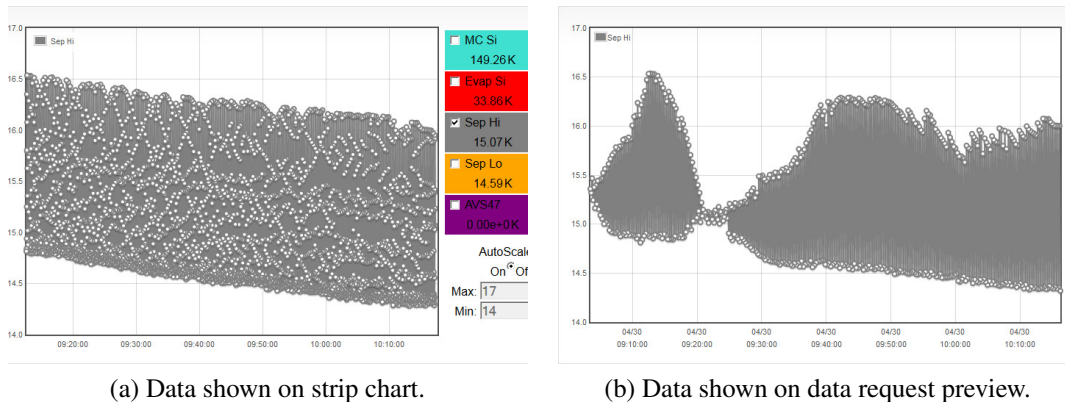


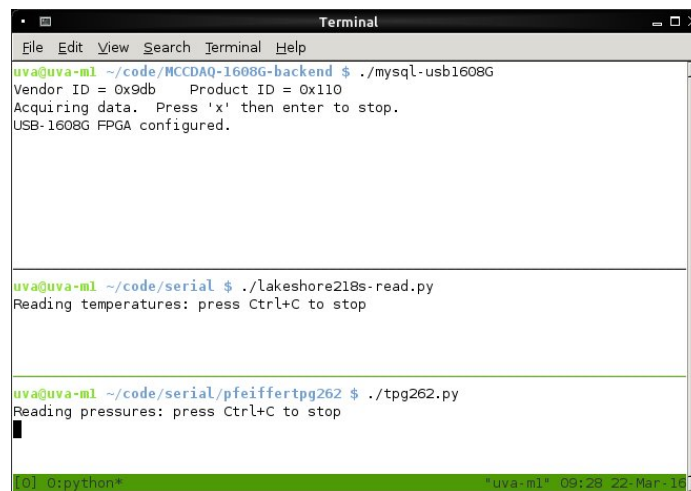
Figure 4.53: The same data shown on the strip chart and data request form previews, except that latter has a slightly larger time range. The pruning operation on the preview indiscriminately removes data points equally spaced along the horizontal axis until the plot width (in pixels) exceeds the number of points. As shown by comparing the two views, this falsely introduces a structure in the slow control graph that doesn't exist in the raw data.

This undesirable behavior could be corrected with a smarter pruning algorithm, however this exceeds the intended scope of the data request form. A common work around is to instead request a small enough subset of data such that there are more horizontal screen pixels than plotted points. If it is critical to manage all data points, the proper solution is to manually extract the data from the database either from the web browser or directly on the server for proper, user-controlled data manipulation.

Tmux

As the number of RS-232 and USB DAQ instruments grew, the accessibility of the machine that controls them declines. For example, at Duke there are three controller connections in the Gamma Vault and two at the pump station. The polarized target operator will be stationed in the counting room where the Apache and MySQL server is located. If the Python and C acquisition programs are started locally, they must be terminated locally, which might require a GV entry and loss of beam on target.

The solution is to use the program `tmux` installed on the counting room computer. `tmux` allows multiple shell sessions to be opened in a single window, and each networked computer can be navigated to with the usual `ssh` commands to initialize each data acquisition program. A secondary advantage is the `tmux` window may be detached from the shell window and exited while the child shells, and thus the data acquisition programs, persist. `tmux` may then be reattached from any other station that has network access to the counting room computer.



```
Terminal
File Edit View Search Terminal Help
uva@uva-ml ~/code/MCCDAQ-1608G-backend $ ./mysql-usb1608G
Vendor ID = 0x9db    Product ID = 0x110
Acquiring data. Press 'x' then enter to stop.
USB-1608G FPGA configured.

uva@uva-ml ~/code/serial $ ./lakeshore218s-read.py
Reading temperatures: press Ctrl+C to stop

uva@uva-ml ~/code/serial/pfeiffertpg262 $ ./tpg262.py
Reading pressures: press Ctrl+C to stop

[0] 0:python*          *uva-ml* 09:28 22-Mar-14
```

Figure 4.54: An example showing `tmux` running three slow control instrument controllers at once.

4.5 Liquid Helium Transfer

Liquid helium arrives in 100 L, 250 L or 500 L dewars from supply companies. Before helium is used, the liquid level of the supply dewar level must be measured to assure we received what we paid for (see Section 4.5.2) and, in the case of operation at the Gamma Vault, the helium transferred into our own dewar.

The cost of LHe drives the decisions of when and how we transfer it. The original plan for LHe distribution, shown in Figure 4.55, involved six transfer lines and four liquid vessels to operate the refrigerator and polarizing magnet.

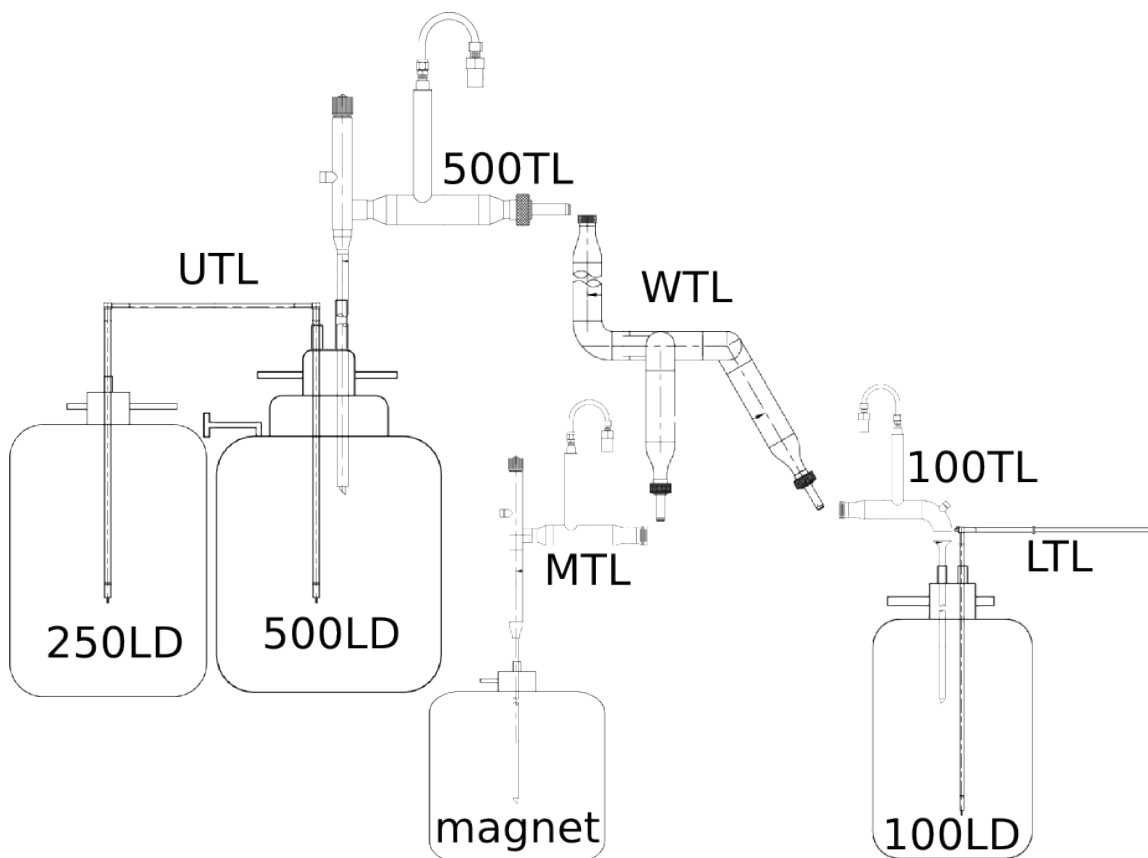


Figure 4.55: The original plan to transfer LHe from a 250 L delivery dewar to the Hifrost magnet and 100 L dewar.

The idea was to fill a 500 L dewar from 250-500 L delivery dewars with a “U”-shaped

transfer line (UTL) in an area outside of the Gamma Vault. The wall transfer line (WTL), a 12 foot long, rigid manifold permanently affixed to the GV wall, fed the magnet with its own transfer line (MTL) and the 100 L GV buffer dewar with yet another transfer line (100TL). The refrigerator itself gets helium from the dewar with a rigid, “L”-shaped transfer line (LTL).

The preparation process for readying the LHe transfer system will not be discussed in detail here¹⁶, but is sufficiently involved as each major component of Figure 4.55 has its own vacuum jacket that must be tested, o-ring vacuum seals, leak checking procedure and assorted Goddard fittings for adapting to adjacent components. Furthermore, since one team is required at each end of the WTL, a radio communications protocol was established to properly coordinate the LHe transfer procedure.

4.5.1 LHe Transfer Losses

To cool the refrigerator from room temperature, LHe is brought into the system where heat meets the liquid helium and, after stored energy in the latent heat of vaporization is surpassed, boils off as cold gas which is pumped away. In this section, the term *liquid helium loss* refers to any liquid that is not used in this way. Expected losses can be planned for and quantified, such as cooling the vessels or transfer lines in Figure 4.55 down from room temperature. Unexpected losses include discovering a vacuum jacket has been breached, unforeseen heat leaks and misuse of the transfer equipment by personnel.

The largest single unexpected loss came from the 500 L dewar, acquired from a discarded helium liquifier system at Brookhaven National Laboratory, which was leak checked and vacuum tested at room temperature. After being filled with LHe, the dewar inlet frosted and helium rapidly boiled off. While most well-maintained dewars lose approximately

¹⁶See the Hifrost Manual[Duv15a].

1 % of their maximum capacity per day, we saw the 500 L dewar lose 80 L in 24 hours. Unfortunately, a liquid helium level probe wasn't readily available until late 2013, so determining this dewar deficiency took place over several LHe deliveries spanning July 2013 until August 2014. The solution was to remove the 500 L dewar and UTL from the schematic in Figure 4.55 and connect the delivery dewar directly to the WTL.

Another significant loss during noninitial 100 L dewar fills, i.e., fills where the 100 L dewar is already cold, was due to warm helium gas coming from the WTL being transferred below the liquid level line of the 100 L dewar. Under ideal circumstances, gas blown out of the WTL as it cools from room temperature would be evacuated to atmosphere before the liquid flow is diverted to the receiving dewar. Figure 4.56 shows the losses accumulated by not having this functionality built in.

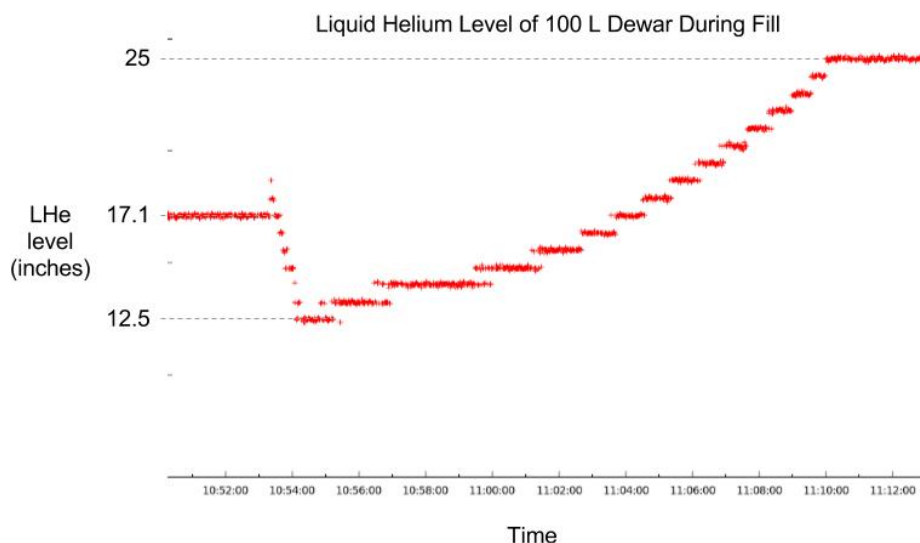


Figure 4.56: Example of LHe loss in the 100 L dewar during a top off transfer in the July 2014 cooldown. The initial dip between 10:53 and 10:54 shows the loss. Each inch corresponds to roughly 5 liters, so the LHe loss shown is a little over 23 liters.

The solution was to install a tee and ball valve on the 100TL on the emergency relief valve connector (see top of 100TL in Figure 4.55). Before the 100TL shutoff valve opens gas flow from the WTL into the dewar, the ball valve is opened to let the warm gas vent.

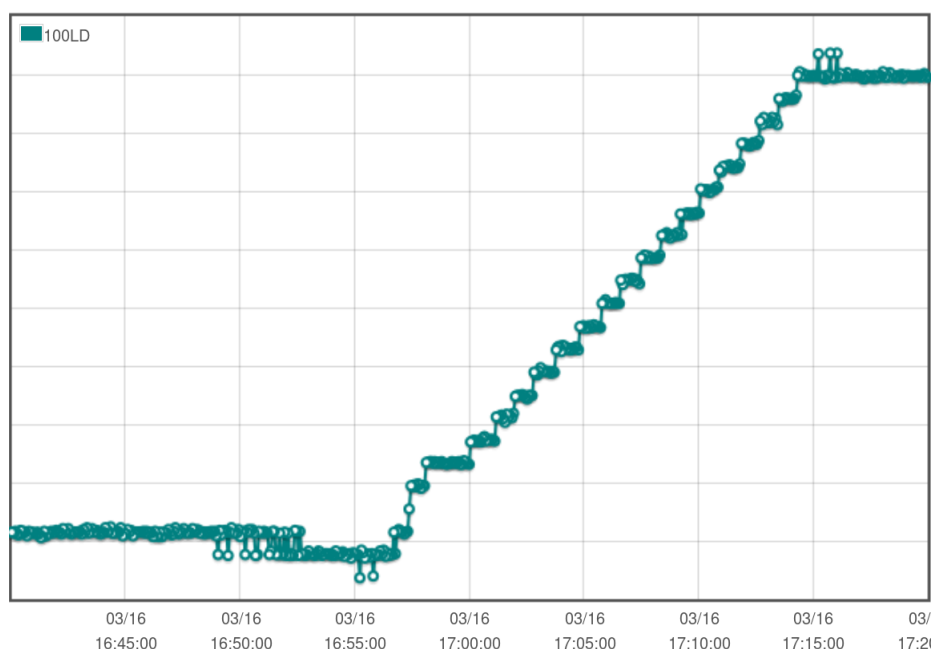


Figure 4.57: LHe loss in the 100 L dewar during a top off transfer in the March 2015 cooldown after the ball valve was installed. The initial fill loss beginning around 16:50 was 5 liters, or 20% of that shown in Figure 4.56.

When the vented gas becomes very cold, it is redirected to the dewar to begin the liquid transfer.

The last noteworthy transfer loss comes in the form of cooling down the WTL each time the dewar in the Gamma Vault is topped off. When the system design in Figure 4.55 was first settled upon around 2010, it was intended to be a continuous flow transfer between the 100 L and 500 L dewars. It appears the heat leak calculation from the WTL manufacturer was either overlooked or misunderstood. After the above LHe transfer solutions were implemented and we still saw 40-60 L losses during transfers, we had the manufacturer resend the heat leak calculation for the WTL. The expected leak is between 7-8 W (or over 200 liters LHe per day), two orders of magnitude higher than what we lose in the 100 L dewar, and about double the actual usage of the refrigerator in operation.

Operating under these conditions simply is not possible, so instead the helium transfer has been made in discrete fills, allowing all transfer lines to warm up between fills. At two

fills per day, we are still losing around 100 L LHe per day to the WTL. A proper solution has not yet been agreed upon, but recommendations involve skipping the WTL altogether by finding a way to bring delivery dewars directly into the Gamma Vault for 100 L dewar fills.

4.5.2 LHe Probe

There was no reliable way of measuring LHe levels in the 500 L dewar or delivery dewars until we specified and purchased a level probe from AMI. A schematic drawing of the level probe is provided in Figure 4.58.

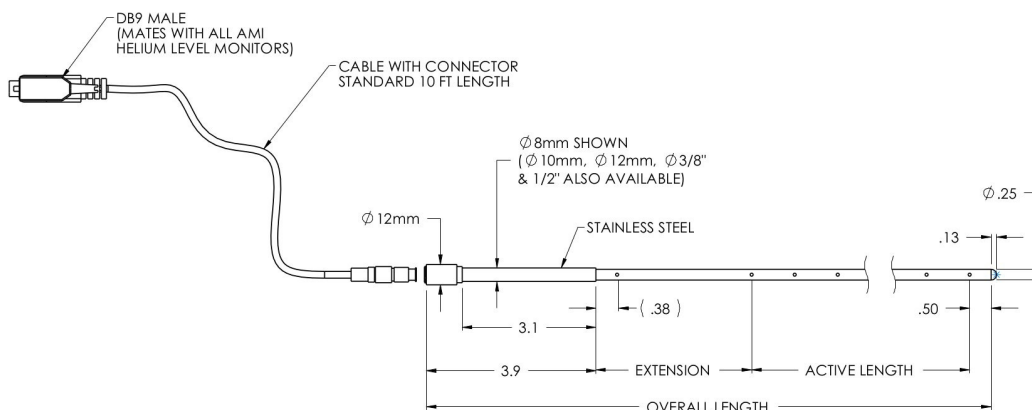


Figure 4.58: Drawing of our LHe level probe provided by the manufacturer, AMI.

The probe effectively works as a potentiometer, with the resistance of a vertical NbTi wire constantly measured. As the probe is lowered into a LHe vessel, the fraction of the wire that is submerged goes superconducting and is manifest as a drop in measured resistance.

The probe was designed to continuously reside within the 500 L dewar and monitor the level periodically. However, we specified a non-standard, stainless steel sleeve on the top of the probe so it could also accommodate 250 L delivery dewars¹⁷. The long sleeve allows a Goddard fitting seal to be made at variable range along the probe, which minimizes losses and prevent cold vapor from escaping through the top of the dewar.

¹⁷Which was fortunate because this was nearly the sole utilization of the probe (see Section 4.5.1).

4.5.3 Thumper

A thumper is a hollow tube with one large, conical opening that is used as an alternative method to measure liquid helium. The method utilizes thermoacoustic effects which cause a spontaneous sound, called Taconis oscillations, to emerge from a stainless steel tube when one side is at room temperature and the other is submerged in liquid helium. While visiting the HD-ice laboratory at Jefferson National Lab, a thumper was utilized for a secondary sanity check on a delivery dewar's liquid level. We decided to build our own in an attempt to simplify the frequent delivery dewar level measurements and free up the AMI level probe for other uses.

In January 2015, the thumper was made from a 6 foot long, 1/4 inch outer diameter, 304SS tube and a 304SS KF-40 blank. A 1.5 inch hole was bored into the blank before it was welded to the long tube. A latex membrane was fit over the flange and secured.

The thumper was used throughout the March 2015 cooldown (see Section 6.2.5) and found to perform quite well, with cross calibrations results shown in Table 4.3.

Thumper measurement (L)	Probe measurement (L)	Error
260	260	0%
11.5	12	1.7%
2	0	6.8%
13	10.7	7.9%
1	0	3.4%
12.75	14.7	6.7%
29	28.5	1.7%

Table 4.3: LHe level measurements of delivery dewars (29 inch depth when full) made with both the AMI level probe and the thumper.

4.6 Indium Extrusion

Both the MC and IVC flanges are sealed with indium inside the refrigerator. Indium wire seals have the nice property of filling small gaps at even very low temperatures as the indium flows under the high pressure of the mating flanges. This section discusses how we made our indium wire supply. Much of it is from the Hifrost Manual[Duv15a] section of the same name, which itself heavily sources a technical document on indium extrusion made at DFELL[TD14].

Hifrost requires indium wire precisely 1 mm in diameter for ^3He sensitive seals. The indium is cleaned away after use, and the metal is recovered due to its scarcity and ability to extrude more useful wire from it. A seal may not be used twice.

The Indium Association of America charges roughly \$1000 for 13 feet, or about \$20-30 per seal, so it is worth creating our own wire from the so-called “scraps”, or remnants of previous indium seals. Indium extrusion is the name of the process that transforms bulk indium into nicely shaped wire.

4.6.1 Background

Indium scraps or ingots are put into a hollow cylinder with a small hole in the bottom and softened with heat before being pushed through to make 1 mm OD wire. The melting point of indium is about 150°C , but actually approaching this temperature leaves the indium “runny” and impossible to shape. We have found heating the cylinder to 100°C with a heating tape yields the ideal consistency to make useful wire consistently.

The first iteration of the indium die¹⁸ had a 1 mm hole, intended to match the resultant wire. Instead, this produced 0.75 mm indium which was too small to seal the MC and IVC flanges. We increased the die hole to 41 mil, about 5% larger, and the indium wire produced

¹⁸A die is the plate at the bottom of the hollow cylinder that has a small hole for shaping indium.

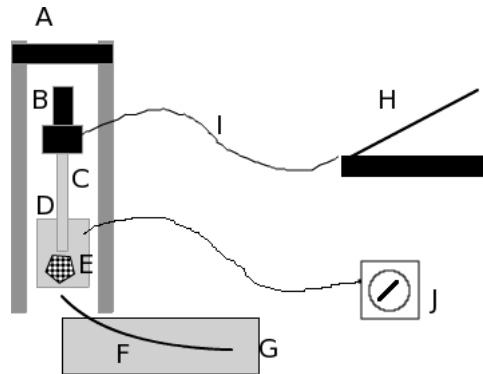


Figure 4.59: Indium extruder setup: A) extruder stand, B) hydraulic pump, C) steel rod, D) extrusion cylinder, E) indium scrap/ingot fragments, F) finished wire exiting die, G) sterile wipe sheet, H) hand jack, I) hydraulic line, J) thermocouple gauge

had an OD close to 1 mm, as desired.

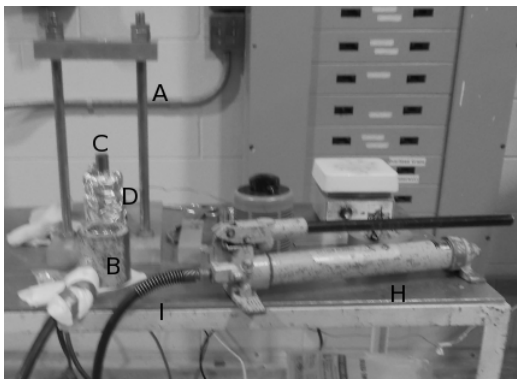
When extruding the indium, a varying force on the hydraulic pump sometimes leads to uneven wire, looking something like sausage links. To prevent this, a continuous, non-varying force should be applied for an entire press.

4.6.2 Materials

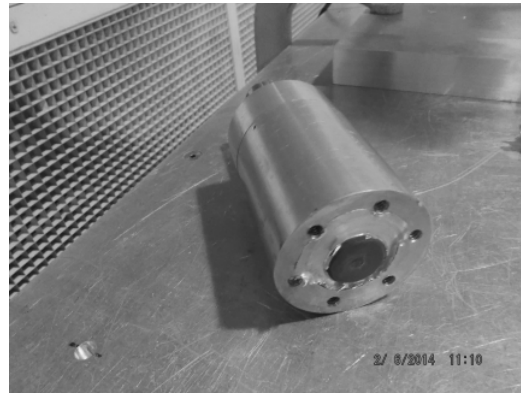
Select materials used for extrusion are shown in Figure 4.59 and described in detail below. A complete list of materials with descriptions is documented elsewhere[TD14].

The extrusion cylinder is made of aluminum and has six 1/4-20 bolt holes tapped in the bottom. The inside is lined with a hollow steel cylinder, which precisely matches the size of a steel rod insert. There is a small hole drilled in the side of the aluminum for a thermocouple thermometer sensor.

Screwed into the bottom of the extrusion cylinder is the indium die, a plate with a hole through the middle to push indium through. The exit hole in the bottom of the die shapes and defines the size of the indium wire. The die is a separate component from the extrusion cylinder for cleaning and modularity reasons. Indium is generally recovered from scraps of old seals or ingots bought from the Indium Association of America. Ingots are cut to size so



(a) A photo of the setup.



(b) The extruder cylinder without the die. The steel rod is plunged all the way down and leftover indium can be seen on the surface.

Figure 4.60: Photos of the indium extruder setup.

they fit inside the extrusion cylinder.

The extrusion stand is a structural, horizontal bar for the hydraulic press to push against when pressure is applied to the extrusion cylinder. The hole in the base of the stand is where indium wire is collected.

Heating tapes warm the indium while being pressed and should be long enough to wrap around the cylinder to warm it evenly. A layer of aluminum foil is wrapped around them to keep the heat from dissipating away, and a variable alternating current unit adjusts the temperature. A thermocouple sensor is used with an accompanying readout to monitor the temperature of the extrusion cylinder.

Step-by-step instructions for pressing the indium are given in the technical document available at DFELL[TD14]. Figure 4.61 shows the finished setup in use. Once the process was mastered, Hifrost has exclusively used our own extruded 1 mm indium for all MC and IVC seals since February 2014.



Figure 4.61: The hydraulic press sitting on top of the extrusion cylinder.

4.7 Holding Field

A solenoid magnet was made at UVa in November 2015. Complete details are in a technical note[Duv15b], of which parts are included in the rest of this section. See Section 2.5 for details about the purpose of the holding field.

4.7.1 Geometric Limitations

The holding coil is able to be less massive than the polarizing magnet for two reasons. First, there are fewer turns in the winding because the field doesn't need to be as high. Second and more significantly, the holding coil does not need its own cooling mechanism since it is located in the cryostat. This implies no additional nitrogen jacket, steel walls, vacuum walls or heavy mechanical supports are needed.

Sharing the cooling mechanism with the cryostat, however, is at the root of greatest technical hurdle of the frozen spin configuration: geometry. The coil must exist in the very tight radial clearance between shells of the cryostat. In our system, the coil is wound between the inner vacuum chamber (IVC) can and the outer vacuum chamber (OVC) can, within a radial clearance specified to 500 microns.

Our previous coil and IVC can is shown in Figures 4.62 and 4.63 with a layer of 71 micron thick teflon tape wrapped around them. The OVC was then installed and removed and the result is shown in Figures 4.64 and 4.65: the inner OVC wall pressed firmly against the coil and IVC.

The reason this happened is that coil is at least 180 microns too thick radially, which is the diameter of the wire. The result of a cooldown using this coil is shown in the plot of coil resistance vs. time in Figure 4.66. The coil resistance did not drop below $9\ \Omega$, presumably because the firm contact between the coil and relatively hot OVC kept the temperature locally above the critical temperature of the wire.



Figure 4.62: Before: teflon tape wrapped around holding coil.



Figure 4.63: Before: opposite side.



Figure 4.64: After: the OVC made such firm contact with the coil that the wire is visible through the tape.



Figure 4.65: After: unwrapping the tape shows it is cleanly severed.

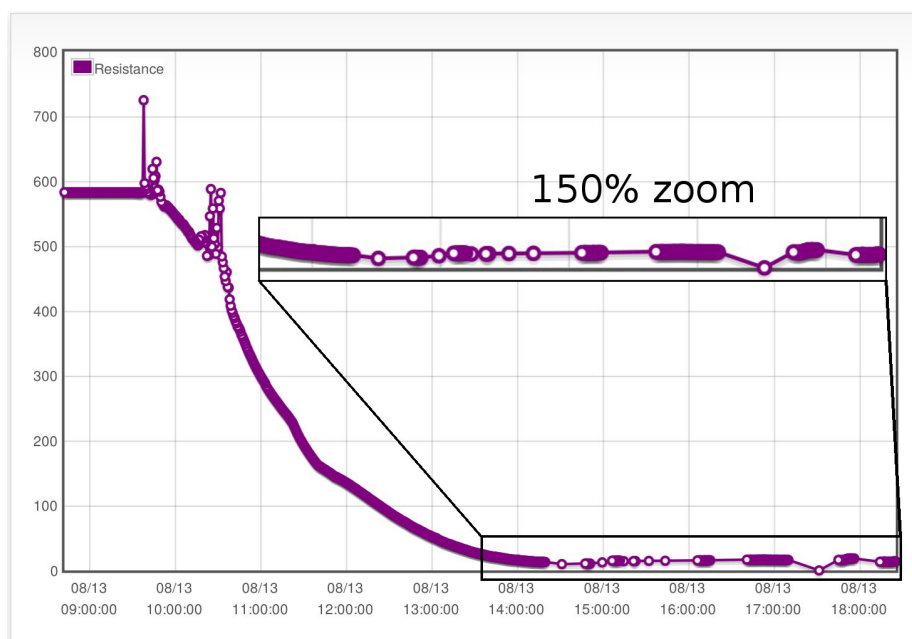


Figure 4.66: Plot of the resistance of the holding coil in ohms during the cooldown. Note that the coil never goes superconducting (the $0\ \Omega$ readings are from powercycling the electronics).

4.7.2 Inner Vacuum Chamber Can

The coil is wrapped around the narrowest section of the IVC can (see Figure 4.67), with two wire leads fed through the flange and into the 1 K evaporator to cool the solder joints to the refrigerator leads. Underneath the 250 micron thick AISI 316 L+N stainless steel IVC wall is an insulating vacuum isolating the mixing chamber[Nii15a]. Radially outward from the IVC is the inner wall of the OVC, which has an ID of 43 mm.

During normal running conditions, the coil is cooled by the superfluid film creep from the 1 K evaporator pot immediately upstream of the IVC[Nii76]. During the initial cooling period, it is important to lower the temperature of the entire refrigerator below 100 K as quickly as possible to prevent the target material from annealing. The large thermal mass of the IVC can and holding coil makes convective cooling insufficient to reach 100 K in a timely manner, i.e. $\mathcal{O}(\text{minutes})$. To speed up this cooling, a “bypass” capillary¹⁹ runs

¹⁹The bypass capillary is 316H19TW tubing purchased from MicroGroup, 42.5 mil OD and 5 mil wall,

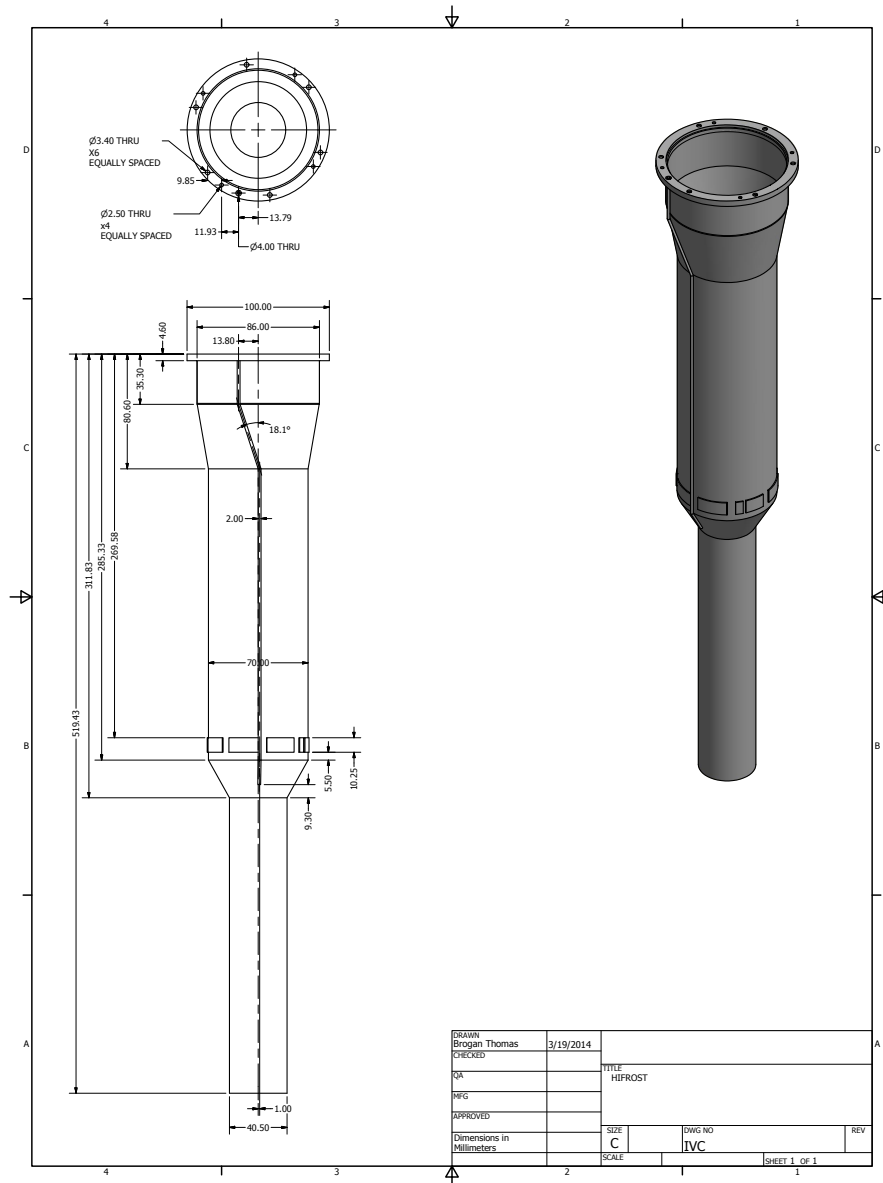


Figure 4.67: Drawing of the IVC with the CERN coil installed. Note that the 40.50 mm diameter includes the thickness of CERN's coil and epoxy. With no coil, that diameter is 39.34 mm (see Figure 4.69).

downstream along the IVC wall.

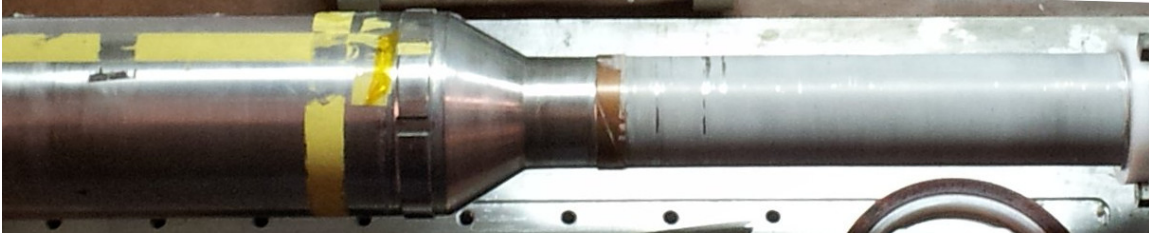


Figure 4.68: Profile view of IVC before winding.

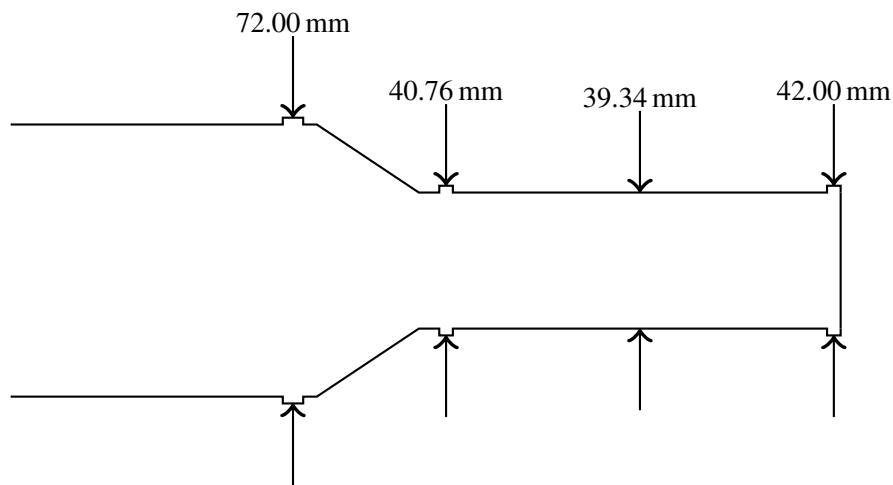


Figure 4.69: Radial measurements of features in Figure 4.68 (not to scale). The feature at the end is the weld seam from the stainless steel end cap.

4.7.3 Equipment

A detailed list of equipment necessary for the winding is available elsewhere[Duv15b], but select components are listed below.

Coil Wire

Superconducting wire from Supcon Inc, type: 54S43, diameter: 6 mil bare (7 mil rolled to oval cross section with minor axis ≈ 760 micron and attached with eutectic solder along the side of the IVC can. See Section 4.2.4 for details.

formvar), material: CuSc ($1.3 \pm 0.1:1$), nominal length: 1600 feet, measured resistance: 847Ω .

Teflon Bearing

A shallow insert that rests in the IVC flange and sits on the indium shelf. A central hole is bored to constrain the can on the axis of the lathe, shown in Figures 4.70 and 4.71.

Clutch

A delrin ring cut to size of the steel endcap and press-fit onto the IVC. See Figures 4.72 and 4.73. The clutch always turns with the lathe jaws, but the IVC either rotates or slips in the clutch depending on the friction applied by the user.

Tension Spring/Rail

A spring adjusts the height of the tension rail during winding. Supercon's technical support recommends referencing their standard wire chart[Equ] which lists less than half a pound for our wire, which the tension spring and rail provide.

Stycast 1265 Epoxy Parts A and B

Stycast 1265 is characterized by the manufacturer as a long pot life, low viscosity epoxy for sealing coil turns together[EC].

4.7.4 Coil Winding Procedure

Preparation

1. The resistance of the nominal 1600 foot spool of 54S43 wire was measured to be 847Ω , putting the resistance per unit length close to the nominal $1.7 \Omega/\text{m}$.
2. The outer diameters of the IVC can's features were measured as shown in Figure 4.69.

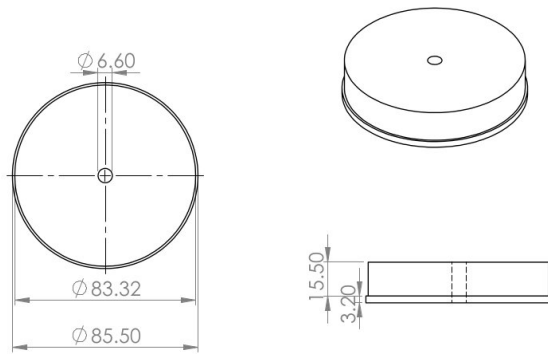


Figure 4.70: Drawing of teflon bearing (units mm).

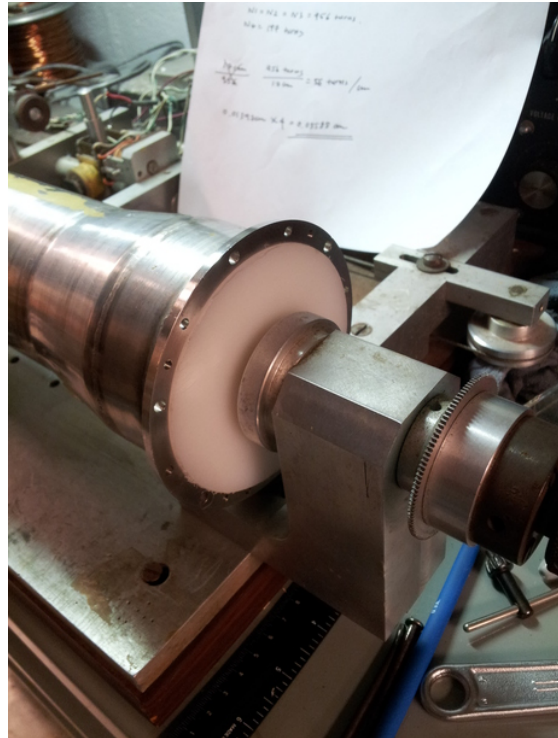


Figure 4.71: Teflon bearing installed in IVC.

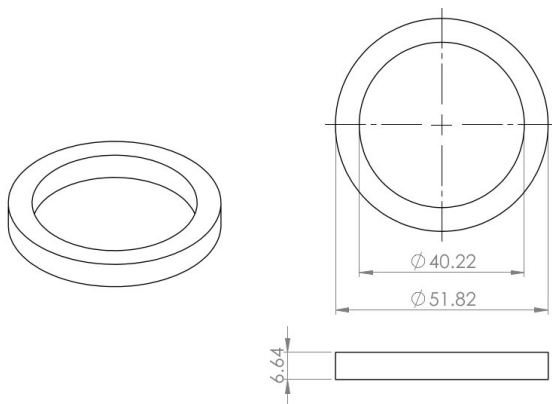


Figure 4.72: Drawing of delrin clutch (units mm).

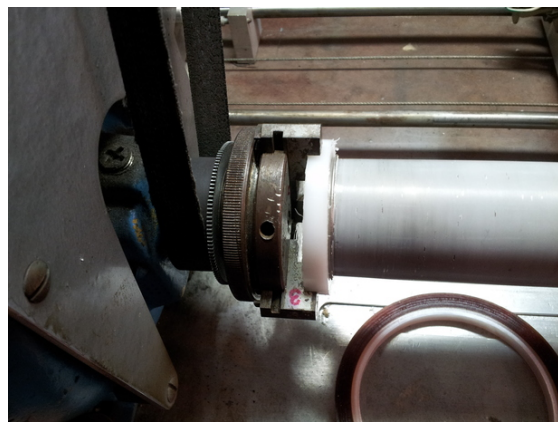


Figure 4.73: Delrin clutch in lathe jaws. Note that the clutch was bored in 10 mil increments until it press-fit on the IVC nose. This is necessary due to the deviations in the steel surface.

3. The entire application surface was cleaned with acetone and isopropyl alcohol.
4. The IVC can is set up in the lathe jaws with the delrin clutch (Figure 4.73), teflon bearing (Figure 4.71) and tension bar.

Winding

First Layer

1. We drew approximately 1-2 m of wire and wrapped it around the can just upstream of the brass ring (40.76 mm diameter section in Figure 4.69) and taped it in place. This is one of the leads that travel up the refrigerator to the 1 K pot.
2. We set the lead in the guiding notch cut in the brass ring (see Figure 4.68) and taped it in place.
3. We started rotating the IVC with the lathe at about 1 Hz, using a free hand to manually slow down the can. The clutch prevented the lathe from stalling.
4. As the IVC rotated, the delrin scraper was used to set each loop into place next to the previous loop. Gaps, shown in Figure 4.74, are easily seen since the metal underneath reflects light between the coil's dark red insulation.
5. It took about 5 hours to nearly finish the layer.
6. Near the last few turns, there was no room for the scraper to align the wire, so the turns were looped directly into place. This took more time but was possible by carefully translating the wire feed.
7. The outer diameter of the layer was measured to be 39.7 mm.
8. We applied 8-10 equally spaced drops of Stycast epoxy to the first layer, as shown in Figure 4.75.

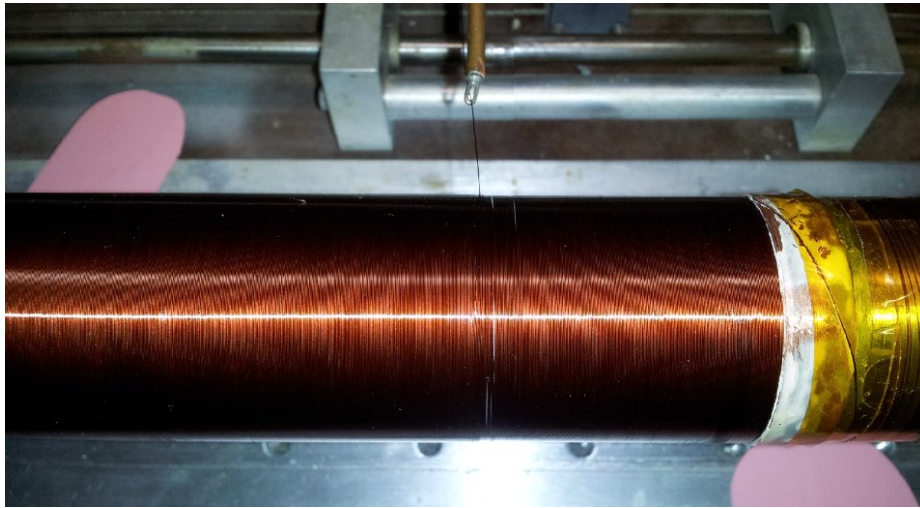


Figure 4.74: Tiny gaps, less than the 180 micron wire diameter across, are visible in the first layer because the can and coil are different colors.



Figure 4.75: Drops of epoxy being applied to first layer. We relied on the epoxy's low viscosity and the constant rotating of the IVC to evenly spread it across the layer.

Second Layer

1. We reversed direction on the translating wire feed to begin winding the second layer.
2. We proceeded as with the first layer, except the delrin scraper was used more gently since it is possible to shift the turns of the first layer.
3. The can was turned slower, around 0.25-0.5 Hz, because it is harder to wind turns over an existing layer of turns.
4. Halfway through, we applied more epoxy to the remainder of the exposed first layer.
5. We repeated the same routine at the end of the layer, meticulously translating the wire feed to wind the turns in place after the delrin scraper could no longer fit.
6. We measured the OD of the second layer to be 40.0 mm.
7. It took about 5 hours to wind the second layer.

Third Layer

1. We applied 10 more drops of epoxy before winding the third layer, as shown in Figure 4.76.
2. This entire layer was wound by hand since it was too difficult to align the turns over the second layer with the lathe. We timed 17 turns in 9 minutes and 52 seconds.
3. We eventually used a magnifying glass when it was difficult to see gaps being made between turns in the third layer.

4. We measured the OD of the third layer to be 40.34 mm.
5. It took about 9 hours to wind the third layer.

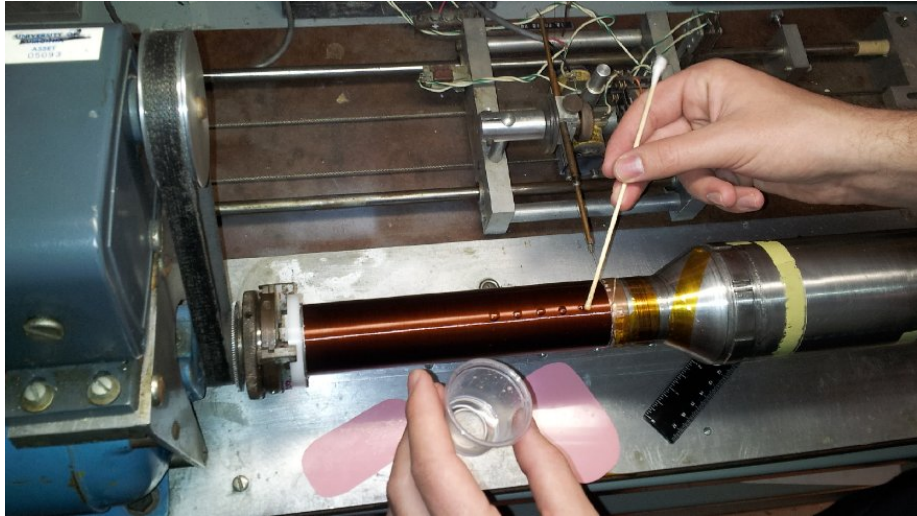


Figure 4.76: Begin applying epoxy after winding second layer.

Fourth Layer (fringe coils) ²⁰

1. We began winding the layer as the others, but stopped approximately 2 cm from the downstream end of the can.
2. We wrapped the layer in Kapton tape to prevent it from uncoiling and wound one long, helical turn so the wire reached approximately 2 cm from the upstream end of the solenoid (see Figure 4.77).
3. Epoxy was applied to several parts of the helical turn, then reinforced with tape so the helix didn't unwind at the start of the next step (see Figure 4.77).

²⁰The fourth layer consists of two so-called “fringe coils”: a limited number of additional turns at each end of the solenoid intended to minimize the geometric effect of the magnet’s finite length on the field away from its center. Rather than calculate the effect of the number of turns, we have chosen “a few centimeters” based on papers from other groups. Citation: private correspondence with P. Seo.

4. We finished winding the fringe coil like the other layers (see Figure 4.78) and measured the OD of the fourth layer to be 40.60 mm.
5. At the end of the fringe coil, we again passed the wire through the second guiding notch (opposite side of the brass ring shown in Figure 4.68) and wound approximately 2 meters of coil around the can to use as the second lead to the 1 K pot.
6. The wire lead was cut and taped in place. We stripped 1 cm of insulation off each lead and measured the resistance of the entire holding magnet to be $0.6\text{ k}\Omega$.

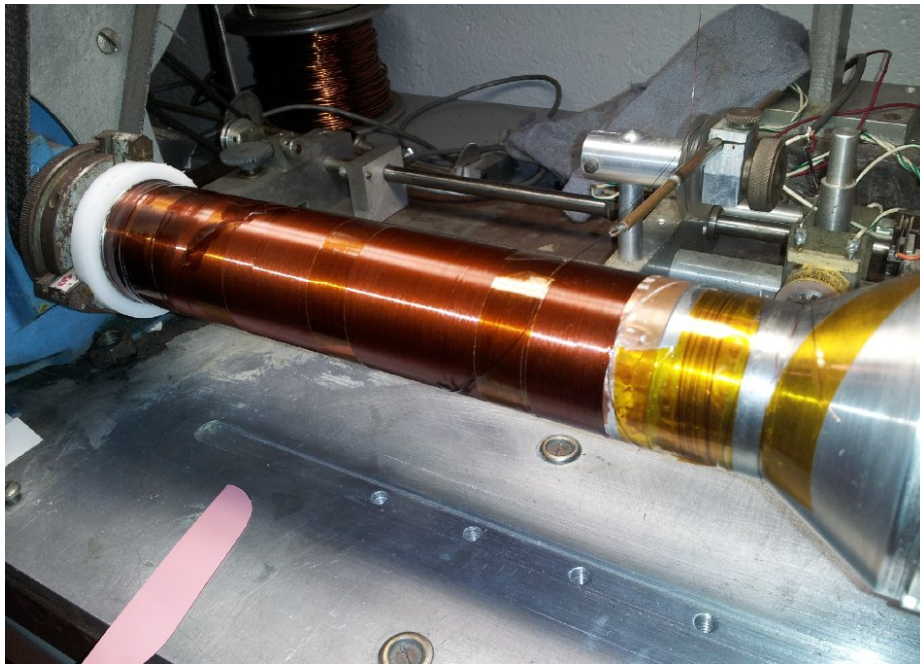


Figure 4.77: Halfway done with the fringe coils.

4.7.5 Magnetic Field Test

Before being run inside the refrigerator, the holding field must be ramped up in a controlled environment to be sure it is capable of handling the required current. Once it is



Figure 4.78: Finishing the fringe coils.

shown to operate correctly on its own, it can be installed in the polarized target and tested in situ.

Results

The magnetic field was first tested at a fixed location with varying currents. The location (or “depth”) was chosen to be the downstream end of the solenoid, conventionally called 0 cm. As the current was swept from 0-15 A, the field was recorded and is plotted in Figure 4.79.

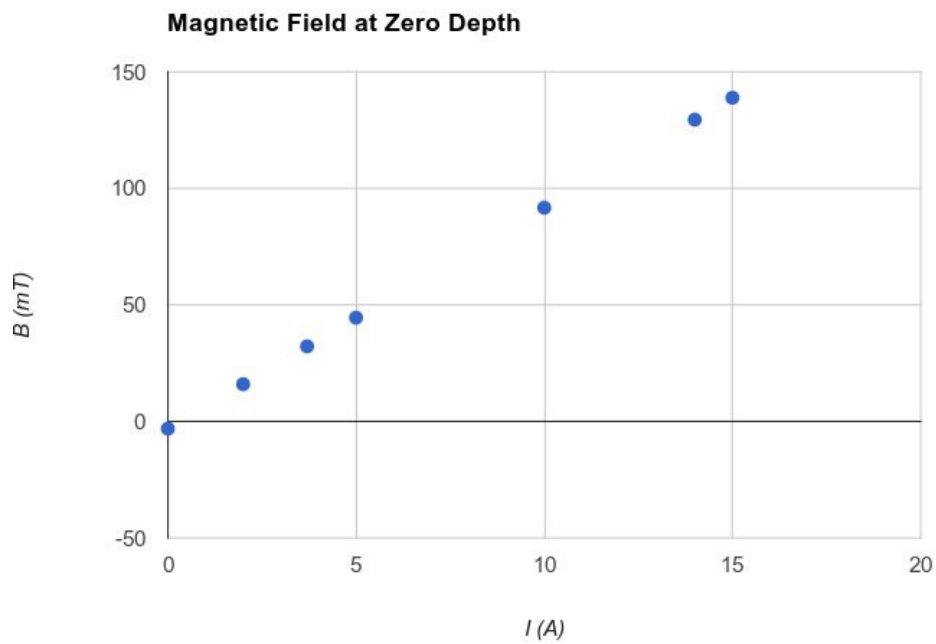


Figure 4.79: At depth 0, the current is changed the field is recorded.

Then, the current was kept at 12 A and the magnet probe was swept through depths from 0-27 cm.

The linear relationship between the current and field in Figure 4.79 extrapolates to a 250 mT field at about 25 A, which is both the expected value and in agreement with the previous coil.

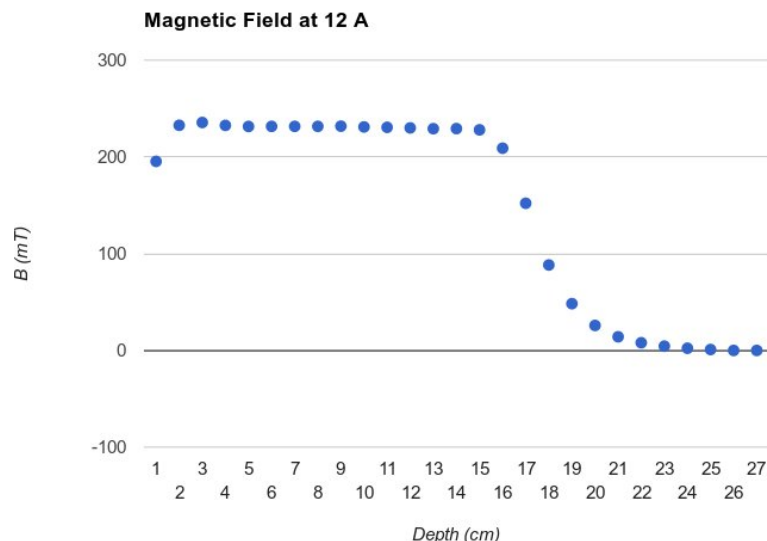


Figure 4.80: At $I=12$ A, the depth of the sensor is changed the measured field is recorded.

4.7.6 Performance

In early December 2015, the IVC was installed and the resistance of the new coil was continuously monitored. After six hours of cooling, the coil went fully superconducting (see Figure 4.81), confirming the heat touch was resolved.

4.8 OVC Track

During refrigerator assembly procedures at Duke, the OVC is installed in a vertical position; the refrigerator swing developed was designed to make this as simple as possible. There is no similar swing mechanism at UVa, so the OVC must be installed horizontally after the refrigerator is mounted. This often had to be done by an individual researcher and, once the teflon tape tests described in Section 4.7.1 began, up to several times a day for a period of weeks.

Gravity can not be used to align the OVC with the refrigerator during a horizontal assembly the way it can for a vertical assembly. This means the researcher must control the

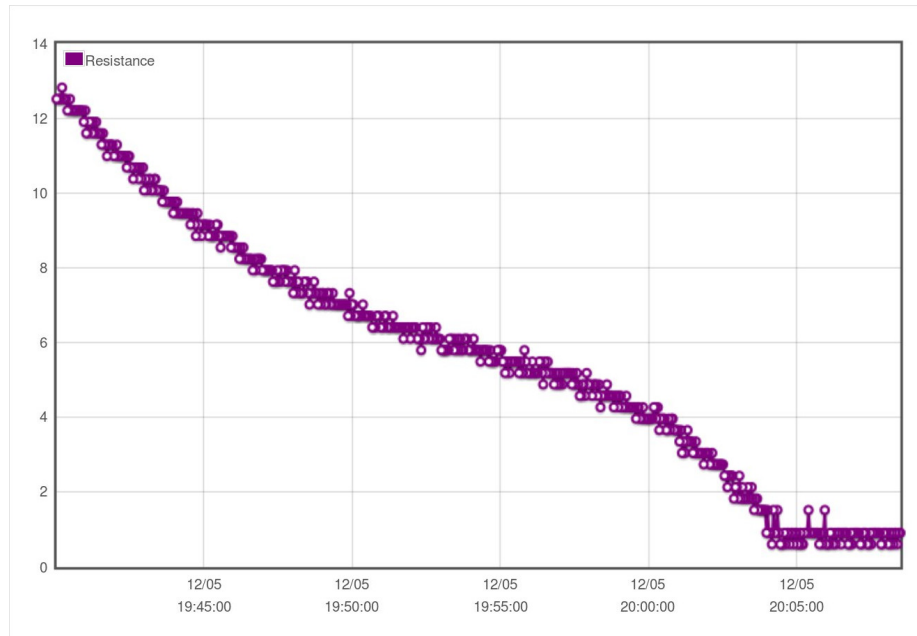
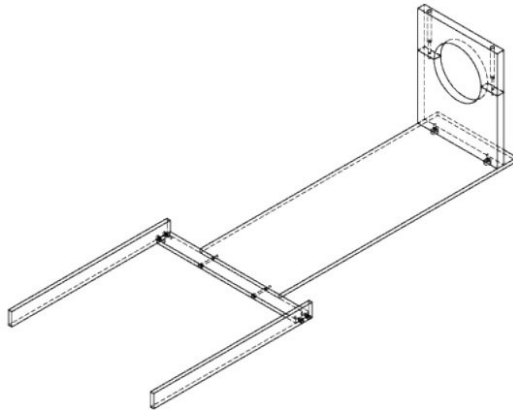


Figure 4.81: Graph of the holding coil resistance in Ω during the December 2015 test, which dropped to nearly zero shortly after 20:00. The marginal resistance is due to the leads between the magnet power supply and the superconducting leads inside the refrigerator.

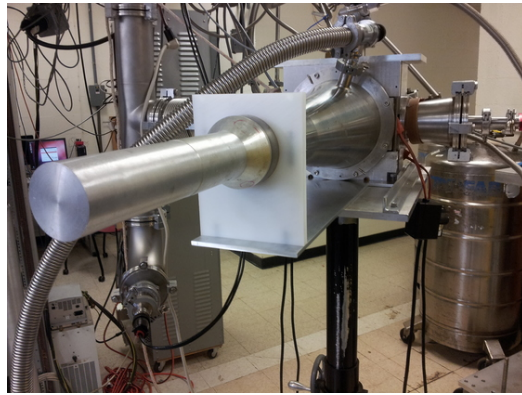
pitch, yaw and roll of the OVC while sliding it over the IVC while being careful not bump any fragile components of the refrigerator. Recalling that the clearance between the OVC and parts of the IVC is as small as 100 microns, we determined we needed to find a more systematic and reproducible way to install the OVC to minimize the risk of damage to the refrigerator.

A system called the OVC track, shown in Figure 4.82, was designed to solve the problem. A sheet of UHMW polyethylene was cut and split to fit the cylindrical section of the outer OVC can. Both sides are drilled with the lower side tapped, which secure the plastic to the OVC. The entire polyethylene sheet is fastened to an aluminum plate, on which an alignment fork built on the opposing side.

Since the track was installed, neither the OVC nor the rest of the refrigerator has incurred damage due to the OVC assembly procedure, despite a large increase in the number of installations.



(a) Drawing of the OVC track.



(b) Photo after the OVC track has been installed on the refrigerator.

Figure 4.82: The OVC track allows a more reproducible installation when the refrigerator is horizontally mounted, minimizing the risk of damage by colliding the OVC into other parts of the refrigerator.

Chapter 5

Geant4 Simulations

The GDH Sum Rule, covered in Section 1.3.1, will be the first experiment run with Hifrost at DFEL. The Blowfish detector array will record the angle and energies of neutrons, products of deuteron photodisintegration, that are ejected from the target.

However, it is an oversimplification to interpret the direction and energy which neutrons are detected as the same direction and energy with which they emerged from the collision site. They must pass through, on average, 0.5 inch frozen butanol, either pure liquid ^3He or a $^3\text{He}/^4\text{He}$ mixture, two stainless steel vacuum cans, the NbTi/Cu holding field coil, an aluminum vacuum can, two copper radiation shields, between 12-15 inches of air and the housing and insulation around the neutron detector cells.

We use a physics simulation toolkit called Geant4 to map the properties of detected neutrons to those they emerged from the target with. The simulations are based on the *BlowfishX* template, which was initially used for other experiments but was written in a modular fashion, allowing the simple target to be replaced with the Hifrost target[Wur10].

The innerworkings of Geant4 and the implementation of the Blowfish package is covered at length by authors that extensively used it for numeric analysis[Pri14]. Until an experiment is run with Hifrost, no such data is available for similar analysis and the framework to

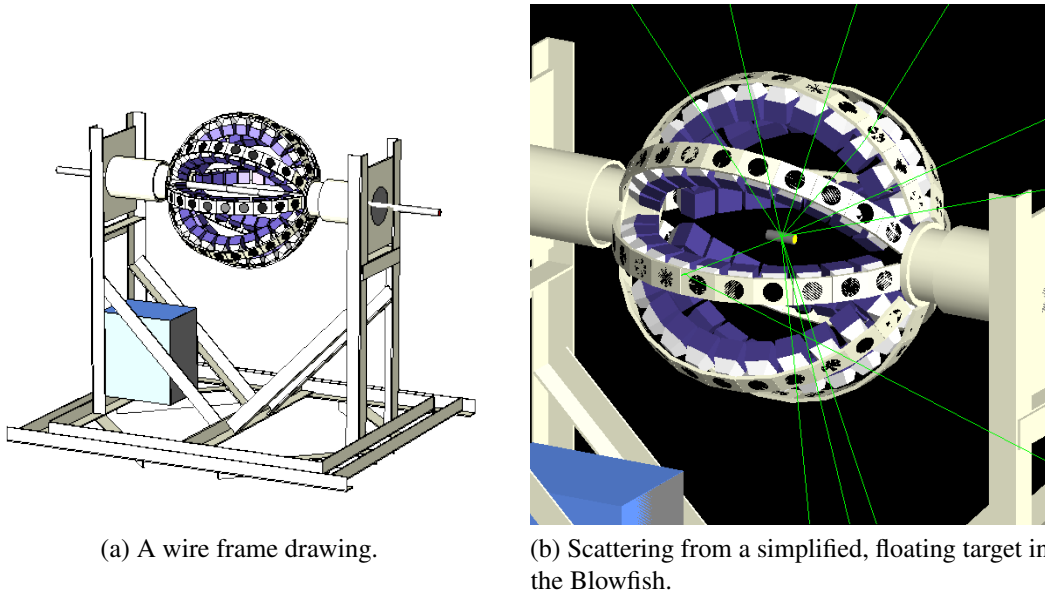


Figure 5.1: A simulation of the Blowfish detector array.

convert the detector data into ROOT format and compare with Geant code will not be covered here. Instead, we cover the changes to the simulation.

In May 2015, a simulation of the refrigerator based on measurements of the MC, IVC and OVC shells was completed and added to the simulation[Pyw15].

5.1 Gamma Attenuation

Ordinarily, a simulation begins with neutrons being emitted from the target with some specified angular distribution. To first order approximation, all neutrons begin propagating radially outward from the center of the target, which coincides with the center of the Blowfish array. To second order, they maintain the same angular distribution but have their origin shifted to a uniformly random position in the target holder¹.

While a very small fraction of total gammas will cause deuteron photodisintegration, a significant portion will contribute to nuclear or atomic elastic interactions, thus becoming

¹This is justified because the DFELL gamma beam profile is very close to uniform.

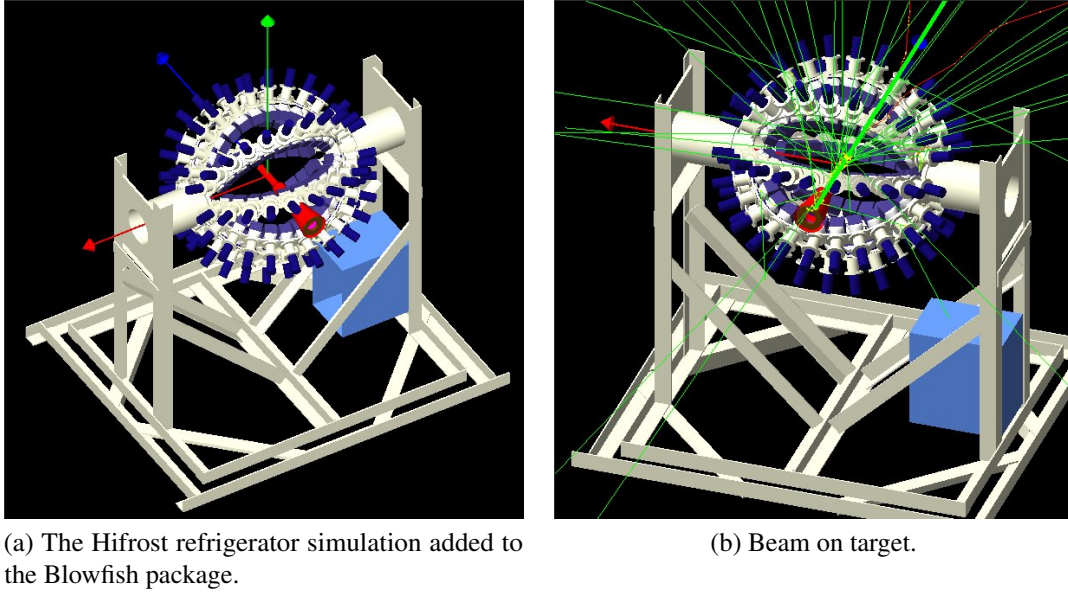


Figure 5.2: The gamma beam (green) is simulated to propagate along the refrigerator axis. The Geant visualization manager shows the paths of scattered particles.

ineligible for (or less likely to participate in) downstream interactions. Therefore, instead of randomly originating neutrons throughout the target, our simulation should have a weighting function f preferentially pick upstream coordinates. While f would theoretically be a simple exponential with distance along the beam axis, effects like the cross section dependence and geometric effects of elastic scattering complicate the situation.

We find f empirically by changing the primary generators in the Geant simulation to gammas at the same energy we expect the DFELL to produce and targeting them along the beam axis towards the refrigerator. The target is separated into ten logical volumes, and as each gamma traverses a new volume its energy is recorded. Any entry indicating the gamma has lost energy since it last entered a target sector is interpreted as an interaction in the previous sector. As a course measure, expelling all gammas that have interacted in a previous volume implies the surviving number of gammas eligible for photodisintegration in the current volume, which determines the probability of an interaction.

Figure 5.3 shows the results of a one million event test on a 20 cm long target of

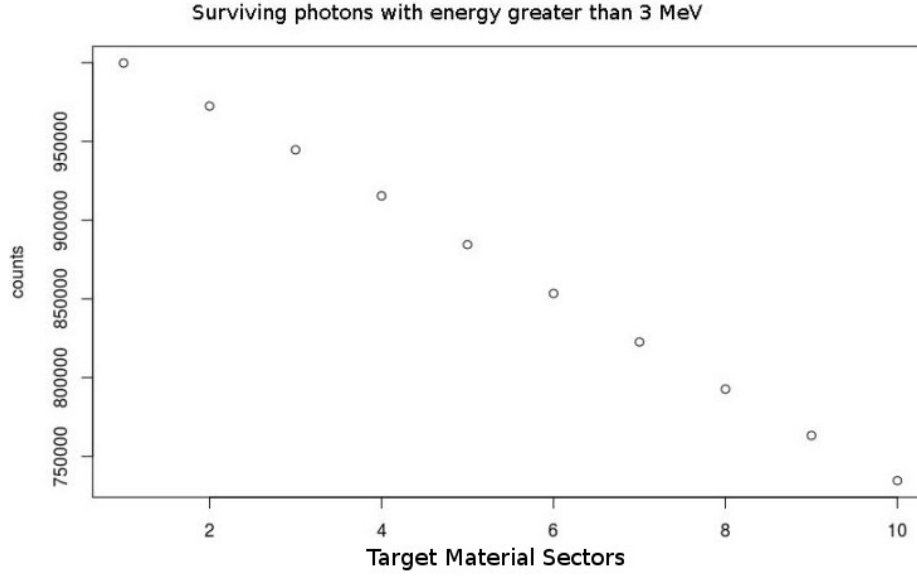


Figure 5.3: One million gammas are sent down the beamline at randomly spaced radial distances from the refrigerator axis (but within the target material). As each gamma passes through the ten target material sectors, each 2 cm long, it is removed from the simulation if it lost energy and allowed to continue propagating otherwise.

deuterized butanol. Nearly 75% of the gammas did not interact with the target material, and those that did followed a linear functional form for f :

$$f = -0.01716x + 1, \quad (5.1)$$

where x is in cm and the number of gammas entering the first sector is normalized to 1.

Chapter 6

Cooldown Results

One special category of commissioning runs tests the Hifrost subsystems at LHe temperatures and determines differences from room temperature operation when applicable. Due to the cost and volatility of supplied liquid helium, these so-called “cooldown” commissioning runs require adequate preparation and organization to make sure an optimal amount of helium is ordered and put to good use. Each cooldown has a clear list of objectives, a contingency plan if the goals are met unexpectedly quickly or not at all, and a brief (sometimes informal) report of the results.

6.1 UVa Cooldowns

The initial UVa cooldowns were primarily to test basic functionality of the refrigerator and the UVa polarized target cryogenic system, neither of which had even been tested since being shipped from Europe. At first, very basic questions about cryogenic equipment were answered, with subsequent cooldowns following up on uncertain points or testing solutions to known problems. Finally, the refrigerator was confirmed to operate at dilution temperatures before being transferred to Duke.

6.1.1 August 2012 - The First Cooling

Preparation

Much of the work done in early 2012 revolved around leak checking the ^3He , IVC and separator pump lines. Leaks were found throughout the 4 K section of the refrigerator and patched with Apiezon Q sealing compound, which works well at room temperature. Sensors were traced to the cable feedthroughs and connectivity was confirmed where possible.

Goals:

- The successful transfer of 4 K LHe into the refrigerator.
- Test ^4He thermometers down to 1 K.
- Test evaporator pressure gauges under operating conditions.
- Verify the evaporator and separator flow meters operate properly under load.
- Run all pumps, with gas load if applicable.
- Confirm all vacuum seals remain leak tight at low temperature.

Results:

- LHe was successfully transferred into the refrigerator.
- The ^4He temperature sensors did not work.
- The thermocouple pressure gauges did work but operated at too limited of a range to be useful, only registering from $10^{-3} - 10^0$ mbar.
- The counter current flow meter was off scale the entire cooldown; the shield and evaporator flow meters did not function at all.

- The mechanical evaporator pump overheated under gas load and triggered an interlock. The separator compressors were not capable of pulling adequate flow.
- The IVC line leaked at low temperatures.

Discussion and Followup

While the inaugural Hifrost cooldown was an overall success, the list of tasks with descriptions of successful completion is too long to enumerate here[Duv]. While the higher order equipment such as thermometers, flow meters and pumps largely failed during the cooldown, successfully assembling the vacuum system and refurbishing the pump stands to be operational was a success.

After the cooldown, the refrigerator sensor cables were rebuilt so they terminated with a D-shaped connector instead of being directly connected to the various instrument readouts with wire nuts. The plumbing that worked well was labelled and allocated a proper storage area and the leaky IVC plumbing was replaced. Varying thicknesses of indium wire were experimented with for making the IVC and MC seals: 70 mil, 30 mil and finally 40 mil. The MC itself, a CERN model made of teflon and Stycast, leaked at the teflon/stainless steel joint and was replaced with a quartz mixing chamber. The microwave guide port was sealed with a thin layer of FEP. New separator compressors were purchased and wired into the system and the auxiliary ^3He pump P8 was refurbished, rewired and reinstalled.

Another major success of the cooldown was the realization that the lab was understocked with vacuum components. It was necessary during the cooldown to modifying the IVC and separator manifolds, but there was an inadequate supply of KF o-rings, clamps, elbows, tees, hoses and adapters available to make the desired connections. Knowing this allowed us to replenish our vacuum supplies after the cooldown.

6.1.2 December 2012 - ^3He Circulation Attempt

The first cooldown where circulation in the ^3He section was attempted began December 5 and ended December 6 of 2012. The ^4He sensors that were reinstalled in the refrigerator did not read out properly and a new KNF compressor used on the separator threw a rod through its casing while in standby mode[Seo12a]. A new cold cathode gauge installed on the OVC and a piranni gauge installed on the IVC performed as expected.

The attempt to circulate ^3He gas in the circulation loop was short-lived. The LN_2 trap was found to have a crack in its bellows and a manual valve on the ^3He gas rack leaked both to atmosphere and across the seat of the valve[Duv13]. The refrigerator plugged almost immediately after circulation began.

6.1.3 February and April 2013 - Dilution

After correctly getting the refrigerator temperature sensors reading and a new electronic logging system (ELOG) installed in the lab, two attempts were made to operate the dilution section of the refrigerator in early 2013. The first attempt, on February 13, successfully saw some ^3He gas condensed in the refrigerator, but the group underestimated how long it would take to finish condensing and ran out of helium before dilution temperatures were met.

The second attempt occurred between April 8 and April 12. With enough liquid for two 100 L dewar fills, we had time to fully condense an unknown ratio of $^3\text{He}/^4\text{He}$ mixture and realize temperatures as low as 270 mK in the MC, according to a recently installed germanium thermometer.

6.2 Duke Cooldowns

After the successful dilution demonstration at UVa, the refrigerator was brought to Duke at the end of July 2013. The plan was to spend the summer commissioning the newly installed liquid helium transfer systems and vacuum pumps and taking beam on a polarized target by the end of November.

6.2.1 October 2013 - The First Duke Cooling

The first Duke cooldown was as much a test of the complex liquid helium transfer system as the refrigerator itself (see Figure 4.55). Unfortunately, with no liquid helium level probes, automatic slow control DAQ or proper evaporator flow meter/pressure gauge, the previous successes at UVa were not reproduced. Very few notes were logged during the cooldown, so it is very difficult to quantify the results and none are presented here. The near lack of a cooldown record was one indicator of what needed to change for future cooldowns.

6.2.2 December 2013 - An Unprepared Cooldown

The list of post-cooldown work at Duke was much longer than anticipated after the October run. Before the preparation was completed, the local group leader placed an order for 750 L of liquid helium, essentially forcing a cooldown with an ambitious list of goals, which were presented to the TUNL administration on December 9, 2013[Seo13].

Goals:

1. Operate the NMR.
2. Send microwaves into the refrigerator.
3. Ramp up polarizing magnet.

4. Ramp up holding magnet.
5. Achieve dilution.

Results:

1. The NMR was not ready to run.
2. The microwaves were not ready to run.
3. The polarizing magnet was not properly hooked up in time to test.
4. The holding magnet was not properly hooked up in time to test.
5. The MC reached a low of 275 K (nearly 0 °C).

Discussion and Followup

Despite the gap between the officially stated goals and the results of the cooldown, the December 2013 cooldown was successful in one way: the entire workgroup was overhauled, both on the TUNL and UVa sides. The need for organization and agreement amongst the group members was indisputable, and regular weekly engineering meetings and organized task lists became standard operation at DFELL. The UVa PI and polarized target physicists began to make regular trips on-site and provide more oversight to the group.

6.2.3 July 2014 - Dilution Cooldown #1

The first cooldown of 2014 was repeatedly delayed after damage to the refrigerator was uncovered in March. After being repaired at Jefferson Lab, cooldown preparation efforts focused on installing the ^3He recovery system (Section 4.4.2), running diagnostics on the circulation loop (Section 4.4.3) and getting the slow control DAQ online (Section 4.4.7).

Cooldown preparation was organized to allow time for the Hifrost team to complete all necessary prerequisites for helium ordering while remaining within the time constraints of the DFELL's beam schedule and the UVa-based group members. One flowchart showing some of the cooldown organization is shown in Figure 6.1. One indicator that the new organization was an improvement over that of the December 2013 cooldown is unexpected problems ended up delaying the cooldown by a sufficient length of time to correct them, as prescribed by the flowchart.

Goals:

1. Achieve MC temperatures below 100 mK.
2. Demonstrate persistent dilution.
3. Log conditions relevant to achieving and maintaining dilution.

Results:

1. The MC did not fall below 1 K.
2. Dilution was never achieved nor persisted.
3. The still heater was run but no effect was shown on the MC temperature.

Discussion and Followup

The cooldown was interrupted by the failure of the evaporator backing pump. After the delay of replacing it with another identical pump, the cooldown was resumed briefly before the second pump seized in a similar manner. The failure of the pumps was later explained by the limiting maximum compression of the Roots stack.

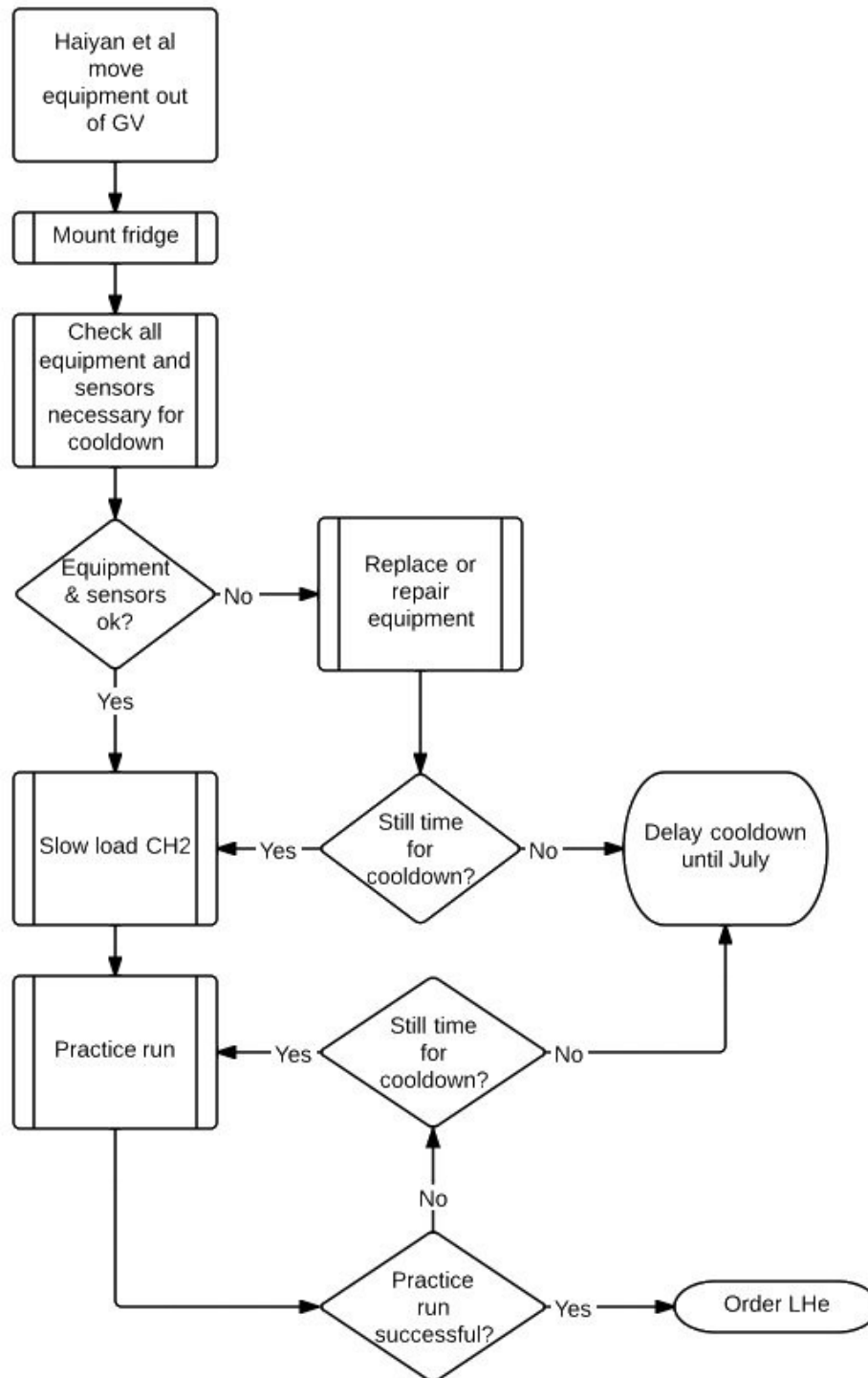


Figure 6.1: Decision tree governing the July 2014 cooldown prep, beginning when the Gamma Vault became accessible in June until the placement of an LHe order.

Additionally, 32 L of air was recovered from the ^3He tanks after the cooldown. The remaining helium gas matched the amount we started the cooldown with, strongly implying a leak to atmosphere in the low pressure section of the circulation loop brought in 32 L air contamination. The leak was later isolated to the ^3He Roots pump stack, the repair of which is described in Section 4.4.6.

Finally, peak records of the LHe transfer losses described in Section 4.5.1 caused us to solve the problem with an additional valved placed on the 100TL[Duv14].

6.2.4 October 2014 - Dilution Cooldown #2

After spending the summer and early autumn of 2014 addressing the ^3He air leak issue, we began a cooldown in early October with similar dilution goals to the previous cooldown.

Results:

1. Reached ≈ 200 mK in the MC.
2. Dilution was not run in a persistent manner.

Discussion and Followup

The cooldown began on October 8 and condensation from the ^3He tanks began on October 9, reaching a temperature of just under 200 mK (as read from the germanium resistor) in the MC. 40 L of contaminating gas was caught by the LN_2 trap in one day.

The cooldown was terminated when the evaporator Roots pumps failed to turn back on after the evaporator was starved of ^4He due to user error[Ken14]. Additional problems that arose include AVS47 error due to improperly shielded ^3He temperature sensor cables, a broken mechanical pump on the ^3He Roots stack and difficulties coordinating LHe transfers to the GV with the wall closed.

Finally, it was noted that the refrigerator was not capable of operating below 4 K at the prescribed separator flows. The higher flows were the cause of considerable icing on the back flanges and feedthroughs, which we suspected might be related to the contamination in the LN₂ trap. See Section 4.2.2 for details.

6.2.5 March 2015 - The Super Cooldown

After the promising dilution results of the previous cooldown, a so-called “Super Cooldown” was planned at Duke. If all goals were successfully met, this would be the penultimate commissioning run¹ before the GDH run took data.

Goals:

1. Operate at expected separator flows (20 SLPM total).
2. Achieve MC temperature required for frozen spin experiment (sub-100 mK).
3. Confirm circulation loop does not become contaminated during operation.
4. Observe dilution in steady state for 4 hours.
5. Ramp up holding field to frozen spin operational current.
6. Observe stable MC temperature in frozen spin mode for 48 hours.
7. Polarize CH₂ target with 2.5 T magnet.
8. Measure polarization with NMR.
9. Send microwaves into refrigerator and record refrigerator response.

¹Even if the Super Cooldown was successful, a cold target load would need to be practiced before a data run, requiring an additional commissioning cooldown.

10. Attempt to preserve thermal polarization with frozen spin mode.
11. Practice recovering CH₂ target material while the refrigerator is cold.

Results:

1. Separator flows of 70 SLPM were required to maintain LHe in the refrigerator.
2. The MC reached 150 mK during dilution.
3. The LN₂ trap continued to become blocked by contamination in the circulation loop.
4. Dilution was never run in a steady state manner.
5. The holding field did not superconduct.
6. Frozen spin mode was never attempted.
7. The polarizing magnet was never turned on.
8. The NMR system was never tuned due to a faulty coil.
9. The microwave power supply did not operate properly.
10. No thermal polarization was attempted.
11. No CH₂ cold recovery was attempted.

Discussion and Followup

The flowchart for the Super Cooldown run plan is shown in Figures 6.2, 6.3 and 6.4. Dilution progress was stymied at 150 mK due to an improper ratio of ³He/⁴He in the mash, an unidentified heat load to the MC, or both. The evaporator Roots pumps continued to fail, causing the 1 K pot to warm at various times during the run. The high separator flows

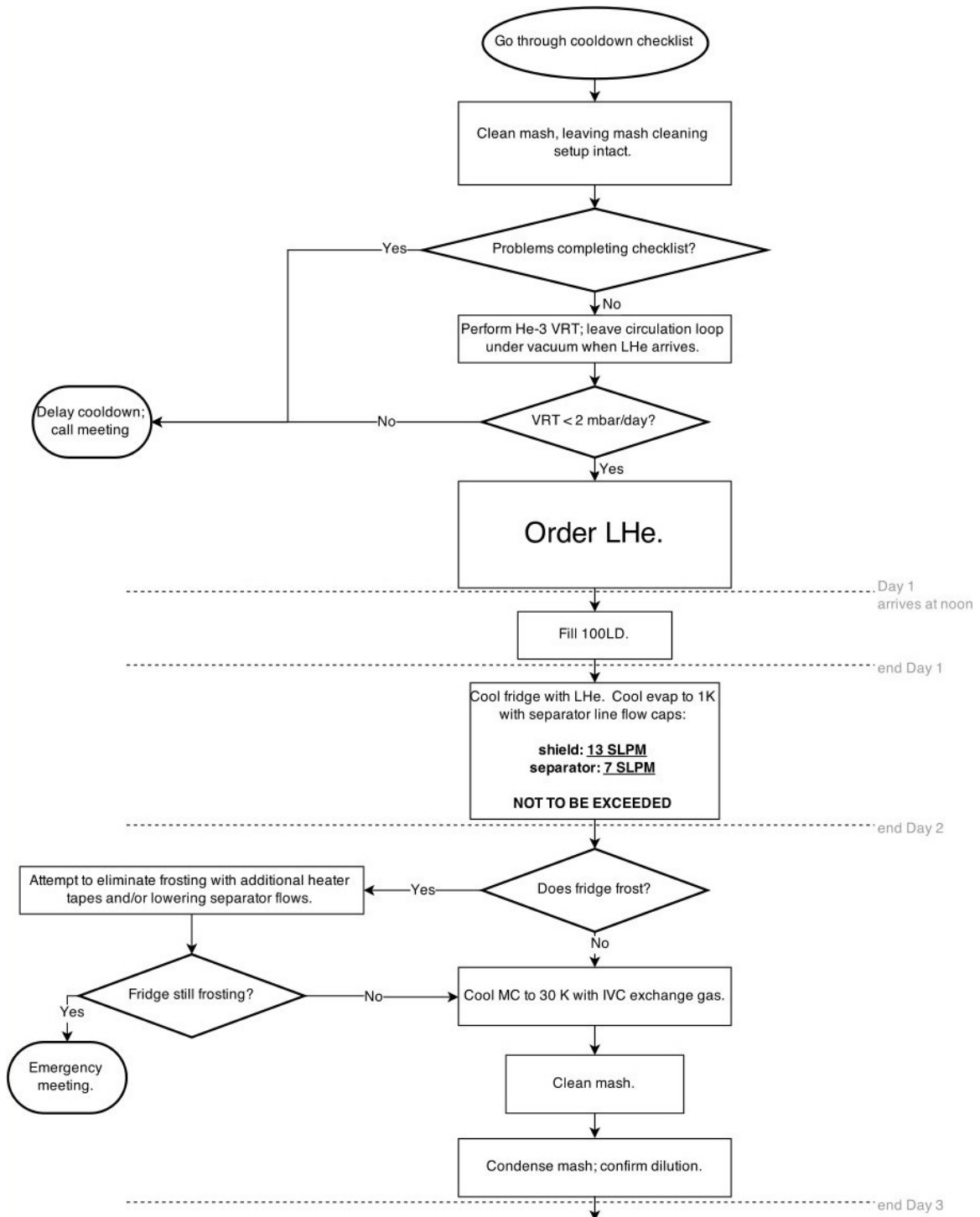


Figure 6.2: Flowchart of run plan for the Super Cooldown, Days 1-3.

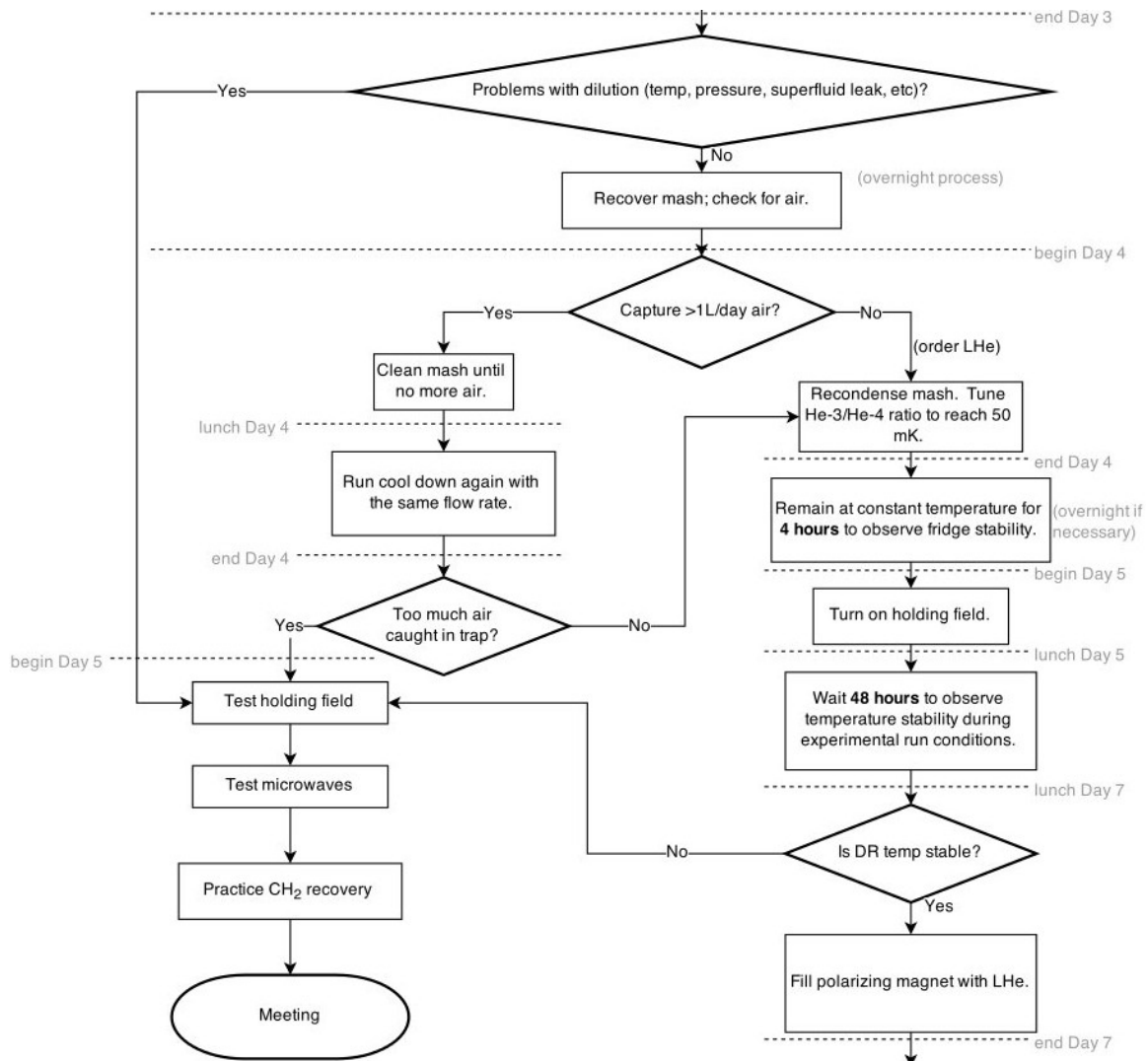


Figure 6.3: Flowchart of run plan for the Super Cooldown, Days 3-7.

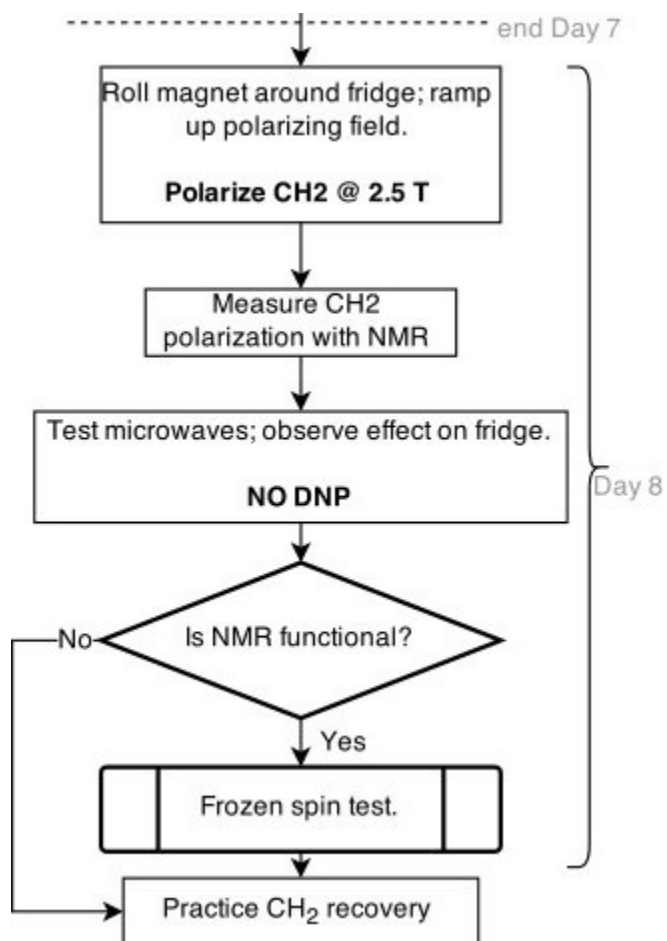


Figure 6.4: Flowchart of run plan for the Super Cooldown, Day 8.

caused considerable icing on the ^3He back flange causing the only source of the LN_2 trap contamination not yet ruled out. The lack of presence of a cold cathode gauge on the IVC prevented us from determining if there was a poor vacuum mediating heat between the MC and the evaporator (potentially caused by a botched exchange gas procedure).

Attempts to test the instrumentation² began on March 25, after a second round of dilution showed the same 150 mK floor on the MC temperature. The resistance of the holding coil was periodically checked with a manual DVM and it was found to never go superconducting. A similar check of the NMR coil resistance read $33\ \Omega$, explaining why it was impossible to tune. The microwave power supply would not provide microwaves at the required power and frequency to send into the refrigerator.

6.3 UVa Cooldowns

The refrigerator was moved to UVa after the Super Cooldown because it became impractical for UVa-based group members to continuously travel to Duke. It was intended for the ^4He sections of the refrigerator to be brought into normal operational mode, namely by solving the problems causing high separator flows and the failure of the coil to superconduct, by August 2015 before being sent back to Duke for the problems in the ^3He system to be investigated in a similar manner. Over the course of the summer, a TUNL advisory committee increased the scope of the work to achieving MC temperatures suitable for a frozen spin run.

6.3.1 June 2015 - Low Flow Cooldown

The first UVa cooldown aimed to only resolve the ^4He cryogenics issues; see Sections 4.2.2 and 4.2.3 for details.

²In this context, *instrumentation* refers to the NMR, holding coil and microwave subsystems.

Goals:

1. Operate the refrigerator at LHe temperatures with sustainable separator flows.

Results:

1. The refrigerator was successfully run at 25 SLPM total separator flows.

Discussion and Followup

The cooldown ran for 5 hours and consumed under 100 L LHe on June 10. The limited list of objectives and the focus of attention on a single goal contrasts greatly with those of the Super Cooldown two months earlier.

6.3.2 July 2015 - Magnet Cooldown #1

An excess of LHe from a PTGroup cooldown gave us a chance to try reproducing the previous cooldown's results after installing the magnet leads. While the ^4He cryogenics performed well, the leads exhibited the same behavior they did at Duke, i.e., not superconducting as expected from an environment with a superfluid film creep. One lead began to short to the refrigerator later in the cooldown, presumably due to vibrations in the pump line and inadequate electronic insulation.

6.3.3 August 2015 - Magnet Cooldown #2

The magnet leads were reinsulated and installed in the refrigerator and the resistance across the coil was read to DAQ. Again, the ^4He cryogenics were successfully operated at low flows, but the holding field resistance would not drop below $9\ \Omega^3$ despite the evaporator

³That is, a length of the coil corresponding to $9\ \Omega$ did not drop below the NbTi critical temperature of about 10 K.

continuously operating at 1.0-1.1 K. The cooldown consumed 100 L LHe and ran for about 10 hours.

6.3.4 December 2015 - Magnet Cooldown #3

The holding coil used in all previous cooldowns, which was wound at Duke in 2014, was found to be incompatible with the refrigerator, see Section 4.7.1 for details. A cooldown focusing on getting another coil, wound at UVa in November 2015, superconducting ran on December 5. Details about the coil's performance are given in 4.7.6.

Goals:

1. Get the new holding coil superconducting.

Results:

1. The coil went superconducting.

The cooldown consumed 100 L LHe and it took approximately 5.5 hours for the coil to go superconducting. The power supply for the holding coil magnet was not prepared ahead of time, and a last minute effort to get it online was not successful before we ran out of LHe from the supply dewar.

Chapter 7

Conclusions

7.1 Conclusion

In summary, great progress has been made on the development of a frozen spin polarized target for production use at HIGS. When the refrigerator arrived in 2011, the only technical progress that had been made was the conceptualization of the DFELL LHe transfer system and Roots stacks, as well as some electronic and mechanical work to accommodate the Hifrost equipment.

7.1.1 Final Results Review

In mid-2011, the refrigerator and various support systems were received from Geesthacht, Germany in a shipping container. After identifying all system components received, the target itself was opened and assessed, both as a dilution refrigerator and a frozen spin polarized target.

All vacuum cans were identified and verified to be in working condition, pumping down to the necessary 1E-6 mbar range. Minor leaks as high as 1E-7 mbar·L/s in the ^4He system were patched where possible, and the ^3He system was verified to be free of

leaks down to the $1\text{E-}9$ mbar·L/s range. The electronics in the refrigerator came with very limited documentation, so all connectors were retraced to their corresponding instruments and eventually rewired where possible. All temperature sensors were replaced with more modern, higher performing counterparts, allowing the mixing chamber temperature to be measured down to 17 mK.

The other supporting electronics modules that needed to be replaced includes: the 4-wire AC resistance bridge, the liquid helium level probe, the holding magnet power supply/load/controller, pressure gauge readouts, and water flow and thermocouple sensors for the EIO and NMR systems. Each of these systems were either purchased or designed by Hifrost collaborators before being integrated into the system. The new modules were integral to a novel data acquisition system developed for Hifrost between 2013-2015, which allows all sensors to be automatically queried and written to a database.

A new NMR system was designed from scratch with the assistance of the Jefferson Lab Polarized Target Group members. The system's hardware was reverse engineered from the existing Liverpool boxes and the software was a modified form of the UVa Polarized Target Group's PDP package. The entire NMR setup was tested in summer 2013.

At UVa, the refrigerator was first cooled with ^4He in 2012 and then with a suboptimal $^3\text{He}/^4\text{He}$ mixture in 2013, with the latter yielding temperatures as low as 270 mK. The entire system was then packed and moved to Duke.

In 2012 and 2013, the engineering staff at Duke University used geometric measurements from the target to develop a refrigerator swing for use in the experimental hall. The swing is a novel solution to the problem of rapidly assembling the polarized target containing volatile cryogenic material and cooling it to liquid helium temperatures. It was eventually tested with the refrigerator and aligned to allow reproducible placement relative to the beamline, Blowfish detector array and the central bore of the polarizing magnet.

Once at Duke, the ^3He circulation loop was rebuilt to meet leak rate specifications,

including an overhaul and recommissioning of the main Roots pump. Eventually, the system was cleared for dilution attempts when vacuum rise diagnostics were brought within operational specification of $\mathcal{O}(\text{L/day})$, which allowed operation non-stop for at least 48 hours.

In 2013 and 2014, the Hifrost team outfitted the Duke FEL Laboratory with the equipment, staff training and safety procedures to properly transfer LHe to the target area. Test results showed two critical pieces of equipment, a 500 L storage dewar and the wall transfer line (WTL), were not suitable for efficient LHe transfer. The WTL boils off LHe at a rate of about 200 L/day, and the 500 L dewar essentially loses all contained liquid overnight. A balance was struck between acceptable liquid helium loss and the need to continue commissioning the dilution refrigerator by modifying the liquid transfer procedures around the underperforming equipment.

The EIO and power supply were successfully tested in a simplified configuration in 2012 at DFELL, producing the required 5 mW microwaves used in DNP. However, subsequent tests through 2015 were unable to reproduce the results in the experimental configuration, possibly as a result of a damaged microwave frequency counter, mixer and power meter.

In 2014, the ^3He system was outfitted with a recovery system that both reduces gas loss by nearly 100% and allows the refrigerator condenser to be pressurized during the initial stage of dilution cooling. The recovery manifold also became instrumental during gas cleaning procedures, which were frequently needed as leaks were uncovered in the ^3He circulation loop.

Dilution was attempted in a series of cooldowns at Duke, with the mixing chamber reaching final temperatures of 200 mK in 2014 and 150 mK in 2015. In each case, the $^3\text{He}/^4\text{He}$ mixture ratio tuning was interrupted by leaks in the circulation loop, forming ice plugs in the condenser line and preventing further progress. Additional setbacks included the discover of various heat leaks to the ^4He system, with the worst being on the order of

watts, and the holding coil failing to superconduct. The refrigerator was moved back to UVa to work on these problems so the DFELL could be used for other experiments.

Finally, a series of experiments in 2015 at UVa resulted in the successful elimination of the ^4He heat leaks and the holding magnet being powered on, which required a new coil to be wound.

Most importantly, all technical progress made between 2011-2015 has been documented and shared with the collaboration in a centralized manner¹. The procedural methods that have been developed and described in the content of this dissertation have corresponding in-depth technical reports, available to all group members at Duke and UVa, so future researchers can pick the project up without reinventing the wheel.

7.1.2 Work To Be Done

The frozen spin target must be operated sustainably around 50 mK or below for a period of days in order to be useful for physics experiments. While progress on this has been made at UVa, the tunable parameters (gas mixture, pressures, instrumentation response) of the system are, in practice, different at DFELL. Therefore, the refrigerator must be operated at target temperatures at DFELL before a data run can be attempted.

Similarly, the NMR and holding magnet must be shown to continuously work in a production cryogenic environment at DFELL, where small differences like the environmental EM background noise may vary enough to affect operation.

The microwave generator and power supply have been tested in a mock setup at DFELL, but has never successfully been reproduced in the production configuration. While the primary difference between setups, namely the longer high voltage cables spanning from

¹UVaCollab, the University of Virginia's centrally-supported online collaboration and learning environment, has a repository of all referenced technical documents, including the Hifrost Manual, as well as data sheets and specifications for hardware purchased and commissioned during the years spanned by the work in this dissertation.

the target region to the power supply outside the GV, should have no effect on how well the microwave systems works, it has nevertheless eluded successful operation for the past several years.

Finally, a cold target load procedure, a fast-paced refrigerator assembly in which live target material initially cooled to 77 K is inserted in the refrigerator and must not be allowed to warm above a critical temperature, must be executed at the beginning of a data run. A successful cold target load is the timed orchestration of all developed cooldown preparation in addition to other obstacles, such as the transfer of target beads from the storage nitrogen dewar to the MC and indium installations in a LN_2 environment with the absence of the usual verification of leak tightness with the leak detector.

Bibliography

- [A⁺00] J. Ahrens et al., *Helicity dependence of $\gamma p \rightarrow N\pi$ below 450 mev and contribution to the gerasimov-drell-hearn sum rule*, Phys. Rev. Lett. **84** (2000), 5950–5954.
- [Ber02] Lou Bertolini, *The us particle accelerator school vacuum testing and leak detection*, http://uspas.fnal.gov/materials/02Yale/11_LeakDetection.pdf, 6 2002, Beginning at slide 25.
- [Bor71] M. Borghini, *Mechanisms of nuclear dynamic polarization by electron-nucleus dipolar coupling in solids*, Conf. Proc. **C710830** (1971), 1–32.
- [Bra08] A. Braghieri, *Nstar 2007: Proceedings of the 11th workshop on the physics of excited nucleons, 5–8 september 2007, bonn, germany*, ch. GDH sum rule and double polarization experiments on the deuteron, pp. 173–175, Springer Berlin Heidelberg, Berlin, Heidelberg, 2008.
- [CG80] G Court and DW Gifford, *Liverpool nmr module, q-meter fundamentals, and circuit testing*, Ultra Physics LTD, November 1980.
- [Che55] G.V. Chester, *Statistical mechanics of mixing of isotopes*, Phys Rev **100** (1955), no. 2, 446–454.

- [CM97] D. G. Crabb and W. Meyer, *Solid polarized targets for nuclear and particle physics experiments*, Annual Reviews Nuclear and Particle Physics **47** (1997), no. 1, 67–109.

- [Cry16] Lake Shore Cryotronics, *Dt-670 silicon diode specifications*, <http://www.lakeshore.com/products/cryogenic-temperature-sensors/silicon-diodes/dt-670/pages/Specifications.aspx>, 2016.

- [Den27] David M Dennison, *A note on the specific heat of the hydrogen molecule*, Proceedings of the Royal Society of London. Series A, Containing Papers of a Mathematical and Physical Character **115** (1927), no. 771, 483–486.

- [DHK⁺04] H. Dutz, K. Helbing, J. Krimmer, T. Speckner, G. Zeitler, et al., *Experimental check of the gerasimov-drell-hearn sum rule for ^1H* , Phys. Rev. Lett. **93** (2004), 032003.

- [DS15] Ryan Duve and Kelly Strauch, *Solid polarized target lab overview*, graduate/undergraduate partnership project, August 2015.

- [Dut04] H. Dutz, *Highlights of polarized solid state target instrumentation*, Nuclear Instruments and Methods in Physics Research Section A: Accelerators, Spectrometers, Detectors and Associated Equipment **526** (2004), no. 12, 117 – 125, Proceedings of the ninth International Workshop on Polarized Solid Targets and Techniques.

- [Duv] Ryan Duve, *August 2012 cooldown aftermath*, http://twist.phys.virginia.edu/~duve/hifrost/20120827_cooldown-aftermath.html.

- [Duv13] ———, *Hifrost annual project report*, Submitted to Blaine Norum, 2 2013.
- [Duv14] ———, *Post cooldown hifrost work*, <http://hifrost.org/status/20140723/>, 7 2014.
- [Duv15a] ———, *Hifrost manual*, 10 2015, Technical Hifrost documentation including procedural and hardware minutia.
- [Duv15b] ———, *Holding coil for a frozen spin target*, Tech. report, 11 2015.
- [Duv15c] ———, *Yale card housing installation*, Tech. report, The University of Virginia, 8 2015.
- [dV01] R. Van de Vyver, *First results from the {GDH} experiment on the proton at {MAMI}*, Nuclear Physics A **689** (2001), no. 12, 379 – 382, European Few-Body Problems in Physics.
- [EC] Emerson and Cuming, *Stycast 1265 a/b msds*, <http://physics111.lib.berkeley.edu/Physics111/Reprints/SHE/1265.pdf>.
- [Eki06] Jack W. Ekin, *Experimental techniques for low-temperature measurements*, Oxford University Press, 2006, pages 57-59.
- [Equ] ACE Equipment, *Proper wire tension*, <http://www.armaturecoil.com/wire-size-tension-chart/>.
- [For68] Paul Forman, *The doublet riddle and atomic physics circa 1924*, Isis **59** (1968), no. 2, 156–174.
- [Fow36] R.H. Fowler, *Statistical mechanics: The theory of the properties of matter in equilibrium*, pp. 85–86, Macmillan, 1936.

- [GHPM15] R.G Goodrich, Donavan Hall, Eric Palm, and Tim Murphy, *Dry dilution refrigerator with he-4 1k loop*, Cryogenics **38** (2015), 221–225.
- [Gil13] Christina Gilligan, *Dual trap manifold*, Tech. report, The University of Virginia, 8 2013, Polarized Target Group.
- [GMGT54] M. Gell-Mann, M. L. Goldberger, and W. E. Thirring, *Use of causality conditions in quantum theory*, Phys. Rev. **95** (1954), 1612–1627.
- [Gol58] L.J.B. Goldfarb, *The polarization of deuterons and particles of arbitrary spin*, Nuclear Physics **7** (1958), 622 – 642.
- [Gu03] Lixing Gu (ed.), *Generalized equation for thermal conductivity of mli at temperatures from 20k to 300k*, vol. 2, ASME International Mechanical Engineering Congress, ASME, 11 2003, 467-473.
- [Hel04] Klaus Helbing, *Experimental Verification of the GDH Sum Rule*, Gerasimov-Drell-Hearn sum rule and its extensions. Proceedings, 3rd International Symposium, GDH 2004, Norfolk, USA, June 2-5, 2004, 2004, pp. 28–39.
- [Hel06] Klaus Helbing, *The Gerasimov-Drell-Hearn Sum Rule*, Prog. Part. Nucl. Phys. **57** (2006), 405–469.
- [HMP16] Franziska Hagelstein, Rory Miskimen, and Vladimir Pascalutsa, *Nucleon polarizabilities: From compton scattering to hydrogen atom*, Progress in Particle and Nuclear Physics **88** (2016), 29 – 97.
- [Jah04] O. Jahn, *Status of the GDH experiment on the deuteron at MAMI*, Gerasimov-Drell-Hearn sum rule and its extensions. Proceedings, 3rd International Symposium, GDH 2004, Norfolk, USA, June 2-5, 2004, 2004, pp. 41–50.

- [JGO74] P.W Keaton Jr., John L Gammel, and Gerald G Ohlsen, *Formalism for the $T(d, n)4\text{He}$ and $3\text{He}(d, p)4\text{He}$ reactions*, Annals of Physics **85** (1974), no. 1, 152 – 213.
- [JLA12] JLAB, *Thomas Jefferson National Lab Hall A Wiki - Solid Polarized Target*, https://hallaweb.jlab.org/wiki/index.php/Solid_Polarized_Target, 11 2012.
- [Joh14] Andrew Johnson, *Introduction to epics*, <http://www.aps.anl.gov/epics/docs/APS2014/01-Introduction-to-EPICS.pdf>, 9 2014, AES-SSG.
- [Kei94] Christopher Keith, *Total cross section measurements for the scattering of polarized neutrons from polarized He-3*, Ph.D. thesis, North Carolina State University, 1994.
- [Kei12] C.D. Keith, *The Jefferson Lab Frozen Spin Target*, Nuclear Instruments and Methods in Physics Research A **684** (2012), 27–35.
- [Kei13] Chris Keith, *Hifrost cooling notes*, email correspondence, 2 2013, Section: "Cleaning the LN2 trap while circulation".
- [Kel13] Dustin Keller, *Investigation into polarization uncertainty minimization of solid polarized targets*, Proceedings of Science **10** (2013).
- [Ken14] David Kendellen, *Hifrost cooldown notes*, Group email, 10 2014.
- [Kie91] William Kielhorn, *A technique for measurement of vector and tensor polarization in solid spin one polarized targets*, Master's thesis, University of Texas at Austin, 5 1991.

- [KJL] Company Kurt J. Lesker, *Residual gas analyzers - how rgas work*, https://www.lesker.com/newweb/technical_info/vacuumtech/rga_01_howrgaworks.cfm?section=leaks.
- [Lan24] A. Landé, *Die absoluten intervale der optischen dubletts und tripletts*, Zeitschrift fur Physik **25** (1924), 56.
- [LN99] A. I. L'vov and A. M. Nathan, *Sum rule for the backward spin polarizability of the nucleon from a backward dispersion relation*, Phys. Rev. **C59** (1999), 1064–1069.
- [LSC] Inc. Lake Shore Cryotronics, *Lakeshore cryotronics product manual*, online distribution, page 146.
- [Mas05] M. Massimi, *Pauli's exclusion principle: The origin and validation of a scientific principle*, Cambridge University Press, 2005, Chapter 2.
- [McK00] Paul McKee, *The spin structure of the proton from slac experiment e155*, Ph.D. thesis, University of Virginia, 8 2000.
- [Mis09] R. Miskimen, *Measuring the spin-polarizabilities of the proton in double-polarized real compton scattering*, HIGS proposal PAC-09, 5 2009.
- [MR01] J. Mehra and H. Rechenberg, *The historical development of quantum theory*, no. v. 1-2, Springer, 2001.
- [MRB69] S. Mango, . Runlfsson, and M. Borghini, *A butanol polarized proton target*, Nuclear Instruments and Methods **72** (1969), no. 1, 45 – 50.
- [Nii71a] Tapio Niinikoski, *A horizontal dilution refrigerator with very high cooling power*, Nuclear Instruments and Methods **97** (1971), 95–101.

- [Nii71b] T.O. Niinikoski, *Construction of sintered copper heat exchangers*, Cryogenics **11** (1971), no. 3, 232 – 233.
- [Nii76] Tapio Niinikoski, *"frozen spin" polarized target*, Nuclear Instruments and Methods **134** (1976), 219–233.
- [Nii15a] ———, private correspondence, November 2015.
- [Nii15b] ———, *private correspondence*, email, November 2015.
- [Nor09] Blaine Norum, *Measurements of the drell-hearn-gerasimov integrand for the deuteron*, 5 2009, HIGS proposal.
- [Nor16] ———, *Measurement of the tensor analyzing power in deuteron photo- disintegration between $e = 4$ mev and 20 mev*, 2 2016, HIGS proposal, pp. 10-13.
- [NRS12] S.B. Nurushev, M.F. Runtso, and M.N. Strikhanov, *Introduction to polarization physics*, Lecture Notes in Physics, pp. 318–321, Springer Berlin Heidelberg, 2012.
- [OE16] INC Omega Engineering, *Polyimide film insulated flexible heaters*, http://www.omega.com/heaters/pdf/KHR_KHLV_KH.pdf, 2016.
- [PDV07] B. Pasquini, D. Drechsel, and M. Vanderhaeghen, *Proton spin polarizabilities from polarized Compton scattering*, Phys. Rev. **C76** (2007), 015203.
- [Pob07] F. Pobell, *Matter and methods at low temperatures*, Springer-Verlag, 2007.
- [Pri14] Glen Pridham, *Photodisintegration of the deuteron at 18 mev using linearly polarized photons*, Ph.D. thesis, University of Saskatchewan, 7 2014, M.Sc dissertation.

- [PV16] GmbH Pfeiffer Vacuum, *Indirect, gas-dependent pressure measurement*, <https://www.pfeiffer-vacuum.com/en/know-how/vacuum-measuring-equipment/fundamentals-of-total-pressure-measurement/indirect-gas-dependent-pressure-measurement/>, 2016.
- [Pyw15] Rob Pywell, *University of saskatchewan experimental subatomic physics software simulations*, <http://kanga.usask.ca/Software.html>, 5 2015.
- [Rou66] P. Roubeau, *Horizontal cryostat for polarized proton targets*, *Cryogenics* **6** (1966), no. 4, 207–212.
- [Rus71] F. M. Russell, *Present and future prospects for separated function frozen targets.*, Conf. Proc. **C710830** (1971), 89–98.
- [RV71] P. Roubeau and J. Vermeulen, *Continuous flow horizontal he3 cryostat for organic polarized proton targets*, *Cryogenics* **11** (1971), no. 6, 478 – 482.
- [Seo12a] Pil Seo, *Second dilution refrigerator test for hifrost at uva*, Group email, 12 2012.
- [Seo12b] ———, *Status of hifrost*, email, 2 2012.
- [Seo13] ———, *Run plan for hifrost instrumentation test*, Distributed to TUNL administration and Hifrost work group, 12 2013.
- [SNP09] Deepshikha Shukla, Andreas Nogga, and Daniel R. Phillips, *Analyzing the effects of neutron polarizabilities in elastic compton scattering off ^3He* , *Nuclear Physics A* **819** (2009), no. 14, 98 – 134.

- [TD14] Brogan Thomas and Ryan Duve, *Making indium wiring for cryo*, Tech. report, UVa and Duke University, 2 2014.
- [Tec12] Agilent Technologies, *Pcg-750 pirani capacitance diaphragm gauge*, 2 ed., March 2012, Manual No. TQNa77e1.
- [TN01] M. Taketani and M. Nagasaki, *The formation and logic of quantum mechanics*, The Formation and Logic of Quantum Mechanics, World Scientific, 2001, pg. 221.
- [TSHN98] J. Tonnison, A. M. Sandorfi, S. Hoblit, and A. M. Nathan, *First extraction of a spin polarizability of the proton*, Phys. Rev. Lett. **80** (1998), 4382–4385.
- [Uh15] Kurt Uhlig, *Dry dilution refrigerator with he-4 1k loop*, Cryogenics **66** (2015), 6–12.
- [Wei98] J.G. Weisend, *The handbook of cryogenic engineering*, CRC Press, 7 1998, page 186.
- [WF56] G.K. Walters and W.M. Fairbank, *Phase separation in ^3He - ^4He solutions*, Phys Rev **103** (1956), no. 1, 262–263.
- [Whe68] J. C. Wheatley, *Dilute Solutions of ^3He in ^4He at Low Temperatures*, American Journal of Physics **36** (1968), 181–210.
- [Wur10] Ward Wurtz, *Photodisintegration of lithium isotopes*, Ph.D. thesis, University of Saskatchewan, 8 2010, Ph.D. dissertation.
- [Zho13] Y. Zhou, *Physics 1942 – 1962: Including presentation speeches and laureates' biographies*, ch. Willis Lamb, Fine structure of the hydrogen atom, pp. 286–295, Elsevier Science, 2013.